

Angus
Petty

2023

***A Micromechanical Investigation of
Soil-Structure Interface Behaviour***



University of
Nottingham
UK | CHINA | MALAYSIA

Abstract

A limiting factor in the drive to deliver performance-based design is the lack of knowledge regarding the constitutive behaviour of soil-structure interfaces, particularly in the case of cyclic loading. Attempts to model the behaviour of these interfaces have failed to consider the long-term effects of cyclic loading, in particular how both the soil and structure may degrade over the course of thousands of cycles. To address this shortfall in understanding, consideration must be given to not only the geotechnical aspects of the interface, but also the structural aspects, and how these two components interact over the course of a structure's lifetime. This thesis presents a micromechanical investigation of the behaviour of soil-structure interfaces, with a particular focus on these cyclic effects by carrying out novel experimental testing at the macro-scale and single-particle scale.

At the macro-scale, a series of direct shear tests were carried out on a smooth stainless steel interface under a constant normal load. After continued shearing, the interface experiences a rapid elevation in the shear force transferred, accompanied by an increase in roughness of the surface and crushing of the Leighton Buzzard Sand grains. These observations are found to corroborate similar behaviour witnessed in literature. However, the initial trigger of this rapid increase in shear force cannot be explained by existing models, or verified by macro-scale observations. Therefore it was necessary to investigate the behaviour of the interface at the single-particle scale. A novel testing apparatus was developed to carry out single-particle direct shear tests on a smooth stainless steel interface. Testing revealed that the steep elevation in shear force also occurs at the single-particle scale and is caused by abrasive wear at the interface.

To investigate the abrasive wear at the single-particle scale further, a method was developed to accurately model the contact geometry of the particle. A particle virtualisation methodology was implemented to capture high resolution 3D meshes of the 1.5 mm particles, with a provision to directly compare the grain meshes prior to and after testing. Using this methodology, it was found that the particle

undergoes a significant change in shape during testing, with the particle becoming flattened and the nominal contact area increasing. This insight, of abrasive wear to the equivalently harder abrasive particle, has not been readily considered by tribological studies due to the difficulty of modelling and monitoring the contact geometry of irregular particles.

The frictional response of irregular particles during abrasive shearing therefore required further investigation, to establish a method for characterising local 3D angularity. Using the particle virtualisation methodology, a novel method was developed to characterise the local 3D angularity of the particle, and the evolution of this angularity during shearing. A new parameter, 3D attack angle, has been established, which characterises the angle an irregular abrasive grain makes with a planar surface. This new parameter is found to have a strong correlation with the rapid increase in shear force transmitted at the interface, whereby at the point of sudden shear load increase, there is a corresponding sudden change in 3D attack angle. It is therefore concluded that the rise in shear force is caused by an initial decrease in the 3D attack angle of the particle, which causes cutting abrasive wear to the surface.

With a better understanding of the micromechanical processes occurring at the interface, the macroscopic mechanisms that govern global response can be viewed in a new light. As such, more informed engineering decisions can be made regarding the design of soil-structure interfaces, which will ultimately lead to more efficient and sustainable infrastructure.

Declaration

All of the work in this thesis is my own, unless otherwise stated. The work of others has been referenced appropriately.

Dedication

To Mum and Dad, without your endless support this would simply never have been possible. The countless hours spent helping me revise, and encouraging me to keep going when knocked down have been invaluable.

Acknowledgements

I would like to thank my supervisor, Dr. Charlie Heron, in addition to the entire Department of Civil Engineering for their support throughout my time at the University of Nottingham. To work on this project has been a privilege, and I am incredibly grateful for all of the guidance, advice and opportunities I have received.

Thank you also to the technical staff, Andrew Maddison, Lee Hickling, Mark Dale, Steve Lawton and Harry Hardy, for their skilled assistance with fabrication and testing.

This work was supported by the UK Engineering and Physical Sciences Research Council (EPSRC) grant EP/R51328311 for the University of Nottingham Centre for Doctoral Training.

Contents

1	Introduction	1
I	Establishing a Motivation and Strategy	4
2	Literature Review	5
2.1	Granular Mechanics	5
2.1.1	Characterising Shape	7
2.1.2	Particle Breakage	11
2.1.3	Crushing of Granular Bodies	18
2.1.4	Granular Force Chains	21
2.2	Tribology and Metallurgy	24
2.2.1	Abrasive Wear	25
2.3	Soil-Structure Interfaces	31
2.3.1	Relevant Terminology	31
2.3.2	Stress Paths and The Influence of Boundary Condition .	32
2.3.3	Initial State and Relative Density	35
2.3.4	Roughness and Hardness	39
2.4	Summary of Findings and Conclusions	42
3	Aims and Objectives	44
II	Investigation and Analysis	46
4	Abrasion in cyclically sheared interfaces	48
4.1	Notes	48
4.2	Introduction	48

CONTENTS

4.3	Experimental Framework	51
4.3.1	Testing Apparatus	51
4.3.2	Test Data	53
4.3.3	Test Plan	54
4.4	Apparatus Benchmarking	57
4.5	Testing Objectives	58
4.6	Results	60
4.6.1	Overview of Results	60
4.6.2	Macroscopic Testing	63
4.6.3	Single-particle Testing	68
4.7	Discussion	70
4.7.1	Stress Ratio Elevation	70
4.7.2	Influence of abrasion	73
4.7.3	Stress Ratio Degradation	76
4.8	Conclusions	79
5	Quantifying Interface Abrasion	82
5.1	Notes	82
5.2	Introduction	82
5.3	Methodology	84
5.3.1	Overview	84
5.3.2	Focus Stacking	85
5.3.3	Binarisation and volume realignment	86
5.3.4	Angular realignment of pre and post-test volumes	87
5.3.5	Vertical realignment of pre and post-test volumes	88
5.3.6	Vertical Displacement Tracking	89
5.3.7	Resolution of Virtualized Grains	90
5.3.8	Grain Comparison	90
5.4	Results and Discussion	92
5.4.1	Quantifying Abrasive Wear of Interface Bodies	92
5.4.2	Effect of Shearing Energy on Abrasion	96
5.4.3	Effect of particle surface area on abrasion	97
5.5	Conclusions	102
5.6	Code Availability	103

6	Frictional Response of Irregular Grains	104
6.1	Notes	104
6.2	Introduction	104
6.3	Methodology	106
6.3.1	Single-particle shear	106
6.3.2	Particle Virtualisation and Mesh Processing	108
6.4	Shape Tensor Analysis	109
6.5	Attack Angle Analysis	110
6.5.1	Characterising Abrasive Wear to Irregular Grains	110
6.5.2	3D Attack Angle	113
6.5.3	Frictional Response of 3D Attack Angle	116
6.6	Conclusions	121
III	Conclusions and Recommendations	123
7	Conclusions and Recommendations	124
7.1	Review of Findings	124
7.1.1	Chapter 4: The role of abrasion in cyclically sheared soil-structure interfaces	124
7.1.2	Chapter 5: Quantifying Interface Abrasion with Particle Virtualization	125
7.1.3	Chapter 6: Characterising Frictional Response of Irregular Abrasive Grains with 3D Attack Angle	126
7.2	Application of Findings	127
7.3	Future Work	128
A	Effect of Crushed Particles on Soil-Structure Interface Behaviour	129
A.1	Introduction	130
A.2	Methodology	131
A.2.1	Experimental Apparatus	131
A.2.2	Test Plan	132
A.3	Testing Medium	133
A.3.1	Soil	133
A.3.2	Structural Interface Plate	133

CONTENTS

A.3.3	Data Collection and Processing	134
A.3.4	Image Data	134
A.3.5	Data Smoothing	135
A.4	Results and Discussion	136
A.4.1	Stress Response	136
A.4.2	Volumetric Response	137
A.4.3	Damage to the Interface	139
A.5	Micromechanical Response	140
A.6	Conclusions	141
B	3D Attack Angle Full Results	143
B.1	3D Attack Angle	143
B.2	Particle Vertical Displacement	145
B.3	Particle Contact Area	145

List of Figures

2.1	Three scales of particle shape in 2D, derived from Barrett Barrett (1980)	8
2.2	Particle shape determination (reproduced from Cho et al. (2006))	8
2.3	Form parameters for extreme 3D bricks, derived from Orosz et al. (2021)	10
2.4	Plots reproduced from Sandeep and Senetakis (2018)	12
2.5	Representation of principal axes in platen crushing	15
2.6	Force-displacement curve of artificial grain in compression, reproduced from Antonyuk et al. (2005)	16
2.7	Diagram summarising the successive movement of parallel critical state lines in relation to the fractal crushing of granular material	22
2.8	Diagrammatic and mathematical definition of force chains . . .	22
2.9	Illustration of the differences between (a) two-body abrasion, (b) three body abrasion, reproduced from Hutchings and Shipway (2017)	25
2.10	Illustration of contact between a grit particle under normal load and a plane surface, reproduced from Hutchings and Shipway (2017)	27
2.11	Geometry of contact between conical abrasive and surface in elevation view, reproduced from Hutchings and Shipway (2017)	28
2.12	Diagram of a direct interface shear box showing the thickness t of the interface layer	32
2.13	Diagram of the three boundary conditions present in interface testing	33
2.14	Diagram of the relative roughness at a soil-structure interface . .	33
2.15	2D simple shear tests results for CNL and CNS tests (reproduced from Evgin and Fakharian (1996))	35

LIST OF FIGURES

2.16	Example of PIV imaging and patching from DeJong and Westgate (2009)	36
2.17	Simple interface shear results, from Oumarou and Evgin (2005)	38
4.1	Schematic of the single particle direct shear interface	52
4.2	Schematic of the macro direct shear apparatus	53
4.3	Comparison of shear stress degradation response in constant normal stiffness shearing of macroscopic direct shear tests against response reproduced from Mortara et al. (2007)	59
4.4	Macroscopic direct shear stress ratio vs cycle number for tests where $\sigma_n = 100$ kPa with associated cycle image data	61
4.5	Single-particle shear stress ratio vs cumulative energy for Stainless Steel tests with Fraction A and glass bead particles for assorted normal weights	62
4.6	Plot of vertical displacement and stress ratio against number of shears for macroscopic direct shear tests where $\sigma_n = 100$ kPa . .	64
4.7	Images captured of soil body pre- and post- cyclic shearing during macroscopic direct interface shear test	65
4.8	Excerpt of interferometry sampling of Fraction A — Stainless Steel macroscopic interface pre-test and post-test	67
4.9	Single-particle interface shear interferometer surface plot	69
4.10	Comparison of average stress ratio and volumetric response in macroscopic direct shear test where $\sigma_n = 100$ kPa and 50 kPa . .	71
4.11	Plots of shear load against shear displacement showing pre-elevation, post-elevation elevated, and post-elevation degraded shear behaviour in a macroscopic direct shear test where $\sigma_n = 100$ kPa	72
4.12	Plots of shear load against shear displacement showing pre-elevation and post-elevation shear mechanism in a single particle interface shear test	74
4.13	Schematic showing method for calculating cutting plasticity ratio	75
4.14	Single-particle interface shear stress response with comparison to the cutting-plasticity ratio η for mild steel interfaces with 500 g of applied load	77
5.1	Overview of particle virtualization	86

LIST OF FIGURES

5.2	Particle Virtualization Framework: (a) Image of particle virtualization apparatus, (b) Focus stacking of images at different focal length, (c) Rescaling of post-test images based on image similarity, (d) Schematic of image-based particle depth detection	91
5.3	Comparison of pre and post-test grains meshes with maximum Z coordinate representing tip stated	91
5.4	Stacked bar plot comparing the proportions of abrasive wear in terms of volume lost from the tip of grains, and volume abraded from interface surface	93
5.5	Stacked bar plot comparing the proportions of abrasive wear in terms of height lost from the tip of grains, and mean trough coordinate of interface surface	93
5.6	Plot of absolute volume change plotted against cumulative energy of shearing, point size represents change in height of grain	98
5.7	Comparison of cumulative shearing energy against vertical displacement	99
5.8	Normal embedment tests of sand grains	100
5.9	Change of nominal particle contact area pre- and post-test with increase in active area in contact during shear (3D meshes are shown viewing the tip of the grain): (a) Nominal contact area for a grain under normal load prior to shearing, (b) Nominal contact area for abraded grain under normal load after shearing, (c) Active contact area for abraded grain during shearing, schematic shows the particle outline and selection of outline faces	101
6.1	Virtualised meshes of sample particle pre- and post-test in single-particle interface shear. Meshes have been processed with ‘collapse_short_edges’ using a threshold of $3\times$ the mean average edge length	109
6.2	Ternary plot of the form parameters for the volume of particle embedded in the surface, for all tests	110
6.3	Violin plot showing the similarity distribution of face normals to z-normal vector at the tip of post-test grains	112
6.4	Plots of vertical displacement, Δz , and stress ratio, μ , against cumulative shearing energy	114

LIST OF FIGURES

6.5	Plots of contact area, ΣA , and stress ratio, μ , against cumulative shearing energy	117
6.6	Development of 3D attack angle: (a) Example of 2D attack angle α estimation for an irregular geometry at increasing levels of embedment z , (b) Example of weighted face attack angle calculation on a sphere	118
6.7	Mean angle of face attack angles to xy plane for a sphere with radius 50 px	119
6.8	Plots of 3D attack angle, α_{3D} , and stress ratio, μ , against cumulative shearing energy	120
A.1	Diagram of the three principal interface orientation conditions	131
A.2	Schematic of updated Toton Shear apparatus	132
A.3	Sample image after post-processing	135
A.4	Plot of the stress ratio, μ , vs cumulative shear displacement	136
A.5	Plot of first derivative of stress ratio, $d(\mu)$, vs stress ratio, μ	137
A.6	Plot of vertical displacement against cumulative shear displacement	138
A.7	Grain size distribution analysis for each test and a clean, untested sample	139
A.8	Frame taken from test 100-10-180-1 at 40,000 mm displacement	139
A.9	Image of damaged interface plate after tests (a) 100-10-000-1, (b) 100-180-10-2	141
A.10	Comparison of crushing mechanisms for (a) upright and (b) inverted test	142
B.1	Plots of 3D attack angle, α_{3D} , and stress ratio, μ , against cumulative shearing energy for the entire dataset	144
B.2	Plots of particle vertical displacement, z , and stress ratio, μ , against cumulative shearing energy for the entire dataset	146
B.3	Plots of particle contact area, A , and stress ratio, μ , against cumulative shearing energy for the entire dataset	147

List of Tables

1.1	Summary of journal articles included in this thesis, and their status as of publication.	3
2.1	Classification of abrasive wear, adapted from Gates (1998) . . .	26
4.1	Test plan for macroscopic direct shear	55
4.2	Test plan for single-particle direct shear	57
5.1	Comparison of volume of abrasive wear of particle and interface after shearing	92
5.2	Comparison of change of height of particle and depth of interface after shearing, with vertical displacement at end of test	94
A.1	Test plan for upright and inverted direct shear tests	133

List of Symbols

The following list of symbols is subdivided by chapter to be referenced in the text. Where necessary, a symbol may be changed from that which is traditionally used in literature due to the disparate topics of this thesis.

α	Attack angle of an abrasive particle, between the particle centroid and particle face tangent
β	Attack angle of an abrasive particle, between the particle face tangent and surface tangent
Δe_b	Change in voids ratio due to particle breakage
ΔX	Horizontal displacement
η	Cutting-plasticity ratio, the ratio between plastic flow and cut material
Γ	Particle toughness
ι	Stress invariant
λ	Plastic compressibility index
μ	Coefficient of friction or stress ratio
μ_u	Interparticle coefficient of friction
ϕ_{cs}	Critical state friction angle
Ψ	Dimensionless wear coefficient
ψ	Specific wear rate
ρ	Regularity of a particle as defined by Cho et al. (2006)
σ	Stress

LIST OF SYMBOLS

σ_f	Nominal strength of a particle
σ_n	Normal stress
σ_t	Tensile crushing strength of a particle
τ	Shear stress
θ_c	Angle between particle centres in a force chain as defined by Xu and Liu (2019)
A	Area of a face
B_p	Breakage potential of a particle as defined by Hardin (1985)
B_t	Total breakage of a sample as defined by Hardin (1985)
D	Concluding fractal dimension of a soil sample as defined by McDowell et al. (1996)
d	Diameter of a particle
d_{50}	Mean particle diameter
E	Cumulative energy of shearing
e	Voids ratio
F	Force
f	Shape orientation tensor as defined by Orosz et al. (2021)
h	Particle hardness
H_a	Hardness of an abrasive particle
H_s	Hardness of a surface
I_D	Relative density
I_e	Interval between maximum and minimum voids ratio
K	Normal stiffness of the boundary condition
n	Normal vector of a face
N_F	Force applied in Brazilian test

LIST OF SYMBOLS

p'	Effective normal stress
$P_s(V)$	Survival probability of a particle as defined by McDowell and Bolton (1998)
Q	Total volume removed per unit shear distance
q	Deviatoric stress
R_{\max}	Maximum distance between the peak and trough along the a surface profile of length equal to d_{50}
R_H	Relative hardness of a particle and surface
R_n	Relative roughness of a soil-structure interface
t	Thickness of the interface layer
t_p	Thickness of a particle
U	Specific energy for material removal
u_x	Tangential displacement
V	Volume
v	Specific volume
Y	Uniaxial yield stress of a material
Z_{crit}	Critical coordination number as defined by Barreto and O'Sullivan (2012)
R	2D roundness as defined by Cho et al. (2006)
R^*	Relative roundness of a particle as defined by Cavarretta et al. (2016)
r_i	Radius of a local surface feature
$r_{\max\text{-in}}$	Maximum size of an inscribed circle within a particle
$r_{\min\text{-cir}}$	Minimum size of a circumscribed circle around a particle
S	2D sphericity as defined by Cho et al. (2006)
CNL	Constant Normal Load
CNS	Constant Normal Stiffness
ICP	Iterative Closes Point (for mesh realignment)

Chapter 1

Introduction

Soil-structure interfaces are a critical component of all geotechnical structures, and there is a growing reliance and ever-increasing demand for these interfaces to support critical infrastructure, such as wind turbine foundations and pipelines. At some point also, these structures will need to be decommissioned, and an accurate understanding of the interface behaviour is required to ensure the safe and economical removal of these structures. There is currently a desire to implement performance based design, to tackle one of the key challenges currently faced by the industry, to minimise the environmental impact of construction. In general, the design of soil-structure interfaces is based on empirical methods, which are not always accurate, and can lead to over-conservative designs.

A limiting factor in the delivery of performance-based design at present is the lack of knowledge regarding the constitutive behaviour of soil-structure interfaces, particularly in the case of cyclic loading, with the majority of research efforts focusing on the macroscopic interaction at the interface. Geotechnical research, particularly granular mechanics has seen rapid advances in understanding with a focus on micromechanical behaviour. To that end, this thesis aims to investigate the micromechanical behaviour of soil-structure interfaces, by focusing predominately on the interaction between the interface and a single grain. By building a greater understanding of the micromechanical interaction, the macroscopic behaviour of soil-structure interfaces can be better understood. To achieve this, advancements are required in the experimental modelling of soil-structure interfaces. One challenge that has stymied research is the lack of available purpose built experimental platforms. As such, a foundation of this thesis is the development of new experimental and analysis methods, which will continue to be of use in further research, and serve as inspiration for other studies.

Where possible, the experimental methods developed in this thesis have been validated against existing experimental research. Furthermore, analysis packages have been made available in open-source, to allow for the replication of results, and to allow for further development of the methods.

Thesis Structure

This thesis is submitted ‘by papers’, with the main body of the thesis made up of three first-author journal articles. To more easily discern what elements have been written specifically for this thesis, three parts have been established. The first part of the thesis, *Establishing a Motivation and Strategy*, contains a comprehensive literature review chapter, and chapter summarising the aims and objectives of this thesis, having considered the literature. The second part of the thesis, *Investigation and Analysis*, contains the three journal articles, the status of which are summarised in Table 1.1). To suit the narrative structure of the thesis, the articles have been modified from their submitted form. Firstly, the introduction to the journal entries has been removed and is incorporated into a comprehensive literature review, unless it is explicitly required to provide context. Secondly, where appropriate, further narrative has been added to the articles to provide a greater level of context on the research as carried out — for example, any failed methods of experimental modelling and analysis are discussed in the thesis, but not in the journal articles due to the limitations of that publication form. Lastly, the conclusions of the journal articles have been removed, and are instead summarised in the final part of the thesis.

The final part of the thesis, *Conclusions and Recommendations*, contains a chapter summarising the key findings of the thesis, and a discussion of the limitations of the research, and recommendations for future research.

Table 1.1: Summary of journal articles included in this thesis, and their status as of publication.

Article Title	Percentage Contribution	Status (as of publication)
<i>The role of abrasion in cyclically sheared soil-structure interfaces</i>	90%	Published ahead of print
<i>Quantifying Interface Abrasion with Particle Virtualization</i>	90%	Under review
<i>Characterising Frictional Response of Irregular Abrasive Grains with 3D Attack Angle</i>	90%	Under review

Part I

**Establishing a Motivation and
Strategy**

Chapter 2

Literature Review

Literature surrounding the soil-structure interface and the mechanisms that govern its behaviour have largely analysed the global response of the system. Such investigations into variables such as the initial state, relative roughness, boundary condition, among others are functions of the relevant underlying micromechanical relationships. These studies could have gone further to investigate not just what the response of the interface is, but why the response is as such. Take, for example, the initial state of the sample. When DeJong and Westgate (2009) considered the density of the global sample, it would have been more insightful to consider the coordination number of particles, and shape factors like sphericity, which are both parameters in the global function of density. As such, this literature review will seek to reconsider the previously published interface research by way of the underlying micromechanical properties. Hence, novel hypotheses can be drawn from a new narrative, forming the motivation of an investigation that seeks to truly understand interface behaviour for the first time. As to truly understand the behaviour of the soil-structure interface, one must consider the individual behaviour of each half of the problem. The conclusions drawn from this investigation will be supported by micromechanical studies of granular mechanics, tribology and materials science. As such, this is where the literature review will begin.

2.1 Granular Mechanics

Granular mechanics research has undergone a transformation in recent years due to the advances of Discrete Element Modelling (DEM) and numerical processing

2.1. GRANULAR MECHANICS

power. With the doubling of processing power every two years (Moore, 1965), there has been an ever growing tendency to carry out computerised modelling, marginalising experimental study as the barriers to entry of quality research have shrunk. Since Cundall and Strack (1979) published their numerical model, understanding of the micromechanics responsible for the global response of a body of sand has become far better understood — following the work of McDowell et al. (1996); McDowell and Daniell (2001). Although numerical simulations are a great tool, they are only as useful as the contact mechanics that underpin them. These contact mechanics are, in general, derived from experimental findings that are over a century old (Hertz, 1882).

A fundamental divide has existed between element scale modelling and discrete element modelling. Traditionally, a crude characterisation of the shape of particles has been achieved in DEM by ‘clumping’ simple Hertzian (Hertz, 1882) spheres together, which may split under a given stress following a Weibullian (Weibull, 1951) distribution to simulate breakage. To more accurately quantify the shape of a particle, more balls are needed, which exponentially increases computation time. For every new ball added, b , to the set of balls, B , the number of computations required is C_{B+b} .

Hence, the computational aspirations of DEM studies has quickly exceeded the computational capacity available, as this method is unable to precisely replicate the real shape of particles. This is before even considering the challenge of establishing this shape in the first instance.

As such, accurate and realistic quantification of the inter-particle forces in a large granular sample is impossible. Advances such as Level Set DEM (LS-DEM) (Kawamoto, Andrade and Matsushima, 2018; Vlahinić et al., 2014), are hoped to bridge the divide between element scale and numerical modelling. Such methods are part of a class of DEM methodologies providing novel insights into granular mechanics, as an “avatar” replicates grain morphology to a better level of accuracy with reduced computational cost than traditional DEM. However, there still exists a place for element scale experimental modelling to validate these new algorithms. Continued effort in element scale particle based research is needed to inform the relationships governing numerical modelling, that in turn give greater insights into the mechanical processes.

2.1.1 Characterising Shape

Grain morphology is critical to the behaviour of granular bodies, however one all-encompassing parameter to characterise the shape of grains does not exist as physical interaction in different granular bodies is affected by three scales of particle shape (shown diagrammatically in Figure 2.1, derived from Barrett (1980)). The overall form of a particle will govern bulk volumetric response, roundness will be a factor in inter-particle friction, whilst roughness will impact the micro-mechanical interaction between each grain. More round particles have a smaller angle of repose, whereas the opposite is true for very angular particles. The most detailed and well regarded work investigating the influence of a particles' shape has been carried out by groups from the University of Hong Kong, Imperial College London and University College London. With the first investigation regarding these issues, Cavarretta et al. (2010) showed that there was a fundamental discrepancy between DEM and experimental tests of triaxial and oedometer glass media of different shape. This shows that as late as 2010, there is a need to refine the relationship between inter-particle friction and global material response.

Characterisation of particles is a difficult task, and this is reflected by the range of methods established by literature. Cho et al. (2006) summarised a series of older papers to present two key dimensionless parameters: sphericity, S , and roundness, R . Cavarretta et al. (2016) built upon this work to account for the relative roundness of a particles' contact point. The parameters are as follows, and dimensions are shown in Figure 2.2:

- Sphericity, S : A measure of the similarity between a particles height and width, when viewed in two dimensions. S can quantified as the ratio between the maximum inscribed circle, and minimum circumscribed circle of the particle.

$$S = \frac{r_{\max\text{-in}}}{r_{\min\text{-cir}}} \quad (2.1)$$

- Roundness, R : A more local measure, comparing the radius of local surface features to the maximum inscribed circle of the particle.

$$R = \frac{\sum r_i / N}{r_{\max\text{-in}}} \quad (2.2)$$

- Relative roundness R^* : Used when considering the strength of a particle when in contact with another, R^* describes the relative radius of a compressed

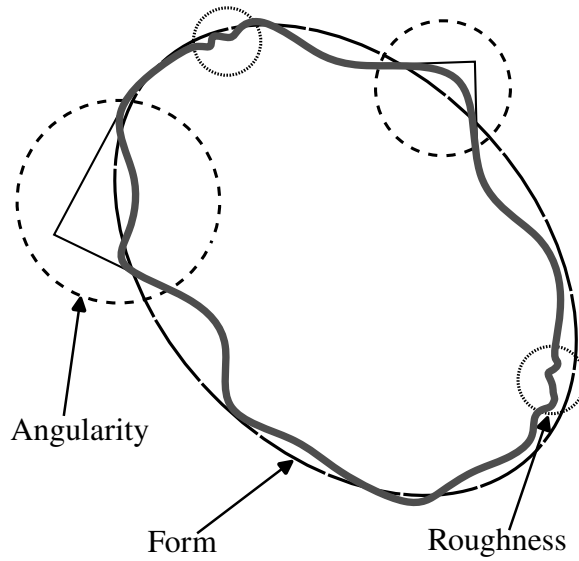


Figure 2.1: Three scales of particle shape in 2D, derived from Barrett Barrett (1980)

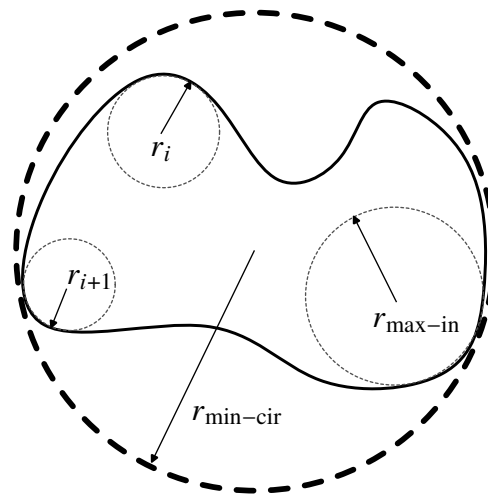


Figure 2.2: Particle shape determination (reproduced from Cho et al. (2006))

contact.

$$R^* = R \cdot r_{\max\text{-in}} \quad (2.3)$$

The sphericity and roundness of a particle can be used to form a general equation for the regularity of a particle, ρ , where values closer to 1 are more regular Cho et al. (2006).

Both Cho et al. (2006) and Cavarretta et al. (2016) concluded from their studies that particle shape had a pronounced impact upon the volumetric behaviour

2. LITERATURE REVIEW

of granular bodies. It was found for a reduction in regularity, the interval I_e between maximum and minimum voids ratio e_{\max} , e_{\min} , is greater. Samples of less regular grains are less able to rearrange, allowing for a greater area of voids in the sample. As such, there is greater plasticity in the response of angular samples, that have greater interparticle friction, than more regular samples when subject to a normal load. Consider a sample of perfect spheres, every particle contact is infinitesimally small, whilst plate like grains will have greater contact areas. If and when the frictional capacity of the sample is overcome, plastic volume losses occur as the sample moves to a lower energy state. Regular grains ($\rho \rightarrow 1$) require less energy to reorient than irregular grains. The inability to reorient, and increased frictional contact, leads to less regular particles having a greater constant volume critical state friction angle, ϕ_{cs} .

Other studies have shown similar outcomes through the use of 3D analyses investigating particle form. Bagi and Orosz (2020); Orosz et al. (2021) proposed a method to determine the orientation of a particles' surface, using a 3D shape tensor f , comprised of normal vectors, n , of each face, k , with area, A on a convex or concave polyhedral mesh.

$$f_{ij} = \frac{1}{\sum_{(k)} A^{(k)}} \sum_{(k)} \left(A^{(k)} n_i^{(k)} n_j^{(k)} \right) \quad (2.4)$$

The tensor is then able to be decomposed into a set of eigenvalues, which can be used to determine the form characteristics of the particle. The eigenvectors of the tensor represent the preferred orientation of the particle. The form parameters — shown graphically in Figure 2.3 — are compactness, elongation and flakiness.

In simple terms a flaky particle will have a major eigenvector in the direction of the large, flat face, and when dropped it is most likely to land on this face. A fully compact particle is either a perfect cube or sphere, and when dropped is just as likely to land in any orientation as the major and minor eigenvalues are equal. Such analyses are ideal for predicting the bulk behaviour of a triaxial sample as the contacts between each particle can be accurately modelled. Orosz et al. (2021) displays how a random assembly of predominately elongated particles will have a greater initial void ratio than a sample of compact particles.

Notably, no suitable analysis exists for characterising the local 3D angularity of a particle. The Shape Orientation Tensor is a fine analysis for determining the overall form of a particle, but if a region of the mesh is selected for characterisation, there will be an inherent bias applied and the tensor will be skewed. This is

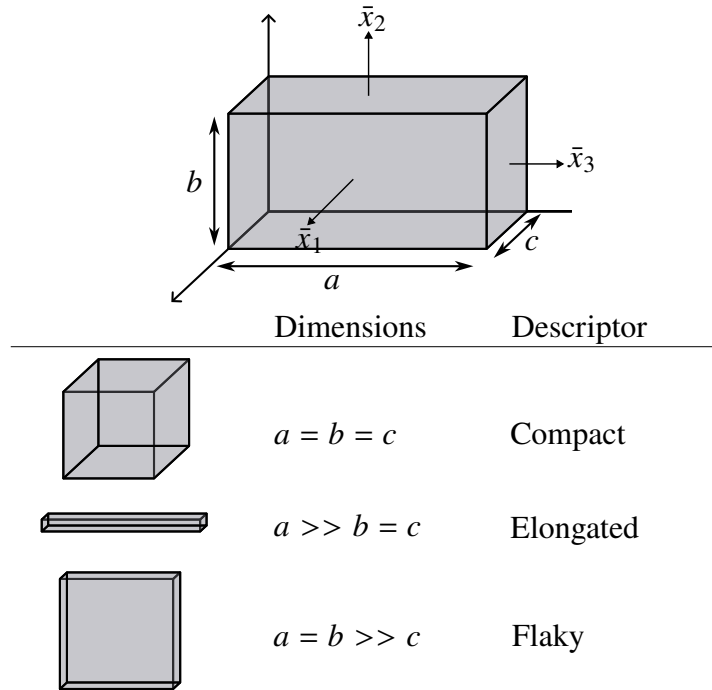


Figure 2.3: Form parameters for extreme 3D bricks, derived from Orosz et al. (2021)

identified in as a strength by Orosz et al. (2021), who state:

“It has the advantage that small sharp corners have less influence on form indices.” (Orosz et al., 2021)

However, it is these small sharp corners which are of interest to the local angularity of a particle, which govern the micromechanical behaviour. As will be established subsequently, the angularity is of crucial importance to the abrasive behaviour of a particle, and the ability to accurately parametrise the local angularity of a particle is essential to the development of a robust model for the abrasive behaviour of granular materials.

Surface roughness has some influence over the inter-particle friction of adjacent grains μ_u Senetakis et al. (2013) was the first study in a series by the same authors researching inter-particle shearing and found that over repeated shearing of a single grain, a reduction in the friction angle occurred. It was suggested that due to the breakage of asperities from the surfaces of the particles, surface roughness decreases and accounts for the fall in inter-particle friction angle, a claim that is supported by the experimental work of Nadimi and Fonseca (2017), and Cavarretta et al. (2010) which established this behaviour from surface profiling

2. LITERATURE REVIEW

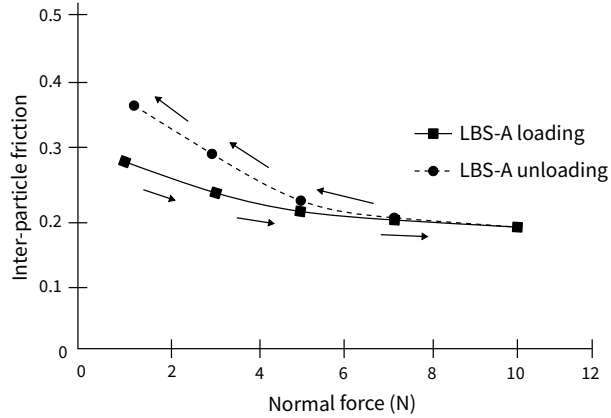
after purely normal loading. Nardelli and Coop (2019) confirms this finding from the more general conclusion that the coefficient of friction is controlled primarily by the surface roughness of grains. Hence, as asperities on the surface break off, creating a smoother surface, the friction angle is expected to fall.

Sandeep and Senetakis (2018) note that the repeated shearing of two grains in tangential loading at low normal loads did not influence inter-particle friction as greatly as higher normal loads. It was observed that ploughing of the counter-body, in this case the quartz sand grain of equivalent hardness, occurred only at the higher contact stresses present in the higher load tests.

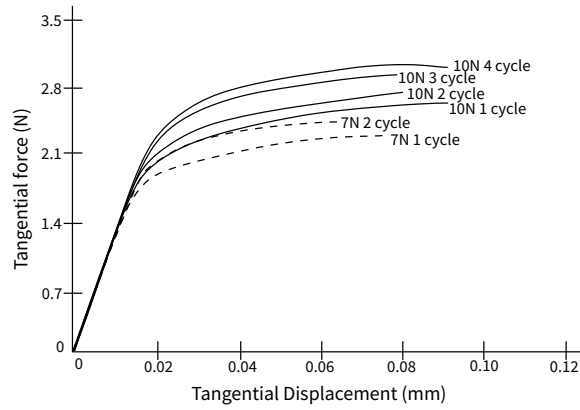
Figure 2.4a displays the variation in inter-particle friction found by Sandeep and Senetakis (2018) for the tests on a single LBS Fraction A grain pair during loading and unloading. Hysteresis is present in the unloading phase at lower normal loads, as the inter-particle friction increases upon unloading — where the particle is sheared over the previous shear displacement track. Results suggested that the unload stress response was a function of the maximum normal stress applied during shear, similar to that of an overconsolidation ratio. The value of interparticle friction decreased slightly with an increase in normal load, this could be due to the resultant tangential forces being large enough to break the asperities on the surface, whereas this is not possible at smaller normal loads. A similar observation was made by Nardelli et al. (2017), where particles of more brittle Eglin sand were studied. Figure 2.4b shows the tangential force vs. displacement curves for repeated shear on LBS pairs at 7 N and 10 N. Note the increase in the steady state tangential force after each cycle, which can be linked to the increase in interparticle friction upon unloading. It shows that accumulative wear between two equivalently hard bodies, increases roughness and leads to an increase in friction, in this case interparticle friction. Sandeep and Senetakis (2018) note that this is not the case for smaller normal loads, presumably as there is not enough energy expended to wear the surface.

2.1.2 Particle Breakage

Particle breakage can be viewed from two scales; first the macroscopic change in sample characterisation, for example voids ratio, size distributions; second, the particle scale change in resistance to loading. Literature regarding the two scales will be considered separately, beginning with the particle scale, where insights can give greater meaning to the research of the macroscopic scale.



(a) Change in inter-particle friction during loading and unloading for various normal loads for a single LBS-A pair



(b) Tangential force vs. displacement for repeating shear tests at constant normal load

Figure 2.4: Plots reproduced from Sandeep and Senetakis (2018)

The form of a particle is a key factor in determining the strength of particle strength as it governs the stress field experienced by the grain, under loading. Cavarretta et al. (2016) concluded in their investigation into the relevance of roundness to crushing strength, that roundness was a key descriptor of the particle. It was shown that for particles with equivalent size of maximum inscribed circle, $r_{\max-in}$, rounder particles are capable of withstanding greater loads. Russell et al. (2009) gives credence to this experimental finding which said that for a brittle sphere, the nucleation point of particle crushing — in platen loading — is where the ratio of second deviatoric stress invariant and the first stress invariant is a maximum. This point lies close to the surface of the applied contact load. The

2. LITERATURE REVIEW

invariants are defined as:

$$\iota_1 = \sigma_x + \sigma_y + \sigma_z \quad (2.5)$$

$$\iota_2 = \sigma_x\sigma_y + \sigma_y\sigma_z + \sigma_z\sigma_x - \tau_{xy}^2 - \tau_{xz}^2 - \tau_{yz}^2 \quad (2.6)$$

To explain further, tensile forces emerge in particles undergoing crushing when cracks begin to form as molecules are forced away from each other. Russell et al. (2009) provides a mathematical explanation for the point at which these cracks nucleate. It is the point where the stress in the principal axes ($\sigma_x, \sigma_y, \sigma_z$) greatly exceeded by the shear force generated in the molecular lattice. More critically, this nucleation point occurs just inside of the sphere, close to the contact point with the platen. It follows that this point requires more energy to reach for spherical ($S = 1$) particles as the intermediate (second) principal dimension is equal to the first, whereas in sub-spherical ($S < 1$) particles, this point is easier to reach as one of the principal axes has lower strength, i.e. is shorter. Russell et al. (2009) used this same analysis for non-spherical and irregular particles, noting that the crushing for a particle with multiple contacts is “controlled primarily by the largest contact force acting on a particle”. This analysis has similar themes to that of Orosz et al. (2021) with the Shape Orientation Tensor. A stress field analysis showed that the location and magnitude of lesser contact forces had a minimal impact upon the crushing of grains. From this analysis, it was concluded again that crushing nucleation lies close to the contact load where the ratio of ι_2/ι_1 was a local maximum.

In the remainder of this subsection the review methodology mirrors that of Cavarretta et al. (2016), although individual sources have been reviewed in their own right. It is widely accepted that the Brazilian breakage criteria for a disc-sample of diameter d and thickness t_p , is suitable for predicting the tensile crushing strength σ_t of spheres and rods under a load N_F between two flat platens (Fairhurst, 1964):

$$\sigma_t = \frac{2N_F}{\pi dt} \quad (2.7)$$

However, for the more complex geometries of naturally occurring grains, the Brazilian criteria is not sufficient. A simplified version of Equation 2.7 can be used for granular media of average diameter \bar{d} to give a nominal strength σ_f :

$$\sigma_f = \frac{N_F}{\bar{d}^2} \quad (2.8)$$

This approximation is still widely used, though can greatly overestimate the actual tensile stress at failure. Lee (1992) found through experimentation that the failure tensile stress of a cylindrical rock sample was overestimated by up to 60 % using Equation 2.8. Lee showed that the nominal strength decreases with an increase in size, finding a linear relationship between $\log(\sigma_f)$ and $\log(d)$ such that

$$\log(\sigma_f) = a + b \log(d) \quad (2.9)$$

where a and b are coefficients of the \log_{10} strength of the particle at unit value of d , and the scale of size effect on strength, respectively. A typical value of b for Leighton Buzzard Sand (LBS) is given as -0.357.

McDowell and Bolton (1998) used the data of Lee (1992) to show consistency with a Weibullian distribution of particle fracture, leading to a micromechanical explanation for the normal compression line which will be covered subsequently. The expression for the survival probability $P_s(V)$ of a given particle volume V is

$$P_s(V) = \exp \left[-\frac{V}{V_0} \left(\frac{\sigma}{\sigma_0} \right)^m \right] \quad (2.10)$$

where m is the Weibull modulus, which shows the uniformity of tensile strength of the sample grains, and σ is the yield stress in normal compression (Weibull, 1951). The parameters b and m seem to describe similar relationships, McDowell et al. (1996) showed the relation between Equations 2.9 and 2.10 by giving $b = -m/3$. Cheng et al. (2003) conducted a DEM study of clumped spheres in particle compression, which validated the relationship and Weibullian distribution of nominal strength. It was shown that $m = 3$ and $b = 1$, where b is a similar order to the value found for LBS grains.

More recent studies have acknowledged flaws in the Weibull method for predicting grain failure in real samples. For Weibull breakage to be a correct assumption, the breakage of asperities need to not occur, though Senetakis et al. (2013) showed this does occur. It was found that over repeated shearing of a single grain, a reduction in the friction angle occurred. It was suggested that due to the breakage of asperities from the surfaces of the particles, surface roughness decreases. Bažant et al. (2009) identified the post-yield hardening of quasi-brittle materials such as sands and glass, where Weibullian theory requires the bulk

2. LITERATURE REVIEW

failure of the particle. Indeed on the conclusions of Lee (1992); McDowell and Bolton (1998); McDowell et al. (1996), one would suspect that the crushing of grains initiates at the point of maximum tensile stress in the particle. This is not the case however, as Russell et al. (2009) and Equations 2.5, 2.6 show. However, for experimental analyses the first and second invariant method is too complex to calculate Hence, Cavarretta et al. (2016) make the assumption that crushing must begin in the plane experiencing maximum tensile stress. The size of the particle for this analysis is calculated from the three principal diameters d_{1-3}

$$d = (d_2 d_3)^{0.5} \quad (2.11)$$

The theory behind this assumption is that as a particle in platen loading will lie on its axis of largest stability, the smallest diameter d_3 , and the largest tensile stress will be experienced in the smaller of the two horizontal axes d_2 . A representation of this is shown in Figure 2.5. Similarly to before, this assumption could be updated with the Shape Orientation Tensor, Equation 2.4, from Orosz et al. (2021), which further shows the benefit of 3D analyses of shape.

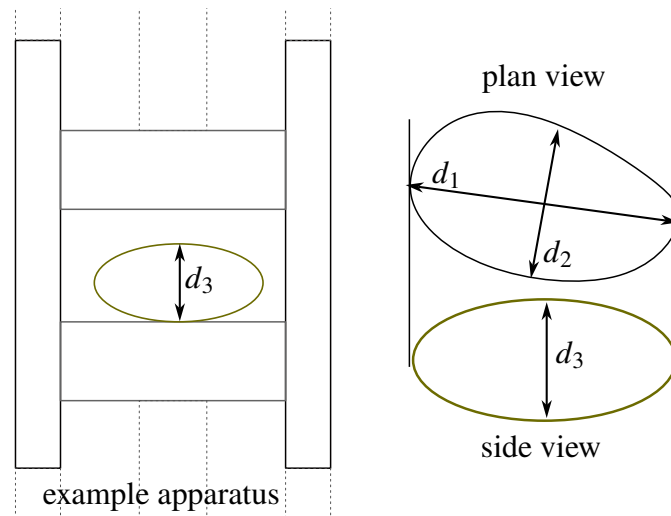


Figure 2.5: Representation of principal axes in platen crushing

The Hertzian behaviour, or rather, lack of Hertzian behaviour in inter-platen compression was analysed by Antonyuk et al. (2005). With reference to Figure 2.6, it was concluded, from comparison of theoretical calculations to experimental results, that four stages of a particle's compression exist. In phase I the breakage of asperities occurs in pre-Hertzian response, as described by Cavarretta et al. (2010) from normal loading of two grains, until a threshold load is reached and Hertzian response begins throughout Phase II. In phase III, after a critical force

2.1. GRANULAR MECHANICS

has been reached, plastic deformations begin to occur and equivalent increases in the displacement of the platens results in a lower equivalent increase in force than according to Hertzian theory. Phase IV arrives when failure of the particle is reached.

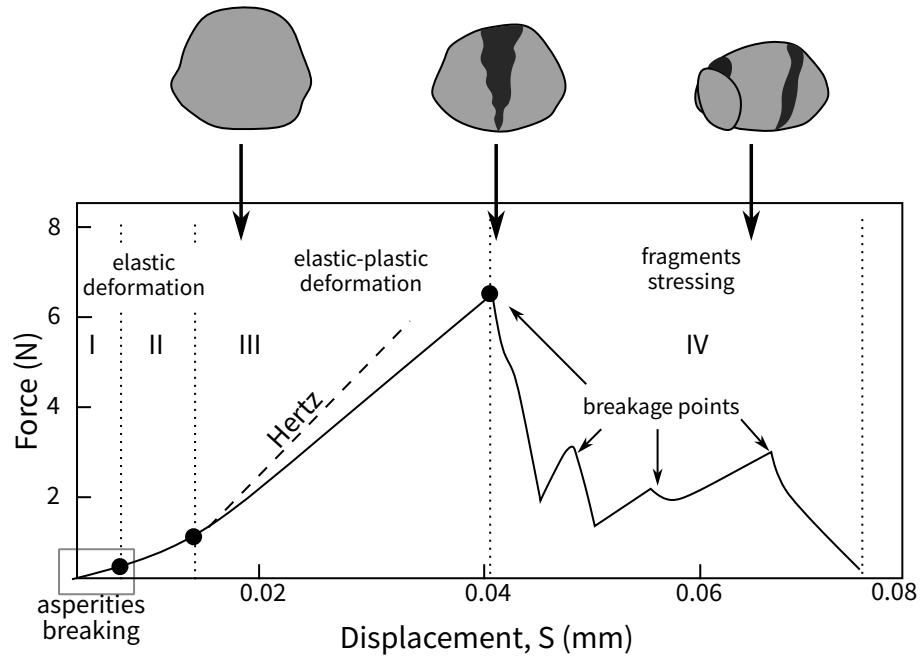


Figure 2.6: Force-displacement curve of artificial grain in compression, reproduced from Antonyuk et al. (2005)

Cavarretta et al. (2016) concluded from their experimental and numerical study into the effect of roundness on crushing of grains, that the widely believed logic of smaller particles having a higher failure stress has the wrong motivation. Although it is true that smaller particles tend to have a higher failure stress, this is not necessarily due to the lower probability of material flaws being present. Bulk crushing failure is heavily influenced by the relative curvature of contacts, an effect which is magnified in particle-particle loading as opposed to platen loading. Cavarretta et al. (2016) found that all being equal, the crushing force is proportional to the square of the relative radius of contact R^* (Equation 2.3). Although relative radius, R^* , is not exactly proportional to size, smaller particles will tend to have lower R^* values. Moreover, d_3 and R^* are found to be inversely proportional. For a population of grains with same d_3 , rounder grains have larger R^* values and fail at larger loads. In a population of grains with the same roundness, larger grains fail at larger loads due to having larger R^* values. This relationship, witnessed experimentally, supports the expansion of Equation 2.3

from Cho et al. (2006).

$$R^* = R \frac{d_{\max}}{2} \quad (2.12)$$

where d_{\max} is equivalent to the maximum inscribed circle ($r_{\max-in}$ in Figure 2.2), or more simply d_3 .

In an assembly of identical irregular particles, Russell et al. (2009) suggested the geometry has limited impact on crushing, where denser or more stable assemblies, with a greater coordination number generally have lower contact stresses. In particle-scale analyses, the coordination number refers to the stability of the individual particle. Todisco et al. (2017) carried out an experimental study into the effects of a change in the number of contacts on LBS and sandstone particles in diametrically loaded crushing. The coordination number was manipulated by loading the grains between sets of hardened steel balls, with a coordination number of 2 (platen loading), 4 (3 steel balls below, one above) and 6 (3 steel balls below, 3 above). The study concluded that the strength of the relatively harder LBS grains was more influenced by local roundness or angularity, rather than sphericity for softer limestone grains. Todisco et al. (2017) did note a difference in the crushing behaviour of the LBS and limestone particles, which was attributed to the hardness of the two grain types. It was found that hard grains did not deform during loading as stress concentrations built, whereas the softer limestone grains moulded relative to their counterbody, be that the steel balls or platen. As the contact area changed during the limestone loading, more of the particle mass was invoked to resist the stress applied. Across the different coordination numbers tested, it was concluded that “an increase in the number of contacts induced an increase in particle stress at failure”. This also changed the failure mode of the particles. Lower coordination number tests, of 2 or 4, could fail catastrophically by fragmentation as well as by splitting, though more confined tests, of a coordination number of 6, would mainly fail by splitting. For the well confined particles, it was shown that the fragments would be held closer together than lower coordination split particles. This corroborates conclusions drawn by Bandini and Coop (2011) which proposed that particle breakage can shift the critical state line for triaxial samples, but due to well confined broken fragments remaining in close proximity to their unbroken locations, there is similarity between the broken and unbroken global response. If the samples were reconstituted, there was a widely different response. The findings of Todisco et al. (2017) broadly agree with the other literature presented so far. If the strength of a soil body is a dependent upon the

strength of individual grains, then more stable particles, which could be due to an increase in regularity and reduction in voids ratio, will compose a strong soil body. Sharper, more acute contacts will have much greater magnitude of stresses near to the contact points, where the ratio of I_2/I_1 can reach a maximum. For the hard LBS grains that build large stress concentrations and suddenly fail after Hertzian loading, similar to Figure 2.6, sharp contacts with a low R^* value are more likely to yield than more rounded particles.

2.1.3 Crushing of Granular Bodies

Having reviewed the micromechanics governing particle breakage, the macroscopic breakage or crushing of granular bodies can be considered.

Before the rise of DEM, macroscopic analyses of the crushing of granular media was conducted by experimentation and evaluation of the particle size distribution prior to and after compression testing. Hardin (1985) investigated the crushing behaviour of a variety of triaxial sand samples, developing a ‘breakage index’ based on the change in particle size distribution of the samples. By making the traditional assumption that a particle’s strength is a function of its size and also that only particles bigger than the largest silt size of 0.074 mm could crush, Hardin defined the breakage potential of a particle as:

$$b_p = \log_{10} \left[\frac{D}{0.074} \right] \quad \text{for } D \geq 0.074 \text{ mm} \quad (2.13a)$$

$$b_p = 0 \quad \text{for } D < 0.074 \text{ mm} \quad (2.13b)$$

where the entire potential for breakage is given by

$$B_t = \int_0^1 b_p df \quad (2.14)$$

Thus, total breakage B_t or the difference between particle size distribution curves, through each fraction f , before and after loading can be calculated as

$$B_t = \int_0^1 (b_{p0} - b_{pt}) df \quad (2.15)$$

Hardin (1985) found, paving the way for later published studies showing larger particles being more susceptible to crushing (Cavarretta et al., 2016), total breakage was approximately proportional to breakage potential, defining the

2. LITERATURE REVIEW

relative breakage

$$B_r = \frac{B_t}{B_p} \quad (2.16)$$

This led to Hardin (1985) forming a set of equations to give the total breakage as a function of, particle size distribution, effective stress and stress path (τ_0, σ'_0) , initial voids ratio e_i , particle shape n_s , and particle hardness h

$$B_t = f(B_p, \tau_0, \sigma'_0, e_i, n_s, h) \quad (2.17)$$

All of these parameters have been shown to have an effect on soil behaviour from a particle scale, giving support to the reframing of global analyses from a micromechanical perspective.

Continued effort has been given to the understanding of particle size distribution and its effects on global soil behaviour. McDowell et al. (1996) considered the continued crushing of a soil sample of granular media, and established theoretically that eventually a fractal dimension will occur where voids are completely filled with smaller and smaller particles. As such the distribution for the number of particles N of size L , greater than d is given as

$$N(L > d) = Ad^{-D} \quad (2.18)$$

where D is the concluding fractal dimension, commonly in the range of 2 to 3 for granular materials, and A is a constant of proportionality that varies with every test. Equation 2.18 could be used as the basis for giving normal compression curves resembling those found experimentally. This development provided a numerical basis for the distribution of particle sizes with successive increases in the stress level, creating the hypothesis that plastic hardening is due to an increase in number of particle contacts occurring as the sample compresses with particle breakage. Hence, the proportionality between compression of a granular body and the logarithm of applied stress can be explained as a function of four material properties: the fractal dimension D ; the variability in particle strength m , referred to by Lee (1992); friction angle of the soil ϕ ; and particle toughness Γ . As McDowell and Bolton (1998) summarised:

“successive fracturing of the smallest particles under increasing one-dimensional stress . . . provides an insight into the existence of linear ‘normal compression lines’ ” (McDowell and Bolton, 1998)

2.1. GRANULAR MECHANICS

In other words, the current yield stress of a granular sample is determined by the tensile strength of the smallest particles (McDowell and Bolton, 1998). These relationships were formalised in McDowell (2005); McDowell and Daniell (2001); McDowell and de Bono (2013) by numerical simulations. It was shown that the plastic compressibility index λ or the slope of the 1D normal compression line is independent of initial grading of the soil, as all particle distributions move towards a fractal dimension of 2.5 with continued crushing (McDowell and Daniell, 2001). Furthermore, from DEM analysis, λ was found to be solely dependent on the size effect of average particle strength, as the smaller a particle is, the statistically stronger it is (McDowell and de Bono, 2013). Note this does not conflict with the findings of Cavarretta et al. (2016), and the true reason for size dependency of strength of soil particles. For the first time also, (McDowell and de Bono, 2013) was able to prove that both the emergence of a fractal distribution, and dependency of the slope of the normal compression line on particle strength and size to hold in three dimensional compression.

Other studies have been conducted with a more applied methodology of specific stress states and relative changes in fine material. Ghafghazi et al. (2014) determined from a series of triaxial tests on sand that the shearing of a sample, at a sufficient stress level to cause particle breakage, will cause the critical state line (CSL) to make a downward parallel shift in $e - \log p'$ space. Furthermore it was found that the magnitude of the shift is correlated with the increase in fines content, a finding that agrees with that of (McDowell and de Bono, 2013). Hence, each gradation of particles can be associated with a critical state line. Consideration was given by Ghafghazi et al. (2014) to the difference in behaviour of samples on the dense and loose side of the critical state. Two assumptions were made in the analysis framework, firstly that particle breakage does not occur until the contractile capacity of the sample has been exhausted by rolling and sliding. This results in a minimisation of the voids ratio as broken particles move into voids to avoid loading. In a loose sample, the end of contraction is associated with the critical state, whilst in a dense sample, a dilative phase follows. Particle crushing will begin for either sample after the contractile phase, so long as the stress level is high enough. The implication of the assumption is that the change in voids ratio occurring through breakage Δe_b , which is independent of the stress of the sample, must be equal to the shift in CSL intercept $\Delta \Gamma$. The second assumption is that breakage only occurs when a soil-specific stress state is reached. To test this assumption, samples were sheared at high stress to impose breakage, shifting the

CSL, before removing load, reforming the sample and testing at a stress state lower than the assumed breakage limit. Results from Ghafghazi et al. (2014) showed that the CSL intercept $\Delta\Gamma$ moved down after reforming the samples, without an associated change in the plastic compressibility index λ . These results support the conclusions of a similarly focused DEM study conducted by Wood (1991). Furthermore, the two assumptions regarding the onset of particle crushing during shear were proved to hold during experimentation.

Figure 2.7 displays the conclusions of the macroscopic scale work diagrammatically. Consider a triaxial sample under isotropic loading. At the point e_0 on the initial λ -line λ_0 the particle distribution is poorly graded with a corresponding CSL intercept Γ_0 , representing the stress history of the sample. Suppose the sample to be sheared under drained conditions at a deviatoric stress q that imposes breakage upon the sample, causing a downwards shift the CSL. The sample is then unloaded and reconstituted to evenly distribute the fine particles that may have been trapped under force chains (as per Bandini and Coop (2011)). Note, this step is avoided in McDowell and de Bono (2013) where simulations do not assume that broken particles are not retained in situ. The fine material is now distributed within the voids, as the sample becomes more evenly graded, and moves closer to the fractal dimension of $D = 2.5$. Hence, there is a lower voids ratio of e_s post-shearing, at the same normal stress condition, with lower corresponding Γ_s , where $e_0 - e_s = \Delta e_b$. Recalling that a samples strength is defined by the strength of the smallest particles in the loading matrix (McDowell and Bolton, 1998), a shift downwards in CSL generates a new, larger yield surface. That is to say, a larger deviatoric stress q will be needed to impose breakage on the sample.

2.1.4 Granular Force Chains

Assemblies of granular particles are subjected to loads a nominal stress condition, but the stress state within the assembly is not uniform. The stress state within a granular assembly is a function of the particle size distribution, the particle shape, and the particle strength. When attempting to link macroscopic scale element testing to micro/particle-scale testing, an awareness of the range of stresses on individual grains in the assembly is required. Take for example Figure 2.8a, a soil container with a constant normal stress σ_n applied through a top cap, which is supported by an assembly of rounded sand particles, against a planar surface. The yellow lines are indicative of a force chain, where the most upright

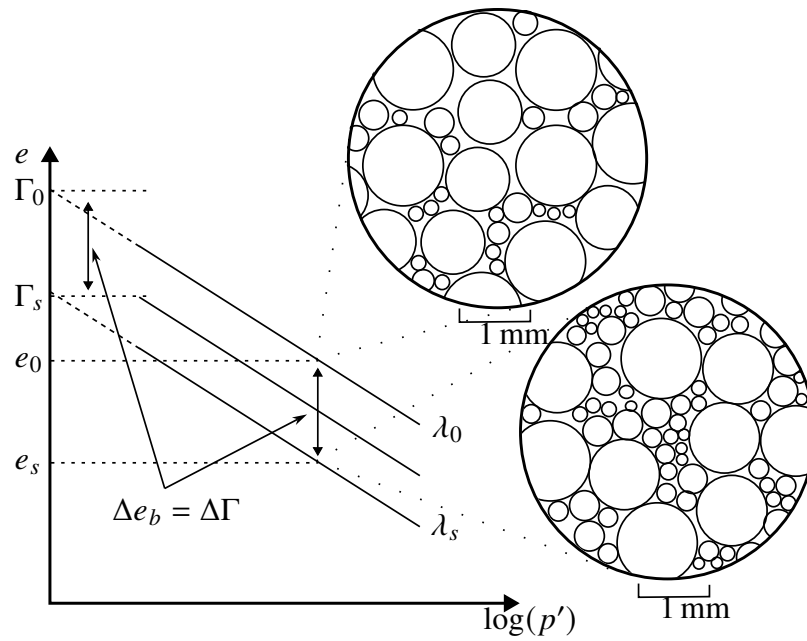
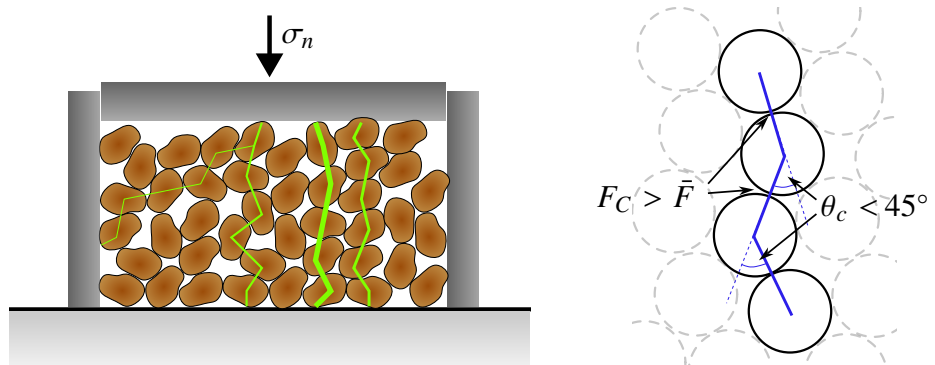


Figure 2.7: Diagram summarising the successive movement of parallel critical state lines in relation to the fractal crushing of granular material



(a) Diagram summarising the successive movement of parallel critical state lines in relation to the fractal crushing of granular material
(b) Identification and evolution of force chains, reproduced from Xu and Liu (2019)

Figure 2.8: Diagrammatic and mathematical definition of force chains

2. LITERATURE REVIEW

chains are strongest. Inter-particle friction is responsible for passing normal and shear loads through a soil body. Xu and Liu (2019) carried out a DEM analysis of the evolution of force chains in a granular sample. For this study and in others (Seyedi Hosseininia, 2012), a strong force chain exists where the contact force between particles, F is greater than the global average \bar{F} and the angle between particle centres θ_c is less than 45° . Figure 2.8b shows this definition diagrammatically. As samples undergo volumetric contraction from loading, force chains will buckle as θ_c increases, reducing the average length of force chains. Xu and Liu (2019) concluded on variation of the interparticle coefficient of friction in their biaxial compression DEM samples, that the larger the value of μ , the more vulnerable force chains are to damage during loading. This is due to the greater tendency to dilate under shear load with a higher inter-particle friction. As such the strain softening effect, or the difference between peak and ultimate shear stress, is more pronounced for a greater μ . A similar evaluation was reached in Section 2.1.1 on consideration of rearrangement capacity. Such an observation was also noted by Barreto and O’Sullivan (2012), which concluded peak shear strength of the sample ϕ_{peak} rises with an increase in μ . The same study also found that as μ increases, the coordination number at critical state reduces. Where critical coordination number:

$$Z_{\text{crit}} = \frac{2N_c}{N_p} \quad (2.19)$$

where,

N_c = number of contacts

N_p = number of particles

In other words, a higher inter-particle friction reduces the amount of particle contacts needed to support a given shear stress. As such, some particles will not be part of a force chain, and hence will not contribute to the load capacity of the sample.

Zhang and Evans (2018) carried out a 3D DEM analysis of the evolution of force chains in a granular sample, sheared against a structural interface, in the form of a series of increasingly rough piles. It was shown that the contact force between grains and the pile could be plotted as a probability function, where the probability of a contact force, f , follows Mueth et al. (1998), given by:

$$P(F) = a \left(1 - b e^{-f^2}\right) e^{-\zeta f} \quad (2.20)$$

where a , b and ζ are fitting parameters. For a small number of particles the normalised contact force could be in excess of $10\times$ the average contact force. This

supports the findings of Barreto and O'Sullivan (2012), where some particles will experience far higher contact forces than the mean, and become critical in the macroscopic behaviour of the system.

2.2 Tribology and Metallurgy

A key factor governing response of the interface to shearing, is the mechanical wear experienced by the interface plate itself. This area of material science is referred to as tribology. A subset of this category considers the abrasive wear of materials by particulates, which usually would be the result of asperities in one surface in contact with another. Since the 1960s, these types of wear have been categorised as either two or three-body abrasion. An early definition of three-body abrasion was given as 'wear by free abrasive particles moving between an interface and counter-body' (Rabinowicz et al., 1961). It is hypothesised that this wear is a key influence into the behaviour of metal interfaces (Petty and Heron, 2020). Gates (1998) presented a critical discussion into the nomenclature of two and three-body abrasion. It was concluded that the categorisation lacks clarity, and has become a catch-all term for particles moving across a material, causing abrasive wear. Instead, the type of wear upon an interface should be classified by the severity of abrasive wear, and the dominant mechanisms of wear. Gates (1998) proposed a classification scheme for abrasive wear, which is shown in Table 2.1. Gates provides a clear framework for distinguishing between the various wear modes of abrasion, showing that parameters that influence particle-particle behaviour in the realm of geotechnics, influence the wear mechanism of materials. Helpfully, analyses reviewed in Section 2.1 provide a way to quantify the differences in particle size, constraint, shape and contact stress. As such, defining the wear mode of an interface can be achieved using the Gates (1998) framework.

A question still remains however, certainly for those without a background in materials science, in what scenarios would two and three-body abrasion occur? Hutchings and Shipway (2017) provides a comprehensive summary of abrasive wear, which occurs in many guises in a wide range of engineering issues. Figure 2.9 displays the difference between two and three-body abrasion. Two-body abrasion occurs when hard particles, fixed to the counterface, damage the first body of interest. These particles could be protuberances that make up a rough surface or particles mechanically fixed in place. Three-body abrasion occurs when hard particles, the third body are free to roll and slide between the first body of interest

and a second constraining body. Note in two-body abrasion such as that shown in Figure 2.9a, the particles can only slide over the first body and are unable to rotate. This can be easily related to the Gates (1998) framework in Table 2.1, where it is said that unconstrained particles, like shown in Figure 2.9b would cause three-body abrasion. The Gates (1998) framework also lists partially constrained particles causing high stress three-body abrasion, this presumably would be due to particles constrained by large force chains, where the energy required to rotate is greater than the energy required to damage the first body or deform plastically as outlined in Section 2.1.4.

2.2.1 Abrasive Wear

In this section the literature of Hutchings and Shipway (2017) will be presented and commented upon to provide better access to those from a non-materials science background.

Relative Hardness

The wear rate of a surface is dependent on the difference in hardness between the surface H_s and the abrasive particle H_a (Hutchings and Shipway, 2017). We can then define the relative hardness R_H as

$$R_H = \frac{H_a}{H_s} \quad (2.21)$$

Figure 2.10 illustrates the conditions under which the particle or surface will plastically deform in abrasion. The wear rate of a material is significantly increased when the relative hardness is greater than ~ 1.2 , as the figure indicates.

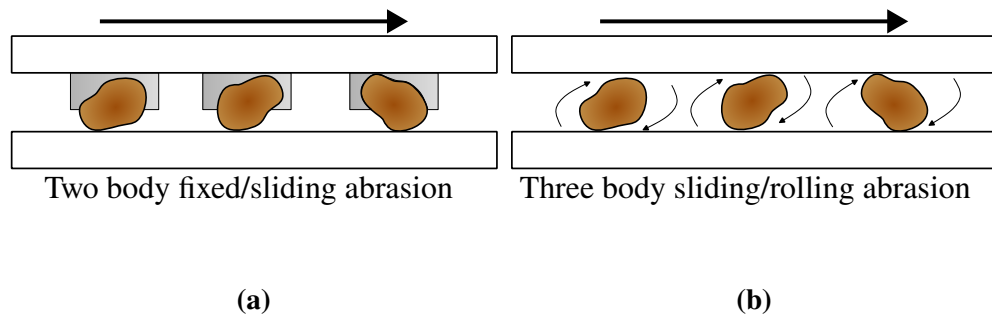


Figure 2.9: Illustration of the differences between (a) two-body abrasion, (b) three body abrasion, reproduced from Hutchings and Shipway (2017)

Table 2.1: Classification of abrasive wear, adapted from Gates (1998)

	Abrasive wear mode		
	Mild	Severe	Extreme
Particle Size	Small	Moderate	Large
Fixity	Unconstrained	Partially constrained	Strongly constrained
Particle Shape	Rounded	Sharp	Sharp
Contact Stress	Low	Moderate	Very high
Dominant Mechanism	Microploughing	Microcutting	Microcutting / microfracture
Equivalent Terms	Low-stress abrasion Scratching abrasion Three body	High-stress abrasion Grinding abrasion Three body	Gouging abrasion Two body
		Two body	

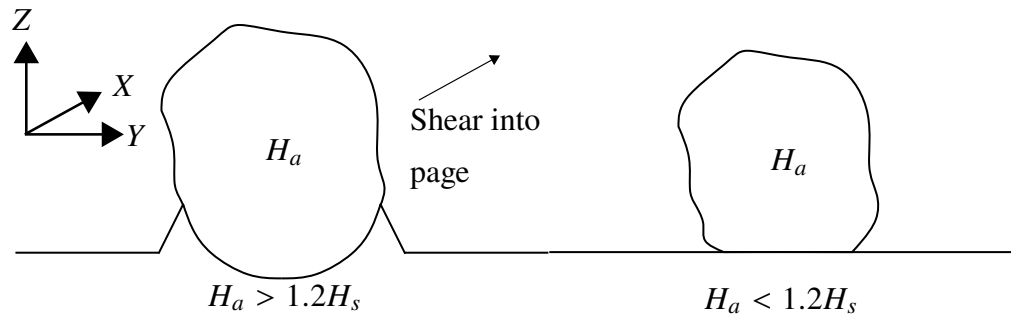


Figure 2.10: Illustration of contact between a grit particle under normal load and a plane surface, reproduced from Hutchings and Shipway (2017)

Proof of this fact can be derived from the mechanics of materials. A body will undergo significant plastic deformation when the contact pressure reaches three times its uniaxial yield stress Y (Hutchings and Shipway, 2017). This can be more easily referenced as the point at which plastic flow occurs from the surface in a Vickers hardness test, or indentation hardness. Plastic indentation will occur so long as the particle can sustain the contact force of at least $\sim 3Y$.

For a spherical particle against a flat surface, the maximum contact pressure is said to be roughly 0.8 times the hardness value of the particle Hutchings and Shipway (2017). It is hypothesised that a near-spherical particle will cause indentation on a surface if the surface hardness $H_s \leq 0.8H_a$. Quartz, the constituent material of Leighton Buzzard Sand, has a Vickers hardness value of 750 HV to 1200 HV, whilst grade 304 stainless steel has been found to have a Vickers hardness value of 100 HV to 200 HV. Evidently, for a quartz particle on steel, plastic deformation of the steel will occur should the normal load be high enough.

Particle Size and Shape

It is unsurprising, considering the role of particle size and shape on granular mechanics, that it plays a role in the abrasive wear of materials. For those with acute interest in tribology Hutchings and Shipway (2017) concedes “angularity is not straightforward to define”. This is in broad agreement with those interested in granular mechanics, as reviewed in Section 2.1.1. In general, angular particles cause a higher wear rate on surfaces than rounded particles, though with this are more susceptible to breakage (Cavarretta et al., 2016; Coop et al., 2004). Hard granular abrasives found in most occurrences of soil-structure interfaces will vary

in size dramatically, as such a general trend is needed to consider this range. Misra and Finnie (1981*b*) considered experimentally the wear rate of materials with abrasive particles ranging from 10 μm to 250 μm in size. It was shown that for particles smaller than 10 μm the wear rate in both two and three-body abrasion significantly decreased. This could be attributed to the general trend of smaller particles being rounder in nature (Cavarretta et al., 2016), or potentially due to the size effect of moving dislocations in the materials lattice structure. Causing plastic flow in a material is more difficult as the atomic scale is approached than over larger areas.

Plastic Deformation

A simple model for abrasive wear by plastic deformation has been derived by Hutchings and Shipway (2017). Consider a conical abrasive being forced through a ductile surface creating a groove, shown diagrammatically in Figure 2.11. The normal load w is supported by a pressure P causing a plastic deformation of the surface where,

$$w = P \frac{\pi a^2}{2} = \frac{1}{2} P \pi z^2 \tan^2 \alpha \quad (2.22)$$

The volume of displaced material by the abrasive is equal to the volume of the cone embedded in the surface $lax = z^2 \tan \alpha$ over the length of shear l . In reality, some fraction η of the displaced material will be removed as debris. This has been referred elsewhere as the cutting-plasticity ratio, the ratio between plastic flow and cut material (Lindroos et al., 2015). Hence, the volume of debris material can

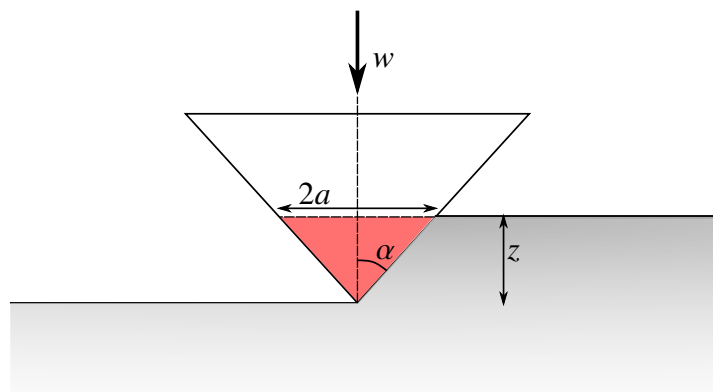


Figure 2.11: Geometry of contact between conical abrasive and surface in elevation view, reproduced from Hutchings and Shipway (2017)

2. LITERATURE REVIEW

be described as

$$q = \eta z^2 \tan^2 \alpha \quad (2.23)$$

The embedment depth, z , can be substituted from Equation 2.22 to give

$$q = \frac{2\eta w}{\pi P \tan \alpha} \quad (2.24)$$

Over a number of particles, assuming that plastic flow occurs when stress exceeds the indentation hardness $P \simeq H_s$, the total volume removed per unit shear distance, Q , is

$$Q = \frac{\Psi W}{H_s} \quad (2.25)$$

where W is the total applied normal load; the dimensionless wear coefficient Ψ depends on the cutting–plasticity ratio η and geometry of the particle, here quantified by α (Hutchings and Shipway, 2017). Values for Ψ have been found experimentally and vary with material and deformation mode. Materials in two-body sliding abrasion tend to have higher wear coefficients than three-body by about one order of magnitude (Hutchings and Shipway, 2017). For comparison among different materials the specific wear rate $psi = \Psi/H$ can be considered, with units $\text{mm}^3 \text{N}^{-1} \text{m}^{-1}$. Also the specific energy for material removal U is used

$$U = \frac{\mu W}{Q} = \frac{\mu}{\psi} \quad (2.26)$$

where μ is the coefficient of friction. For two-body abrasion of metals, μ is in the range of 0.4 to 1, whilst for three-body abrasion it lies in the range of 0.2 to 0.5 (Hutchings and Shipway, 2017). Equation 2.25 suggests a relationship between the volume of material lost and the shear distance and normal load applied. In a study of ductile metal abrasion Misra and Finnie (1981a) confirmed the proportionality of the quantities. It is also suggested by Equation 2.25 that there is inverse proportionality between wear rate and hardness. Experimental study by Khrushov (1957), showed linearity between the hardness of pure metals and relative wear resistance. Similarly to Moore (1974), it was shown that wear resistance increases with hardness, even in alloyed steels of varying pearlitic and martensitic content, but at a different rate than of pure metals, that does not fall through the origin. This can give the incorrect conclusion of soft steels ($H \rightarrow 0$) having a wear resistance, similar to the incorrect conclusion of effective cohesion in sands emanating from drawing a y intercept.

Returning to the abrasive and surface in Figure 2.11, the material at the worn surface will have been strain-hardened by plastic flow. Data from Moore and Douthwaite (1976) showed that shear strains decrease with depth into the material, as atoms in the metallic lattice are dislocated in greater density close to the surface. An experimental single and multiple scratch test study (resembling fixed particle sliding abrasion) corroborated this, finding from that as a result of shear strains hardness decreases with depth from the surface (Lindroos et al., 2015). Due to strain hardening, flow stress at the surface could be substantially higher than that of the virgin material, an effect that will be pronounced over multiple shears of the same area, up to a maximum hardness. For example, Lindroos et al. (2015) found that “work hardening led to a 50 % increase in surface hardness compared to the initial bulk hardness”. Also for most tests, multiple scratches were required at large enough loads to reach the maximum hardness in the same groove.

Another limitation of the analysis derived from Figure 2.11 is that irregular particles will cause varying amounts of material cutting and plastic flow. The cutting-plasticity ratio η can be calculated as the ratio between the volume below and above the virgin plane

$$\eta = \frac{V_{\text{below}} - V_{\text{above}}}{V_{\text{below}}} \quad (2.27)$$

As η approaches 1, the wear mechanism is fully cutting, whilst zero denotes a wear mechanism of fully ploughing (Lindroos et al., 2015). In a fully cutting mode, all material plastically deformed from the surface is removed as a chip. In a fully ploughing mode, all material is pushed ahead, underneath and to the sides of the particle. The transition between ploughing and cutting is dependent upon the attack angle of the particle α as a function of the depth of penetration. The deformation mode changes when the attack angle falls below the critical attack angle, $\alpha < \alpha_c$, where lower attack angles — as defined in 2.11 — cause more cutting than ploughing. A sphere for example has an attack angle of 90° and will cause 100 % ploughing, whilst a wedge has an attack angle of 0° and will cause 100 % cutting. α varies for different metals as it has a dependency on the shear strength of the material. It is important to note that when $\alpha < \alpha_c$, it does not mean that every particle causes 100 % cutting deformation, but rather the proportion of plastic deformation by cutting is greater than by ploughing. It is unsurprising also that the particle shape has an affect on the attack angle, with more angular particles tending to have higher angles of attack, which results in a greater proportion of cutting, over ploughing, plastic deformation.

Having given consideration to this abridged review of tribology, it is evident that there is a significant overlap between physical properties governing granular shear behaviour and abrasive wear of materials. As such, any analysis of the behaviour of soil-structure interfaces must consider both halves of the interface in equal measure, as the shearing of a granular body over a surface clearly causes degradation in the form of abrasive wear. Having established this link, a plan can be synthesised for future research that leverages the insights of tribological research. Curiously, little mention is given to material wear in published interface research. Perhaps, with the added understandings from tribological research, one can reimagine conclusions drawn from analysis of soil-structure interfaces in shear, particularly those in the long term.

2.3 Soil-Structure Interfaces

2.3.1 Relevant Terminology

Interface Layer

The interface layer has been established as an area of key importance to SSI behaviour (DeJong et al., 2003; Hu and Pu, 2004; Uesugi et al., 1989). It is a region within the soil body directly adjacent to the structure in question, displayed in Figure 2.12 in the example of a direct interface shear box. Crucially, experimental study has shown this region to have a thickness t as a function of mean particle diameter, where $t = 5 \sim 10 \times d_{50}$. This region is not dissimilar to a shear band that occurs in other shear scenarios, be it triaxial compression, simple shear etc. (Huang et al., 2019). Soil outside of this region is referred to as far-field soil, and has a negligible impact upon interface behaviour (DeJong et al., 2003; Uesugi et al., 1989).

Boundary Condition

The boundary condition, parallel to the interface confining the soil body, of interface testing is defined by the stiffness of the boundary. There are two limit conditions that can be imposed on the interface: of zero stiffness, or constant normal load (CNL); or of infinite stiffness, constant volume (CV). A constant stiffness (CNS) boundary also exists between these two limit states (DeJong and Westgate, 2009; Evgin and Fakharian, 1996). The boundary conditions are

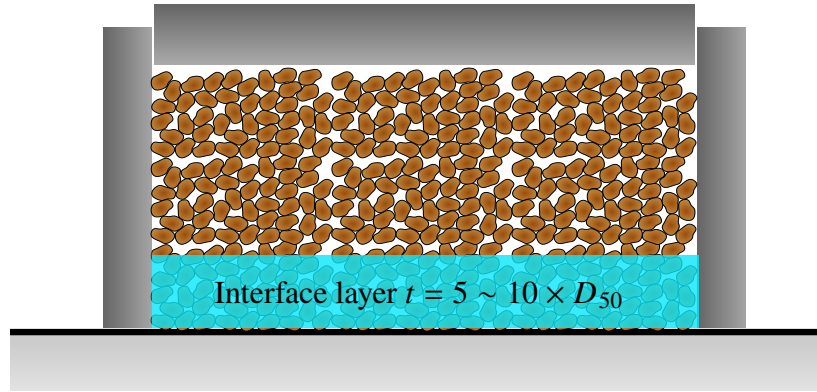


Figure 2.12: Diagram of a direct interface shear box showing the thickness t of the interface layer

visualised by the continuum represented in Figure 2.13. In reality, all interface boundaries have some stiffness K , though in experimental testing it is advantageous to understand behaviour at either ends of this spectrum.

Relative Roughness

Frictional behaviour of the interface must be dependent on both constituents of the interface, the soil and structural interface. The relative roughness R_n has been established to quantify the difference in roughness for different structures, relative to the adjacent soil (Uesugi et al., 1989).

$$R_n = \frac{R_{\max}(L = d_{50})}{d_{50}} \quad (2.28)$$

R_{\max} is taken as the maximum distance between the peak and trough along the a surface profile of length equal to d_{50} . A representation of this relationship is shown in Figure 2.14. Evidently for long interfaces, multiple values of R_n will be found and a generalised relative roughness of the interface can be calculated as the average of these values.

2.3.2 Stress Paths and The Influence of Boundary Condition

Much in the same way as the Cam Clay framework of triaxial compression, the method of application of load to a soil body has an effect on the stress path it responds with (Bolton, 1984). When carrying out experimental testing of interfaces, the boundary condition, which controls the application of normal stress has an impact on the shear response. Evgin and Fakharian (1996) studied the stress

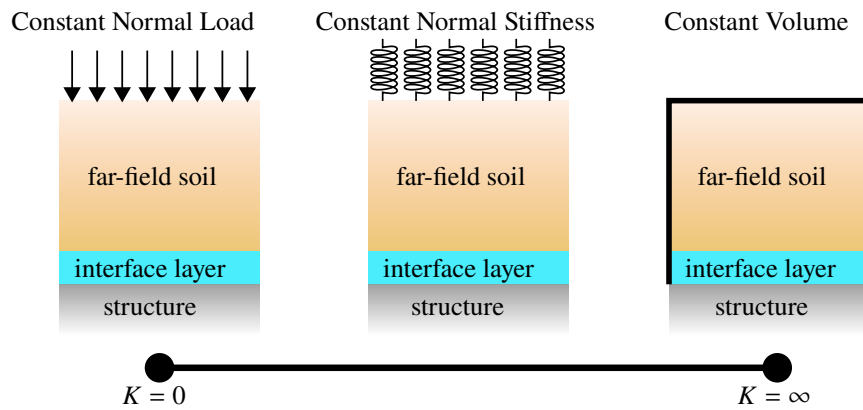


Figure 2.13: Diagram of the three boundary conditions present in interface testing

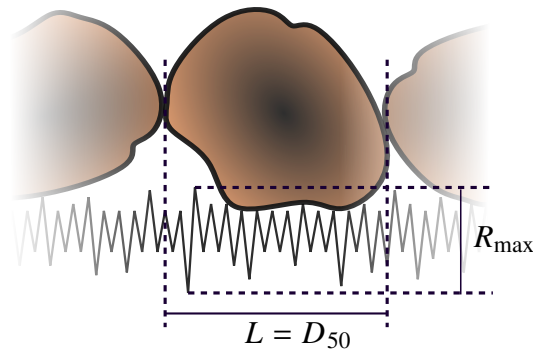


Figure 2.14: Diagram of the relative roughness at a soil-structure interface

path response of a sand-steel interface in both 2D and 3D monotonic simple shear, to each of the three principal boundary conditions. A densely poured medium crushed quartz sand against a rough surfaced steel plate was used to simulate the interface. It should be noted that direct and simple interface shear tests obtain the same peak and residual shear strengths in both monotonic and cyclical shearing up to a cumulative 5 mm. Simple shear brings with it the advantage of measuring shear deformation of the sand, where total tangential displacement is equal to the sum of sliding and shear deformation (Evgin and Fakharian, 1996). For this study, the stress path was considered in stress ratio vs. displacement space, $(\tau_x/\sigma_n) - (u_x)$ for 2D tests, $((\tau_x^2 + \tau_y^2)^{0.5}/\sigma_n) - (u_x^2 + u_y^2)^{0.5}$ for 3D tests. After consideration of the experimental results, which showed a steep rise over the first millimetres of shearing before softening, Evgin and Fakharian (1996) concluded that the magnitude of both the peak and resultant stress ratio is independent of stress path. For six 2D tests of stiffness 0 kPa mm^{-1} to 1200 kPa mm^{-1} , there was

2.3. SOIL-STRUCTURE INTERFACES

a proportionate change in shear stress and normal stress resulting in negligible variation of stress ratio. A similar response was witnessed for the 3D tests carried out, a rise in stiffness has a negligible impact upon monotonic shearing of samples with a constant initial normal stress.

In the same study Evgin and Fakharian (1996) compared the effect of a change in normal stress level for both CNL and CNS tests. Sample results of the variation in stress ratio μ with sliding displacement are shown in Figure 2.15. An increase in initial normal load, for both CNL and CNS tests, suppresses the softening phenomenon after the peak stress ratio, as well as reducing the magnitude of the peak stress ratio. Interestingly, for higher normal stresses, the elastic response of shear stress is shortened as plastic response becomes prominent earlier in the sliding displacement. Regardless of the shear behaviour approaching the peak stress ratio, in both CNL and CNS conditions the post-peak response is identical for varying normal stresses. The residual stress ratio is not affected by changes in normal stress, indicating that this value is perhaps constant for the given interface constituents. Finally, Evgin and Fakharian (1996) concluded that the stress path has a significant influence on the shear stress — tangential displacement behaviour of the interface. For example in CNL tests of increasing normal stress, a peak shear stress emerges that is more pronounced with increases in normal stress, whilst for CNS stress, no such peak emerges.

A similar study into the effects of the boundary condition was carried out by DeJong and Westgate (2009). Tests of a rough interface against loose and dense samples of Ottawa 20 – 30 quartz sand simulated the interface. Notably, some differences between the witnessed behaviour in Evgin and Fakharian (1996) for CNL tests exist. Evgin and Fakharian (1996) assert that the “residual stress ratio is independent of the magnitude of normal stress”. However, data from DeJong and Westgate (2009) shows a marked difference between the tested stresses of 10 kPa, 100 kPa and 1000 kPa in dense samples. Resultant values of stress ratio varied from 0.75 to 1.6. The high stress test showed a shear stress hardening response, consequently causing a hardening of stress ratio, a conclusion that was not drawn by Evgin and Fakharian (1996), although the trend of increasing normal stress suppressing peak behaviour suggested this. Evidently the difference highlights a failing of testing methodology in Evgin and Fakharian (1996) as only constant loads of similar order of magnitude were tested. Although a much rougher surface, $R_n = 0.95$, was used in DeJong and Westgate (2009) to simulate the interface when compared to Evgin and Fakharian (1996), perhaps a change in residual stress

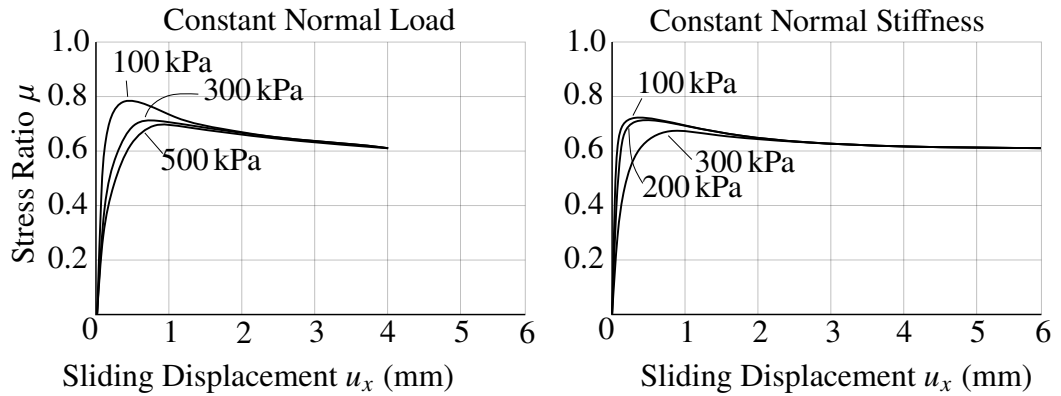


Figure 2.15: 2D simple shear tests results for CNL and CNS tests (reproduced from Evgin and Fakharian (1996))

ratio occurs for much greater normal stress levels.

On the subject of CNS conditions the two studies do corroborate the conclusion of a common ultimate stress ratio. The volumetric response of the samples in both studies involving CNS and CNL tests were in agreement. For greater normal stresses volumetric contraction is increased, whilst understandably, increases in stiffness suppress dilative effects. To ground the knowledge presented here in real world application, consideration can be given as to the conditions needed for various loading conditions. As mentioned previously and shown in Figure 2.13, the stiffness of the boundary condition lies on a continuum. It is unlikely to ever find conditions of no stiffness $K = 0$ in real engineering problems. A stiff system, where volume changes are suppressed $du_x \rightarrow 0$, resembles the radial pile-soil boundary along the depth of the pile (Fioravante, 2002; Foray et al., 1998). A ‘flexible’ system, where a constant dead load is applied and volume changes are not suppressed $du_x \rightarrow \infty$, may occur at a shallow buried pipeline in non-cohesive, dry sand, where the absence of pore pressures does not provide a rebounding effect to volumetric changes in the soil specimen.

2.3.3 Initial State and Relative Density

The density of a soil body has a marked impact upon its response to shearing. Whilst fundamental mechanical soil characteristics such as shape and gradation play a role in the relative density of a sample, the soil stress/strain history also has an impact. In general, loose samples undergo a contraction during shear, with a strain hardening effect; dense samples experience a dilation and strain softening effect, resulting in a higher shear resistance than an equivalent loose sample Saberi

2.3. SOIL-STRUCTURE INTERFACES

et al. (2018). Relative density I_D is defined as

$$I_D = \frac{v_{\max} - v}{v_{\max} - v_{\min}} = \frac{e_{\max} - e}{e_{\max} - e_{\min}} \quad (2.29)$$

DeJong and Westgate (2009) clearly showed from monotonic interface shear for three soil types of varying shape and fracture strength on a sandblasted steel surface, that dense samples, as expected, had a greater mobilisation of shear strength and consequently greater ultimate stress ratio than loose samples. It should be noted that this greater shear strength, identified by DeJong and Westgate (2009) occurs at an ultimate rather than critical state. With continued shearing, one would expect that a common critical state will be reached for both dense and loose samples, as the critical state is independent of initial relative density (voids ratio). Unfortunately reaching a critical state through monotonic direct shear testing is often difficult, due to the lack of disassociation of sliding and soil deformations that is otherwise present in simple shear testing.

It has been established in Section 2.3.2 that increases in the normal load on an interface suppress the dilative response of dense soils. From the literature presented in Section 2.1.2, this finding relating to interfaces is in good agreement with granular mechanics work. An increase in normal load increases the amount of work required for dilative rearrangement which can not be matched by the shearing of the interface, hence, the equivalent dilation of the soil will be lower.

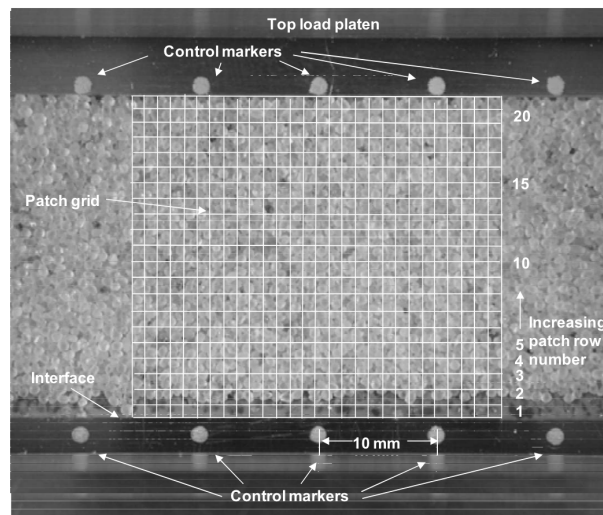


Figure 2.16: Example of PIV imaging and patching from DeJong and Westgate (2009)

Using particle image velocimetry (PIV) analysis DeJong and Westgate (2009) was able to evaluate not just the global volumetric response during shear,

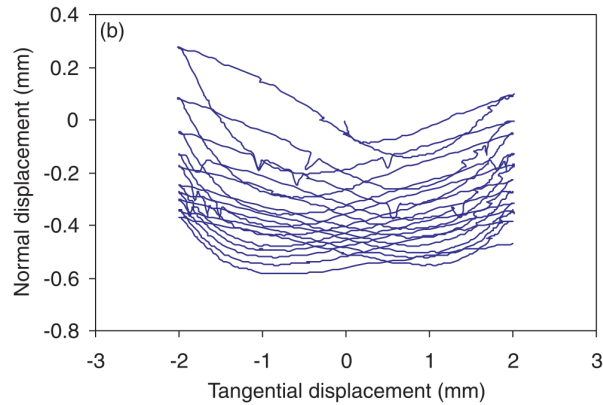
2. LITERATURE REVIEW

but of the local interface layer. PIV analyses have been utilised several times in granular soil-structure interface studies, an example of the samples imaged, including the patch size is displayed in Figure 2.16. Advances in imaging techniques in recent years have improved the fidelity of traditional PIV techniques (White et al., 2003), though ‘patching’ the sample introduces an inherent error in the tracking of individual particles. It was concluded that the dilative reaction of a dense sample sheared under a normal load occurred only within the interface layer. Even for loose soils, DeJong and Westgate (2009) found particles in contact with the interface would dilate as interlocking occurs, as those particles interact with the roughness of the interface. Beyond this, in the far-field soil, volumetric changes occur in the normally expected fashion depending on their relative density, compensating for the dilation of the particles in contact with the structural surface. A similar finding of localization of dilation in shear bands (the region of deformation in soil-soil body shearing) has been found in purely soil tests (Bernard et al., 2002; Gudehus and Nübel, 2004).

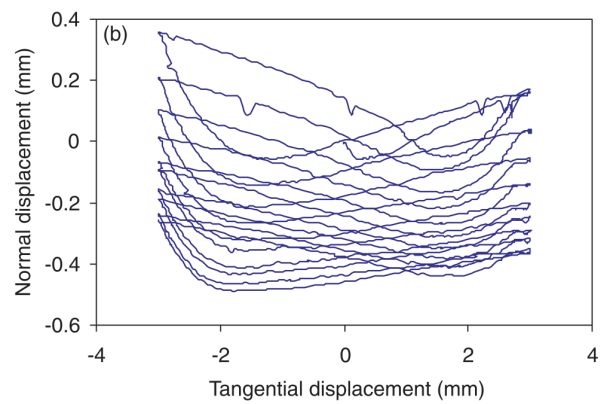
One quirk of soil-structure interface shearing is the cumulative contraction of soils of any relative density. Cumulative contraction occurs over several cycles of shearing on the same sample. In experimentation where the interface is sheared over the same area multiple times, the global soil sample experienced contraction, regardless of the initial density of the sample (DeJong and Westgate, 2009; Dejong et al., 2006; Mortara et al., 2007). Upon initial shearing, it is well known that a dense sample undergoes a slight contraction before steadily dilating, as particles interlock with the interface, be that structural or soil. When the reversal of shear direction occurs, this initial contraction is more pronounced, and the contraction magnitude is greater than the cumulative dilation for the given cycle (Hou, 2008; Oumarou and Evgin, 2005). This behaviour is displayed graphically in Figure 2.17, using results from Oumarou and Evgin (2005) of dense samples sheared through tangential displacements u_x of 4 mm and 6 mm. This conclusion is in excellent agreement with that of Ghafghazi et al. (2014), reviewed in Section 2.1.3. Regardless of the initial state of the sample, energy is expended through reorientation of the samples. Upon shear reversal, a relatively large rearrangement occurs, presumably as particles in the interface layer in contact with the interface itself undergo a complete orientation, allowing for the voids ratio to decrease as energy is expended.

If the conclusions drawn from Ghafghazi et al. (2014) are to be followed fully, it would suggest that after this cumulative contraction, the critical state

2.3. SOIL-STRUCTURE INTERFACES



(a) Cyclic test on dense sand, $\sigma_n = 200$ kPa, $u_x = 4$ mm



(b) Cyclic test on dense sand, $\sigma_n = 200$ kPa, $u_x = 6$ mm

Figure 2.17: Simple interface shear results, from Oumarou and Evgin (2005)

is reached and particle breakage should begin provided the stress state is high enough. However, most studies find after a period of cyclic shearing, that the cumulative contraction ceased as the contractile and dilative rearrangement of each cycle stabilized, indicating a return to a sliding mechanism over deformation of the soil body (Fakharian, 1996; Fakharian and Evgin, 1997). The limitation of these studies is that the maximum cumulative shear displacement reached was only 37.5 mm over 50 cycles. If we are to gain a better understanding of real interface response, we need to simulate behaviour beyond what is to be predicted. In reality, accumulated shear displacement could be at least two orders greater over the life span of an interface (Guo et al., 2014). It is incorrect to assume on a cessation of volumetric strain, that those conditions will continue into the future based upon the form of only a few millimetres of shear, especially when there

is evidence of an emergence of particle crushing upon continued compression. Indeed, the density of the sample, particularly that of the interface, is a function of the amount of breakage (from Section 2.1.3). If the density of the interface layer changes due to breakage, it follows that the shear behaviour could change drastically through repeated shearing.

2.3.4 Roughness and Hardness

Having reviewed the influence of variations in the properties of the soil in an interface's behaviour, it is clear that variations in the structural properties will influence behaviour. To explore the influence of a change in surface roughness DeJong and Westgate (2009) used three different structural interfaces sheared under a CNL boundary. For the smooth condition, a machined smooth steel interface of relative roughness 0.008; for the intermediate condition, a sandblasted steel surface of relative roughness 0.074; for the rough condition, a steel plate milled to a 1 mm depth below surface level, backfilled with an epoxy/sand mixture and filed down to give a relative roughness of 0.98. There is one notable inconsistency with these three surface conditions when evaluating the methodology with respect to the review of tribology in Section 2.2. Both the smooth and intermediate surfaces are metallic, machined to a certain roughness, whereas the rough surface is a mix of polymer and quartz sand which will have greatly different hardness values. From Equations 2.21, 2.25 it is shown that the hardness of the materials in abrasion affect the wear mechanism. In the rough condition, there will have been soft and hard spots across the interface, which could influence the wear of these materials. Fortunately for this study, only monotonic shearing was examined, and so the different rate effects of plastic wear in soft and hard materials should not have caused a great impact.

DeJong and Westgate (2009) concluded on variation of the roughness of the interface that an increase in relative roughness R_n , there was a corresponding increase in shear stress mobilisation and stress ratio, with an exacerbated softening in stress. Rougher surfaces tended to impose much greater dilation on the interface, with loose samples experiencing dilation due to particle interlocking at the interface regardless of their tendency to contract. Very smooth surfaces removed the dilative reaction of dense samples to shearing, whilst densification of loose samples still occurred through contraction of the interface. These conclusions are in good agreement with Hu and Pu (2004); Uesugi et al. (1988, 1989), which showed there

2.3. SOIL-STRUCTURE INTERFACES

existed a critical relative roughness for sand-steel interfaces of 0.1. For $R_n > 0.1$ a peak shear stress emerges and post-peak softening is seen. An explanation is offered in Uesugi et al. (1988, 1989), which showed that the interface coefficient of friction increases linearly with R_n until the interface coefficient of friction is equal to the soil friction coefficient, at which point, increases in roughness have a negligible effect on interface friction.

Cyclic Effects

For interfaces subjected to cyclic shearing both softening and hardening of the stress ratio may occur, depending on the initial roughness and tendency for particle breakage. Mortara et al. (2007) carried out CNL and CNS tests of Gioia Tauro quartz sand of two fractions on steel plates with a relative roughness $R_n = 0.157$ and 0.030. It was concluded that for smooth interfaces the volumetric strains from cycle to cycle, of cumulative contraction comprised of a sudden contraction on shear reversal followed by sustained dilation (see Section 2.3.3), were not as intense as rougher surfaces. This conclusion is one that could have been predicted by those familiar with soil-soil interface direct shear tests. Where the interface coefficient of friction is lower, volumetric changes have lower magnitude. It has been demonstrated that the relative roughness of interfaces is a key in determining the stress behaviour of the interface. Relative roughness, as per Equation 2.28, is dependent upon the mean particle diameter d_{50} and R_{max} . Clearly, as shown by Sections 2.1 and 2.2, these quantities can change after shearing. If the particles in the interface layer undergo breakage, the mean particle diameter will fall and the relative roughness increases. It has been shown that for a higher relative roughness, there is an increase shear stress mobilisation. As Saberi et al. (2018) neatly concludes, “in smooth surfaces, particle breakage increases roughness and leads to an increase in residual shear strength. However, particle breakage does not have a significant impact on stress-displacement behaviour of rough surfaces.”

As explained by Uesugi et al. (1988, 1989), increases in R_n after interface friction has equalled the soil coefficient friction have a negligible effect on interface friction, hence stress response is not effected by particle breakage in already rough interfaces. A similar conclusion can be drawn when considering the plastic deformation of the structural interface. When abrasive wear of the relatively soft interface is caused by a granular material, plastic deformation leads to the value of R_{max} , and consequently R_n , increasing. For already rough interfaces, the increase

2. LITERATURE REVIEW

in R_n has a negligible impact upon the stress response as the limiting friction ratio has become that of the soil. On account of this limiting friction ratio, an interesting relationship can be offered for the resultant coefficient of friction or stress ratio after a number of cycles. If particle breakage and abrasive wear cause a change in relative roughness such that the interface coefficient of friction tends towards the soil friction ratio, the stress ratio over many cycles should reach a unique value, regardless of the initial relative roughness. This conclusion is drawn by Uesugi et al. (1989) from data of 15 cycles of a sand-steel interface of relative roughness between 0.003 to 0.103.

Knowing from Section 2.2 that the hardness of a material influences its response to abrasive wear, the parameter R_{\max} at the end of a period of cyclic shear will be a function of the wear the structural interface has experienced. In an experimental and DEM study into surface roughness and hardness, Frost et al. (2002) concluded that the hardness of the interface was found to influence the stress mobilisation at the interface by experimentation of monotonic direct shear up to 80 mm, with softer materials achieving a larger interface friction angle. This finding is to be expected, softer materials are more susceptible to wear, causing an associated increase in the interface friction angle. Other research has shown the surface hardness to not be a constant value, and that abrasion can change the hardness of the surface, this process (referenced in Section 2.2) is known as work hardening. Lindroos et al. (2015) showed that the local hardness of a region of hardened steel worn by a diamond pin (such that $H_a > 1.2H_s$ from Figure 2.10) increased after multiple cycles, whilst the average coefficient of friction and wear rate decreased for every cycle. In experimentation, a constant normal load was applied through a fixed diamond pin to simulate two-body abrasion. Initially, a quartzite particle was used, though the irregular shape of grains did not provide consistency across tests. After ten cycles, the steel interfaces were scanned using white light interferometry, to create a high resolution map of the surface. Due to plastic flow, the value of R_{\max} greatly increased. As per Equation 2.28 and the relevant explanation in the previous paragraph, it would be expected that a greater amount of stress transfer would occur as roughness has increased, though this is not the case. When diamond tip embeds itself into the surface, one may expect the greater frictional contact area to cause stress transfer, though results displayed a reduction in the coefficient of friction (stress ratio). Work hardening of the area local to the pin/particle was responsible for this reduction. Whilst Frost et al. (2002) predicts a fall in stress ratio for an increase in hardness, that is

assuming roughness does not change, results from Lindroos et al. (2015) seem to conflict this. One potential explanation for this discrepancy is the relationship between single particle interface shear and macroscopic interface shear.

2.4 Summary of Findings and Conclusions

This chapter has reviewed the disparate literature of granular mechanics, tribology and soil-structure interfaces. In doing so, it has been shown that there is a significant overlap between the fields, particularly in the areas of abrasive wear and its potential influence on interface behaviour. The following insights can be drawn from the literature review, presented in order of the preceding sections, highlighting the areas of research that require further investigation:

1. *Numerical simulations such as Discrete Element Modelling are not always sufficient for modelling complex granular behaviour.* Even considering recent improvements, the computational capacity of numerical simulations is limited by the number of particles and accuracy of shape that can be modelled. In any case, element scale testing is still required to validate any numerical model.
2. *A model for characterising 3D angularity is required, at present only 2D angularity has been considered.* If the bulk behaviour of granular systems is able to be modelled using 3D analysis of particle form, there is a need for a similar analysis to determine the micromechanical behaviour governed by local angularity of a particle.
3. *Particle scale experimentation has led to a greater understanding of the mechanics of granular systems.* Particle scale experimentation has yielded numerous insights into interparticle friction and crushing behaviour, which can be used to inform macroscopic models of granular behaviour, or improve the likeness of numerical simulations to reality. It stands to reason that similar analyses at the particle scale can be conducted for soil-structure interface behaviour.
4. *Abrasive wear must occur in soil-structure interfaces.* Tribological theory states that given the difference in hardness of sands and structural materials (as opposed to the sand-sand contacts reviewed in Section 2.1.1, it is clear

2. LITERATURE REVIEW

that abrasion will occur in soil-structure interfaces. The extent of this influence requires investigation.

5. *Abrasive wear is governed by particle shape, based traditionally on a simple 2D attack angle.* There is no method for establishing the relative abrasive influence of complex grain shapes. Traditional tribological analysis is limited to simple constant geometries such as conical tips. If the influence of abrasion on interface behaviour is to be understood, then the influence of shape on abrasion must be considered.
6. *A range of boundary conditions are possible at interfaces.* When considering the behaviour of an interface, the boundary condition it is subjected to can dominate its response. It is therefore important to consider a range of boundary conditions, particularly those that are likely to be encountered in real world applications. One such condition is the constant normal load, which has not been extensively studied.
7. *Interface testing needs to examine long term behaviour.* The cumulative shear displacement of an interface over its lifespan is likely to be much greater than that of existing experimental studies, which have been shown to only consider a maximum of hundreds of cycles. As such, it is necessary to investigate behaviour at shear displacements beyond what is currently available in the literature, to gain a better understanding of the long term behaviour of interfaces, comparable to the design lifespan of those applications.
8. *Abrasive wear must change interface behaviour.* It has been established that the behaviour of an interface is dependent on its relative roughness and load condition. Therefore it follows that abrasive wear of the interface will change its behaviour. Over a number of cycles, these characteristics will change with continued wear. As such, is important to investigate the effect of wear on the interface behaviour.

In summary, if abrasive wear is occurring at the interface between a relatively harder body of sand and softer body of structural steel, then the magnitude of this abrasive wear is influenced by the load application, and duration of loading, in addition to the abrasive characteristics of the sand, namely the particle shape. These insights allow for a plan to be synthesised for a micromechanical investigation into soil-structure interfaces.

Chapter 3

Aims and Objectives

The aims and objectives of this research must attempt to address or test these conclusions, and to provide a new insight into the behaviour of soil-structure interfaces. In light of this, the following aims are proposed with the according objectives:

Aim 1. *Investigate the link between macroscopic interface behaviour and particle scale interface behaviour.*

The interface layer is comprised of many single-particle contacts to a structural interface. Whilst the macroscopic behaviour is complex, investigating the behaviour of a single particle contact may provide a better understanding of the interface behaviour.

Objective 1. Conduct a series of macro scale and particle scale interface shear tests to establish the link between macroscopic interface behaviour and particle scale interface behaviour.

Objective 2. Carry out experiments at a much larger number of cycles than previously conducted to establish a better understanding long term behaviour of the interface.

Aim 2. *Investigate the role of abrasion at soil-structure interfaces.*

It is known that abrasion is a key factor in the wear of a surface, but the effect of abrasion on the behaviour of a soil-structure interface is not well understood at present.

Objective 3. Examine and characterise the quantity of abrasion on a structural interface after a series of interface shear tests.

3. AIMS AND OBJECTIVES

Objective 4. Develop a method to establish if any abrasion takes place on sand grains in the interface layer.

Aim 3. *Analyse the role of particle shape in particle-interface shear.* The shape of an abrasive particle is a key factor in determining the wear rate of a surface. It is impossible to analyse the effect of this in particle-interface shear without a method to accurately capture the contact geometry.

Objective 5. Develop a method to accurately capture the 3D shape of a particle.

Objective 6. Develop a method to analyse the 3D contact geometry of a particle against a surface in particle-interface shear.

With these aims and objectives used as a framework, the following chapters will detail the research conducted to address them.

Part II

Investigation and Analysis

Outline

The following chapters are largely reproduced from three separate first-author entry journal articles. Where necessary, alterations have been made to suit the format of this thesis. Firstly, to avoid the duplication of figures, figures that may reoccur from chapter to chapter will reference the first appearance, for example in the Literature Review. Secondly, an additional section of narrative has been added to the end of each chapter, to link back to the aims and objectives of the thesis.

Chapter 4

The role of abrasion in cyclically sheared soil-structure interfaces

4.1 Notes

This chapter is reproduced from the Géotechnique entry Pettey and Heron (2023*b*). Where necessary, changes have been made to reflect the continuous narrative required for a thesis, mainly to the introduction which draws on the established literature review. The original paper is available in the University of Nottingham library and online at <https://doi.org/10.1680/jgeot.22.00326>.

4.2 Introduction

As established in Chapter 2, the long-term behaviour of soil-structure interfaces has been investigated in only very limited depth, which is not sufficient considering the long life-spans of these systems. For example, thermal expansion and contraction of a buried pipeline will cause thousands of cyclical shear displacements over its design lifespan (White et al., 2012). Equally, for the case of offshore monopiles used to support wind turbines, there will be the superposition of the low frequency, high amplitude, tidal cyclic loading with the higher frequency, lower amplitude, wind induced cyclic loading (LeBlanc et al., 2010). Combined, there will be several thousand loading cycles imposed on the monopile over its lifetime and hence extensive cyclic loading of the soil-structure interface. It is therefore necessary to understand the behaviour of soil-structure interaction at high numbers of cyclic shears. It should be noted that due to the continual degradation of the

structural interface and granular soil during shearing, a single ‘steady-state’ is not expected to be achieved and hence ‘long-term’ in the context of this work refers to shearing over a significant number of shear cycles and does not refer to a traditional ‘ultimate state’. In any case, research into the cyclical behaviour of soil-structure interaction has yet to consider the behaviour beyond tens of shear cycles. The number of shear cycles to be considered by this study is far greater than that previously considered by prominent published research (DeJong and Westgate, 2009; Evgin and Fakharian, 1996; Ho et al., 2011; Mortara et al., 2007). It is suspected that due to the effect of abrasion, interface behaviour will change significantly over the course of thousands of shear cycles. By examining the interface over a larger number of cycles, the role abrasion plays in the frictional interface shear response can be examined (Lindroos et al., 2015).

The concept of the ‘interface layer’ is well established in literature (see Section 2.3.1). It is defined as the region of soil adjacent to the structural interface in the range of thickness $5 \cdot d_{50}$ to $10 \cdot d_{50}$, where d_{50} is median particle diameter (Hu and Pu, 2004; Uesugi et al., 1989). Existing literature can broadly be divided into two categories — those that seek to understand the behaviour of the interface layer, and those that attempt to capture the macroscopic behaviour witnessed in experimentation through parametric modelling to create a constitutive framework. Notable examples of the former are that of DeJong et al. (2003); DeJong and Westgate (2009); Evgin and Fakharian (1996); Hu and Pu (2004); Uesugi et al. (1989). Examples of the latter are that of Liu et al. (2006, 2014); Mortara et al. (2010); Saberi et al. (2019); Zhang and Zhang (2009). All of the examples presented, from either category, have the same limitation; the scale of experimentation does not capture the long term effects that an ever increasing number of interfaces will be subjected to over the duration of their design life spans (previous studies have finished prior to 100 cycles whereas this study will continue in excess of 1500 cycles). Furthermore, there is a notable lack of studies that focus on the micro-mechanics that inform the global response of the soil-structure interface, at large cumulative displacements. This approach, albeit for a different application, formed the motivation in McDowell and Bolton (1998); McDowell and Daniell (2001) and subsequently McDowell and de Bono (2013), explaining complex geotechnical behaviour with a fundamental micro-mechanical based approach. A similar fundamental approach is needed for soil-structure interface — only then will a proper understanding of global soil-structure-interaction behaviour be developed for cases involving a large number of cycles.

4.2. INTRODUCTION

Although discrete element method (DEM) analyses have proven to be immensely useful in uncovering the fundamental physical interactions that govern the behaviour of granular media, the techniques currently utilised suffer from two main hindrances. Firstly, modelling complex geometries in DEM is notoriously computationally intensive (Kawamoto, Andò, Viggiani and Andrade, 2018; Lim et al., 2016; Michael et al., 2015; Vlahinić et al., 2014). Secondly, even if creating complex geometries was trivial, there is not a standard method to simulate abrasive wear by those non-uniform geometries. To-that-end, particle scale element laboratory testing can be used to provide a detailed insight into the physical interaction. Particle scale experimentation of granular media has been used to great effect by Cavarretta et al. (2010, 2016); He et al. (2019); Nardelli and Coop (2019); Senetakis et al. (2013); Todisco et al. (2017). These studies use mathematical led analyses to quantify the role of particle shape in failure of granular media and inter-particle friction, in addition to the role of granular material properties on shear response. A similar approach of particle-scale testing was adopted for this study as it was hypothesised that such methods will prove just as insightful when considering the interaction between particles and structural interfaces. To achieve this, the objectives of this chapter are Objectives 1 and 2 as defined in Chapter 3.

The methodology to gain insight into soil-*structure* interaction cannot be exclusively led by geotechnics; an acute understanding of the role that material science plays in this relationship must be gained. As such, where it exists, literature regarding particulate wear of a structural surface will be considered to provide novel insights from a geotechnical perspective.

In this study, experimentation at the granular scale is carried out, along with validation against macroscopic (involving a soil body, not just a single grain) experimentation to ensure consistency of response. Analysis of both sets of data is then undertaken, to build an understanding of how abrasive wear changes interface shear behaviour over a large number of shear cycles.

Given the above, this chapter seeks to target the first two Aims as defined in Chapter 3: to investigate the link between macroscopic interface behaviour and particle scale interface behaviour, and to investigate the role of abrasion at soil-structure interfaces.

4.3 Experimental Framework

4.3.1 Testing Apparatus

Two bespoke interface testing apparatuses within the Nottingham Centre for Geomechanics were used for the experimental work presented in this chapter. One was designed to shear a single grain of sand against a structural interface while monitoring the load-displacement behaviour. The second apparatus, similar to a standard geotechnical direct shear machine, sheared a body of grains against a structural interface.

For the testing at single grain scale, a modified one-directional simple shear apparatus was used for the direct shearing of a single particle under a constant normal load. A schematic of the apparatus, and the coordinate system used is displayed in Figure 4.1. To capture the forces in the horizontal X (shear) and vertical Z (normal) directions, F_X and F_Z , low capacity load cells were utilised; 10 N for both normal force and shear force, each with a 0.02 % sensitivity. Horizontal displacement, ΔX , is controlled by a stepper motor and lead screw, through a control loop using the input of a linear variable differential transformer (LVDT - a displacement transducer). The LVDT has a stroke of 80 mm with a sensitivity of 0.01 %. Dead load to the particle is applied by a steel rod through a flanged bearing in line with the 10 N load cell. The rod, which has a mass of 560 g, has weights added to vary normal load. For simplification of the analysis, rotation of the particle is prevented in every plane by an adhesive (ethyl cyanoacrylate), to fix the orientation of the particle contact point with respect to the structural interface plate. Microscopy analysis of the particle during shearing shows that under the applied loads, no detectable net movement occurred between the particle and the connection to the 10 N load cell. Different adhesives were considered, with the most promise shown by a two-part epoxy resin, however this was found to be impractical due to the long curing time and viscous nature of the adhesive. When placing the grain in the epoxy, it was challenging to ensure the particle was fully seated in the adhesive — i.e. in contact with the underlying bolt head — without the particle tip becoming inadvertently covered in epoxy. This was not an issue with the cyanoacrylate adhesive, which is a low viscosity liquid that cures in seconds.

To corroborate the findings from the single particle direct shear tests, testing was carried out on a macroscopic direct shear apparatus, a schematic of the

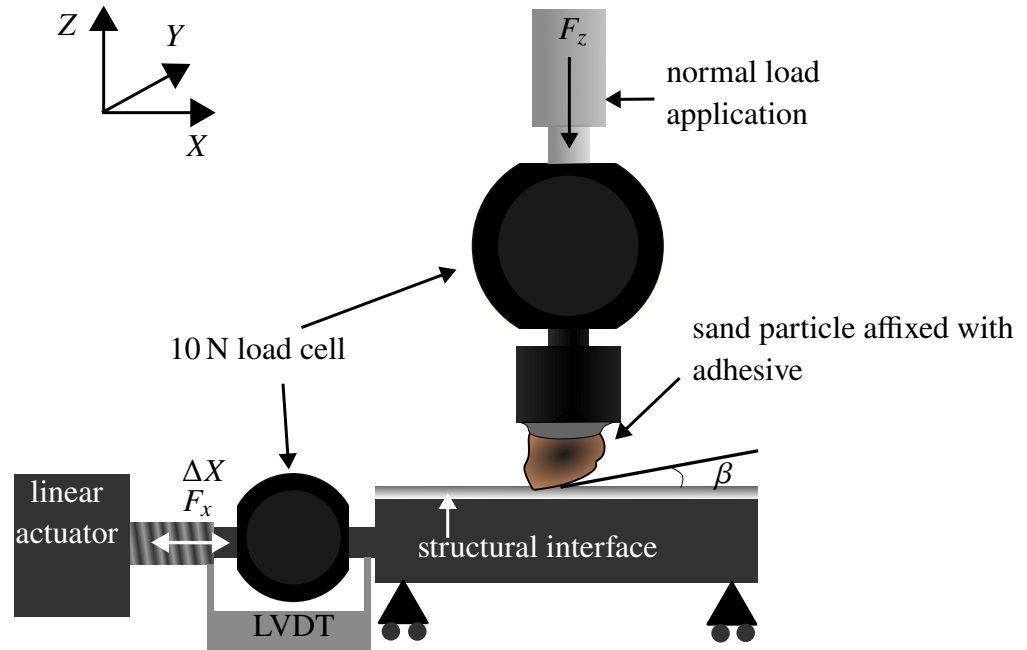


Figure 4.1: Schematic of the single particle direct shear interface

key components is presented in Figure 4.2. The development and initial use of the macroscopic direct shear apparatus has been presented in Hashemi and Heron (2017), with a later study presented in Pettey and Heron (2020) which can be found in Appendix A. Since these studies, changes have been made to the vertical load application. A pneumatic actuator and low latency controller are used to control the vertical load applied to the sample, allowing a range of normal stiffnesses to be used, including that of zero stiffness, i.e. constant normal stress/load. Furthermore, a perspex sided soil container has been utilised in this study to allow for constant imaging of the sample during shearing.

Whilst both testing apparatuses simulate the soil-structure interface, there is one key difference in the nature of the interface regarding the abrasive behaviour in each platform. In single particle shearing the grain (abrasive) cannot rotate as it is confined by the adhesive. This type of abrasion is known as two-body abrasion. Whereas, for the macroscopic direct shear tests abrasive grains are free to rotate — this is three-body abrasion. Three-body abrasion results in a less aggressive wear mode than two-body abrasion (Gates, 1998; Hutchings and Shipway, 2017).

For consistency across both testing platforms, the same granular media is used — Fraction A Leighton Buzzard Sand (LBS), a rounded quartzite sand that has a well reported grain distribution and shape (Senetakis et al., 2013). A d_{50} value of 1.5 mm was calculated for this fraction from sieve analysis. For the

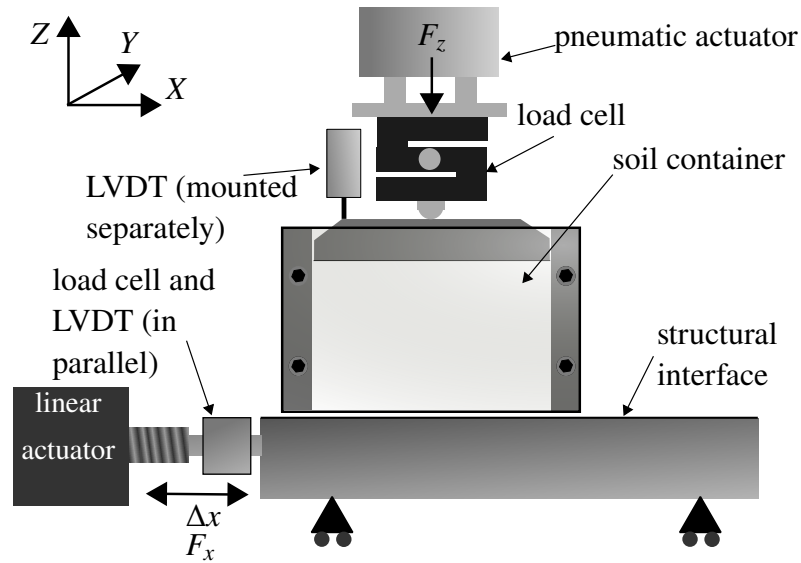


Figure 4.2: Schematic of the macro direct shear apparatus

purposes of ease of comparison, identical 3 mm thickness 304 grade stainless steel plate was used in both testing platforms. In addition, mild steel was also tested as a structural interface in single-particle interface shear tests to better understand the impact of different structural interface materials. It was hoped that using a ferrous material would allow for the separation of metal and sand fines at the end of testing, although this did not prove successful. Crucially, as will be later discussed, the stainless and mild steel interfaces have similar relative hardness values and initial roughness in comparison to the quartz sand and hence, in terms of wear, behave similarly.

4.3.2 Test Data

In this study, controller data in the form of horizontal and vertical load readings, and displacement data are presented. High resolution imaging of the single particle and macroscopic samples is carried out using Teledyne DALSA Genie Nano camera units, providing a means to physically understand the shearing behaviour and to provide context to the controller data. For the macroscopic testing, this imaging was achieved by having a clear perspex sidewall to the soil container, allowing a cross-section of the interface layer to be directly observed. In addition, to quantify the degradation of the structural interface, white light interferometry (a precise surface mapping method) was carried out on a range of single particle and macroscopic interface plates. As such, accurate surface profiles with a lateral spatial sampling of $1.9 \mu\text{m}$ and a vertical resolution better

4.3. EXPERIMENTAL FRAMEWORK

than 0.15 nm are able to be examined post test. Interferometry was also used to calculate the initial roughness of the stainless steel interface plates. It is well established in literature (DeJong and Westgate, 2009; Fakharian and Evgin, 1997; Hu and Pu, 2003; Uesugi et al., 1989) that a key factor in the response of interfaces to shearing is the relative roughness of the interface. Uesugi et al. (1989) defines the relative roughness as:

$$R_n = \frac{R_{\max}(L = d_{50})}{d_{50}} \quad (4.1)$$

R_{\max} is taken as the maximum vertical distance between the peak and trough along the surface profile of length, L , equal to d_{50} . The stainless steel plate is a comparatively smooth surface with an initial roughness of <300 nm. For the Fraction A-stainless steel interface used in this study, initial R_n is approximately 1.5×10^{-4} , which is three orders of magnitude lower than the initial value stated in Uesugi et al. (1989).

4.3.3 Test Plan

Eight macroscopic direct shear tests were carried out with similar test parameters to link the single-particle response to the macro scale. Constant Normal Load (CNL) tests — where $\sigma_n = 100$ kPa — have predominantly been carried out, whilst two tests at a lower constant load of 50 kPa are used to evaluate the impact of normal stress on the interface shear behaviour and to act as a cross-check with other studies (Saber et al., 2018). To investigate the role of particle shape, two CNL tests were carried out using a soil body made up of 5 mm spherical glass beads. Glass beads were used as they are of the same order of hardness as the silica material of Fraction A quartz sand, which is multiple times harder than the stainless steel interface. Furthermore, two tests with a 50 kPa initial normal stress and Constant Normal Stiffness (CNS) boundary condition of $K = 1000$ kPa mm⁻¹ were carried out, for comparison against other studies of macroscopic direct interface shear where CNS conditions have been investigated more often. The test plan is shown in Table 4.1.

For the purposes of this study, all macroscopic direct shear samples were subject to *stabilization cycling* prior to shearing. Dry pluviation (dropping sand at a constant flow rate from a constant height, in this case to achieve a relative density of 85%) is a standard method of sample preparation in geotechnical testing. Centrifuge modellers have found that when sand is dry pluviated, unstable particle

Table 4.1: Test plan for macroscopic direct shear

Interface Material	Soil Body	Initial Normal Stress, σ_{n0} (kPa)	Normal Stiffness (kPa mm ⁻¹)	Cycle Amplitude (mm)	Number of Cycles	Number of Tests
Stainless Steel	Fraction A	50	1000 (CNS)	2	12	2
		50	0 (CNL)	10	1500	2
	Glass Beads	100	0 (CNL)	10	1500	4
		100	0 (CNL)	10	1500	2

4.3. EXPERIMENTAL FRAMEWORK

contacts can form when the sample is prepared and subsequently collapse when the model soil is subjected to an external shearing action during spin up with a radial G-field, resulting in inconsistent experimental results at the small strain level (Stringer et al., 2020). This idea serves as inspiration for the stabilization cycling used in this study, whereby the sample is further densified after initial pouring by cyclically increasing and reducing the normal load (to the test load) — this ensures the grains within the samples adopt a stable configuration (stable particle-particle contacts) and, that shear stresses generated at the vertical boundary wall during the vertical loading process are minimised. As a result, shear behaviour in this study shows a greater level of consistency compared to that previously witnessed utilising the apparatus for a series of macroscopic direct interface shear tests (see Appendix A).

A series of 26 single-particle tests were carried out for this study. The test plan is shown in Table 4.2. All single-particle tests were conducted with a cycle amplitude of 10 mm (i.e. with a total displacement per cycle of 20 mm). Most tests were stopped at approximately 2000 cycles. The mass applied to the particle, above the self-weight of the apparatus, was varied between tests, with repeated testing carried out for mild steel and stainless steel interfaces. In addition, to provide a reference when considering particle shape effects, a spherical glass bead was tested with 500 g applied mass. It should be noted that it was not intended, and it is not practically possible, to replicate perfectly the stress conditions a particle within the macroscopic direct interface test would experience. Instead, nominal loads were used which provided good signal-noise ratio readings on the load cells and which were not so high as to crush the particles in compression. In the single particle case, variation in the particle-interface contact area, defined by the shape of the individual grain, is also found to be variable over prolonged periods of shear as the particle ploughs a trough into the planar interface. Hence, normal pressure applied to the structural interface by the particle is not only variable between particle shapes but also across each grain's test, so a different approach is required for analysis. As will be discussed later in this chapter, there is a potential connection between the stress ratio and the scale of abrasion (total volume removed per unit shear distance). It is not possible, during the tests, to directly measure the scale of abrasion. As such, when presenting the variation in stress ratio during a test, a proxy for abrasion needs to be used. Cumulative energy takes account of the horizontal shear load and the shear displacement — both of which are contributing factors to the scale of abrasion (Hutchings and Shipway, 2017). As

such, cumulative energy will be used as a proxy for the scale of abrasion when presenting the variation in stress ratio for the single particle tests, such as in Figure 4.5. Indeed, it was found that by plotting the results against cumulative energy, instead of cycle number, a higher degree of consistency between tests was observed. This is possible for the single particles as the specific energy per particle is known — this is not the case in the macroscopic testing.

The cumulative energy, E , is calculated as:

$$E = \int_0^x |F_x| dx \quad (4.2)$$

where, x = shear displacement
 F_x = shear load per displacement

Table 4.2: Test plan for single-particle direct shear

Particle	Interface Material	Applied Mass (g)	Quantity
Fraction A	Stainless Steel	750	1
		500	6
		250	3
		100	1
		75	1
	Mild Steel	500	8
		250	5
Glass Bead	Stainless Steel	500	1

4.4 Apparatus Benchmarking

Previous studies into the cyclical behaviour of interfaces have generally considered CNS conditions. Saberi et al. (2018) summarised that differences exist in shear response for CNS tests when compared to CNL or constant volume tests. DeJong et al. (2003) and Mortara et al. (2007) both identified a trend that occurred during CNS testing over a maximum 45 cycles. This trend was a clear reduction in shear stress during cycling. The initial contraction of a granular sample under shearing is understood to cause a reduction in normal stress, when subjected to

CNS conditions, and consequently a fall in the shear stress transferred to the interface occurs. Such a response is to be expected as a result of the constant stiffness boundary condition.

Constant normal stiffness boundaries are common at soil-structure interfaces, however there are a significant number of situations in which CNL conditions are relevant, such as surface or near-surface pipelines. The motivation of this study is to investigate the behaviour of interfaces under cyclic loading when subjected to a CNL boundary condition.

Prior to considering the CNL conditions, as there is no standard for interface testing equipment and hence researchers have tended to develop their own in-house apparatus, it is necessary to benchmark results from the apparatus used in this study to previous studies. If similar results are obtained by considering testing parameters similar to those used by Mortara et al. (2007), one can have confidence in any results presented under CNL conditions and at a much greater number of cycles.

In the case of Mortara et al. (2007), a rough interface of $R_n \approx 0.1$ is used in conjunction with a CNS boundary condition with a vertical stiffness, $K = 1000 \text{ kPa mm}^{-1}$. Identical stress conditions were used in two tests conducted with the macroscopic direct interface shear apparatus, presented earlier, to obtain the results shown in Figure 4.3. Efforts were made to replicate the relative roughness by sanding a stainless steel interface. For comparison, the results from the similar experimental work of Mortara et al. (2007) are also displayed on Figure 4.3. As per Mortara et al. (2007), the degree of degradation is characterised by the degradation factor, which is the ratio between shear stress of the n -th cycle and the first cycle, τ_n/τ_1 . As shown, there is a very similar response to the previously published study, showing the shear stress degradation over the first 12 cycles ($\pm 2\text{mm}$ shearing). This consistency in results provides confidence in the experimental apparatus and approach used in this study.

4.5 Testing Objectives

In an earlier investigation (see Appendix A), it was shown how after a certain level of shearing under a CNL boundary (at cycle numbers which had not been examined by previous studies), an increase in stress ratio occurs — referred herein as a ‘stress ratio elevation’. In this context, a stress ratio elevation is defined as a

4. ABRASION IN CYCLICALLY SHEARED INTERFACES

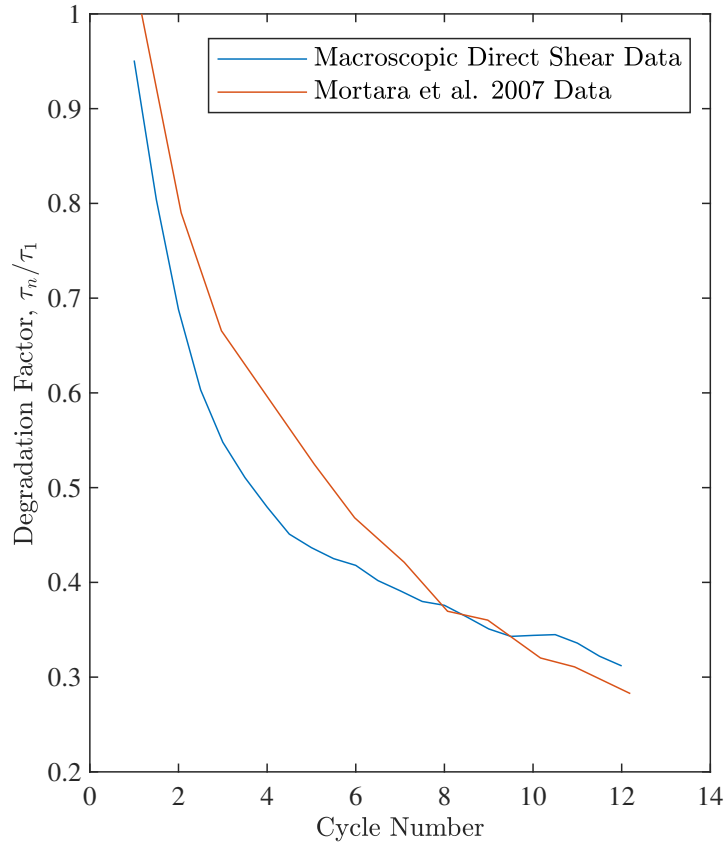


Figure 4.3: Comparison of shear stress degradation response in constant normal stiffness shearing of macroscopic direct shear tests against response reproduced from Mortara et al. (2007)

greater than doubling of initial stress ratio over 100 cycles. An example of this behaviour can be seen in Figure 4.4.

This study seeks to formalise and begin to explain the previously unseen mechanism change by investigating the simplified case of a single particle shearing against an interface. According to theory, there should be commonality between the two sets of results (macroscopic and single particle interface tests) as the magnitude of shearing and interface properties are similar. Comparison of the two data sets, in combination with contextual imaging data and accurate surface profiling, will allow links to be made between changes in the granular and structural bodies. As such, understanding of the underlying causes of the increase in stress ratio can be developed.

4.6 Results

4.6.1 Overview of Results

To aid understanding of the observed change of friction ratio — identified first in Pettey and Heron (2020) (Appendix A) — results from both macroscopic direct shear and single-particle testing are initially presented in Figures 4.4 and 4.5 respectively. For both single-particle and macroscopic direct shear tests, the stress ratio per cycle, μ , has been calculated as the ratio of average shear load to average normal load during each cycle. The stress ratio is synonymous to load ratio or friction ratio as the area over which the vertical and horizontal forces act are equal — in this thesis the term stress ratio will be used.

Figure 4.4 displays the results from four identical macroscopic tests of a stainless steel — Fraction A interface subjected to a constant normal pressure of 100 kPa. Notable is the increase in fines content in the interface layer with increasing cycle number, shown in the inset images of Figure 4.4, which display the cross-sectional view of the soil sample imaged during the test, at selected cycle numbers. In these results two key phases are identified: the elevation phase, which occurs over the first 100 shears; and a subsequent degradation phase where there is a consistent fall in shear stress and hence stress ratio over the remainder of the test (several hundred cycles). Figure 4.5 displays the stress ratio results of all single-particle tests on a stainless steel-Fraction A interface against the cumulative energy of shear (Equation 4.2). Plots of mild steel interfaces will be displayed subsequently. Examining Figure 4.5, there is clearly significant variability between the results for different particles compared to the consistency seen in the macro results (Figure 4.4), even when considering tests of the same applied mass. This is due to the averaging effect in macro tests with hundreds of particles contributing to the overall shear resistance. Whereas variability in the particle shape will have a significant impact on the results obtained from the single-particle testing.

Note that a degradation phase is not seen to occur in the single-particle testing. Although the degradation phase is not the focus of this study, it is informative to explain why it does not occur in the single-particle testing. In the macroscopic tests there is a build-up of crushed material/worn interface material at the interface. When this build-up becomes significant the interface transitions to simply shearing the crushed material over itself (like a fine soil-soil interface)

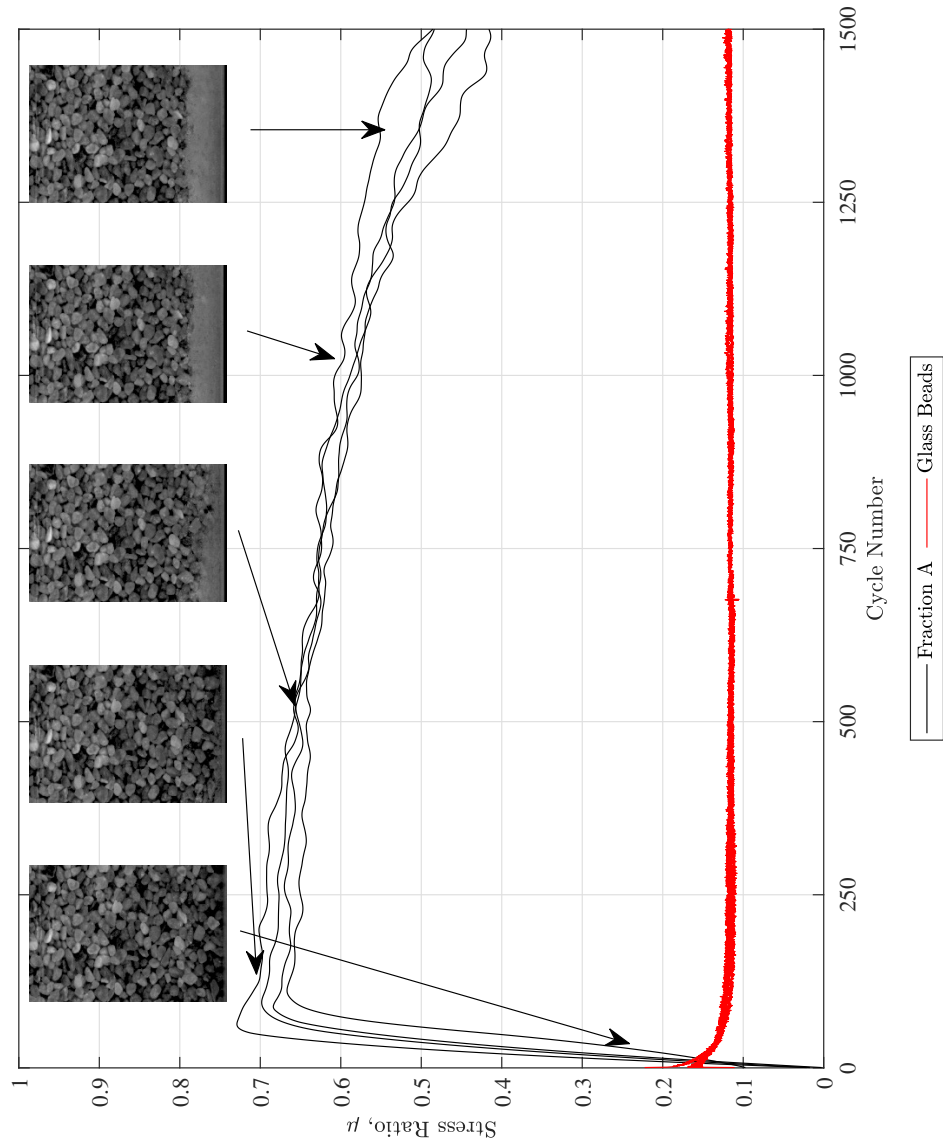


Figure 4.4: Macroscopic direct shear stress ratio vs cycle number for tests where $\sigma_n = 100$ kPa with associated cycle image data

4.6. RESULTS

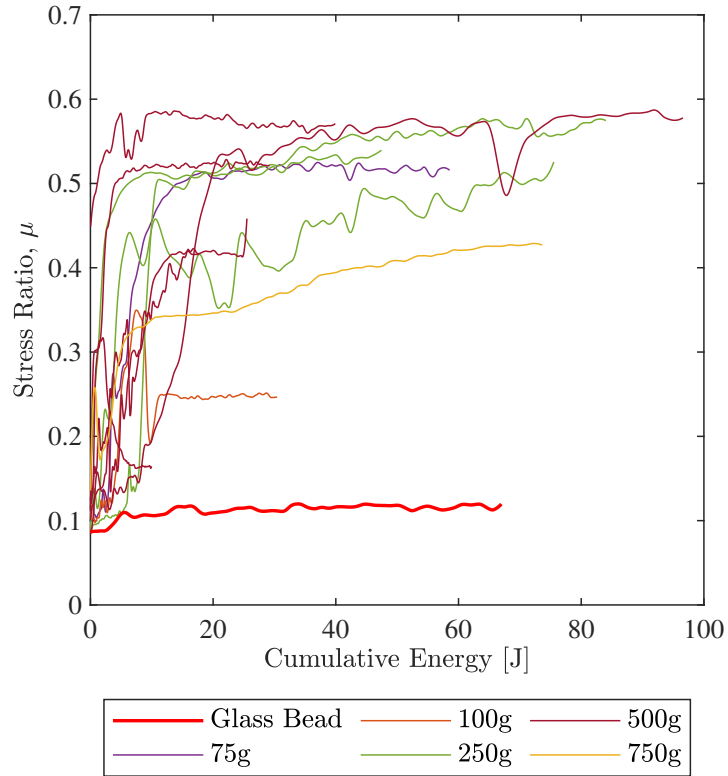


Figure 4.5: Single-particle shear stress ratio vs cumulative energy for Stainless Steel tests with Fraction A and glass bead particles for assorted normal weights

instead of shearing particles against the interface material directly. This leads to a reduced resistance to shear and hence a degradation in the friction ratio. In the single particle tests this does not occur and the constrained single particle being sheared continues to abrade the interface.

This significant stress ratio increase has not been witnessed in other studies as the testing parameters used in this study have not previously been adopted by researchers, most notably confinement condition and relative density. Crucially, an elevation has not been witnessed by any study that investigated interface shear under a CNS confinement condition. Normal load applied to the interface is crucial to abrasive wear. During a CNL test, there is no reduction in applied load despite of volumetric contraction (due to rearrangement and crushing), and hence continual abrasive wear at the interface can be generated. It is this continued abrasive wear which ultimately results in a vast change in shear resistance at the interface. In CNS tests, this cannot occur due to continually reducing vertical load arising from the contraction (rearrangement and crushing) that limit the stress

transferred to the interface.

The following sections will examine single-particle and macroscopic test results independently before discussing their similarities and further discussing the cause of the steep rise in interface stress ratio, μ .

4.6.2 Macroscopic Testing

Each of the macroscopic tests saw a rapid increase in stress ratio from the initial value. The low initial value, which is a function of relative roughness, is the basis of current geotechnical interface modelling and design.

With a low initial roughness, the stress ratio adopts a low value as particles slide over the surface. A change in shear behaviour begins immediately, as indicated by the elevation of μ from the first shear, continuing to a peak stress ratio of 0.7 for tests where $\sigma_n = 100$ kPa, by cycle 100. This elevation in stress ratio must therefore be a result of a change in shear mechanism at the interface from an initial sliding shear where minimal abrasive wear is occurring.

The increase in stress ratio causes an increase in stress concentrations in the soil interface layer, which manifests in a large rate of volumetric contraction. The contraction is dominated by crushing of grains in the interface layer, as supported by image data (Figure 4.4), which corroborates a study conducted on an interface ring shear device by Ho et al. (2011).

Figure 4.6 shows the change in vertical displacement, of the top of the sample, for each test where $\sigma_n = 100$ kPa, against the cycle number. For clarity, the average stress ratio response of these samples has been added on the secondary y-axis. It is evident that the rate of contraction begins to fall consistently with further shearing. Similar to the stress response, there is a good level of consistency in the contractile vertical displacement response, although divergence occurs towards the end of testing, which is thought to be a result of material loss from between the model container and the interface. A reduction in rate of contraction occurs whilst the stress ratio at the interface falls, supporting the argument that the crushing of grains is dependent on the overall stress in the interface layer (not just the vertical stress). It would not have been possible to distinguish where the crushing occurs or crushed grains collect without the context provided by the images acquired during the testing. In an improvement over Ho et al. (2011), images of the soil body during each shear (two per cycle) were collected over the duration of testing, as opposed to solely during dismantling the test after its

4.6. RESULTS

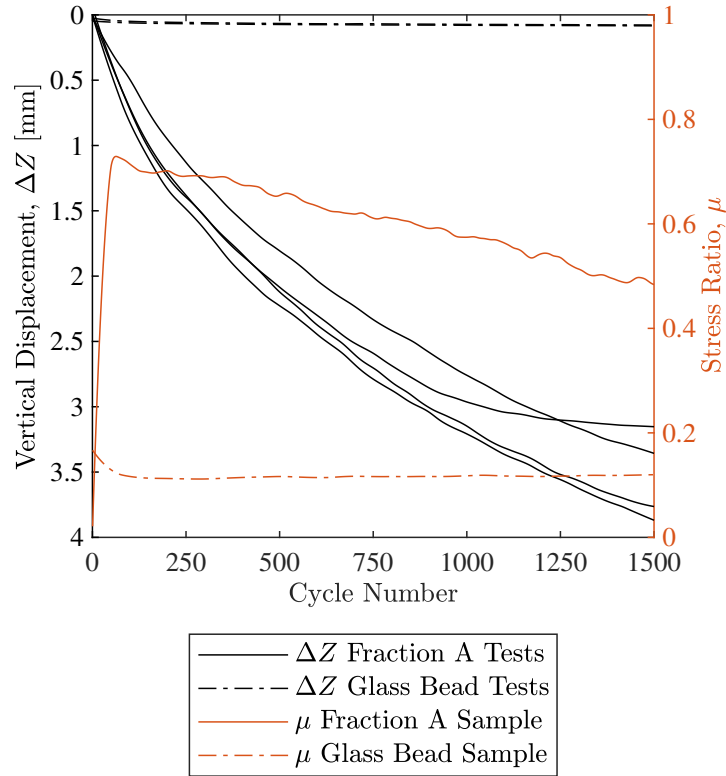


Figure 4.6: Plot of vertical displacement and stress ratio against number of shears for macroscopic direct shear tests where $\sigma_n = 100$ kPa

conclusion. Pettey and Heron (2020) (Appendix A) showed that crushing occurs only in the interface layer independent of the orientation angle of the interface. It was found that, irrespective of the relative direction of gravity to the interface (acting towards or away from said interface), fine material would always build up in the interface layer, with an insignificant amount falling away from the interface in the inverted case, meaning the fines are indeed generated directly in the interface layer. This was observed by conducting the same macroscopic direct interface shear tests with the soil body inverted, i.e. with the entire apparatus rotated 180° about the horizontal axis. This supports the assertion that interface behaviour is ‘not affected by far-field soil’ (Dejong et al., 2006; Hu and Pu, 2004; Uesugi et al., 1989). Figure 4.7 shows images of the sample captured pre- and post- cyclic shearing. The notable deposit of fines due to crushing in the interface layer also accounts for the observed contraction of the sample during shearing. Ho et al. (2011) observed after their ring shear testing, this fine layer “was clearly differentiated from the parent soil by its light grey or greyish-brown colour”,

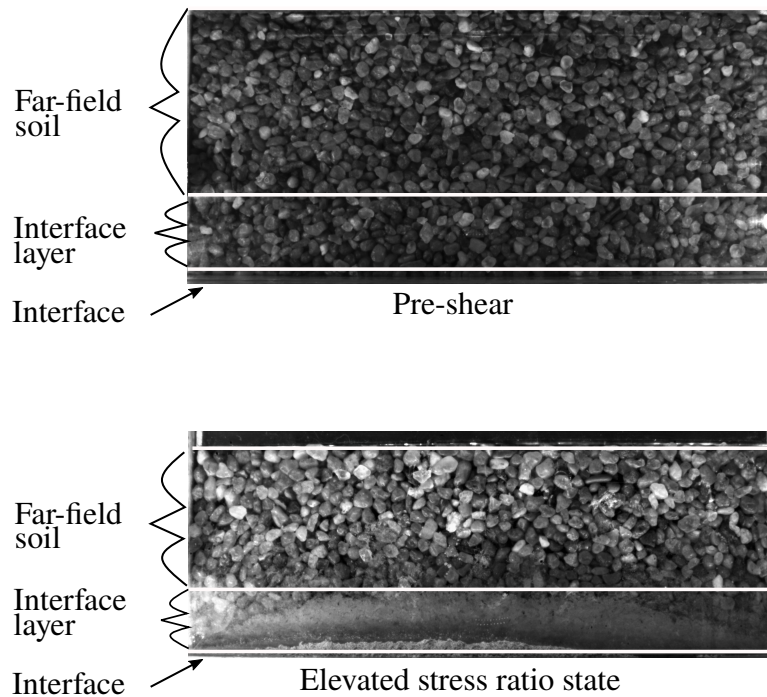


Figure 4.7: Images captured of soil body pre- and post- cyclic shearing during macroscopic direct interface shear test

which was also found during the cyclic macroscopic direct interface shear tests presented in this study. More traditional direct shear analysis of density and voids ratio are not appropriate here, as the soil body becomes stratified by crushing and furthermore, the far-field soil does not contribute to the interface behaviour. Therefore, analysis of the global soil body would disguise notable changes in the interface layer, while it is not possible to quantify the changes in the soil at the interface in real-time during the test. Using the images captured during testing, it would be possible to quantify the change in voids ratio from the beginning of shearing, however due to the stratification of the soil body, this was judged to be a less important measure of change during the test.

Whilst the crushing of the soil interface layer is symptomatic of an increased stress ratio over the original sliding value — as evidenced by Figure 4.4 where fines accumulate post stress ratio elevation — it does not explain the cause or source of the initial increase. The initially smooth structural interface itself is damaged by the shearing of the soil sample. White-light interferometry of the structural interface plates after testing shows a significant increase in surface roughness of the interface, as the surface is abraded by the granular media. A

4.6. RESULTS

profile of the plates after testing is shown in Figure 4.8. To aid visualisation of the wear suffered by the interface over thousands of shear cycles, a pre-test structural interface profile is shown on the same axes. The scale of abrasion is highlighted by Figure 4.8, showing an increase in roughness of one order of magnitude in most areas. Recalling from earlier, the initial roughness of the stainless steel interface was $0.3\ \mu\text{m}$, hence shearing has an extremely pronounced effect on the relative roughness of the interface, with R_{max} values now in excess of $100\ \mu\text{m}$, especially when the mean particle diameter in the interface layer decreases due to crushing.

Lending further support to the concept that abrasion of a smooth surface leads to a stress ratio elevation, is the results from testing of a glass bead - Stainless Steel interface. The glass bead results shown in Figure 4.4 display no increase in stress ratio with continuous shearing at a low level for the duration of the test. The glass beads have a low abrasive effect due to their spherical shape. For context, Nardelli and Coop (2019) reports that for the Fraction A sand being used in this testing, the sphericity is 0.8 and roundness is 0.7. Whereas for a *spherical* glass bead both the sphericity and roundness values will be 1. However sphericity and roundness are overall particle parameters — for interface friction what is important is the local shape effects at the interface itself. One relevant parameter is the attack angle β , as shown in Figure 4.1, which is minimal and constant for glass beads. This attack angle is taken relative to the interface surface, and is the angle between the horizontal and the tangent to the particle at the point of contact with the interface. It is the complementary angle to the attack angle α , referred to in Section 2.2 and Figure 2.11. Where in the literature of tribology, attack angles are drawn from the centroid of a solid, creating the angle α . For an irregular grain, the centroid is less easy to define, so the attack angle β is used instead, where drawing the angle relative to the surface may be more intuitive for those from a geotechnical background. If the breakage and crushing of grains was only a symptom of the high stress ratio state in the interface layer, then no crushing should be present in the glass bead sample at the end of the tests, as the transition never occurred. This is confirmed on dismantling the sample and shown in the plot of vertical displacements in Figure 4.6.

Although the condition of the macroscopic interface surface at the end of shearing can provide a certain level of fundamental understanding of the mechanisms at work, insights gained are merely an average across a developing and variable interface over the duration of each test. It is known that the relative roughness, recalling Equation 2.28, is crucial to interface response, yet as has been

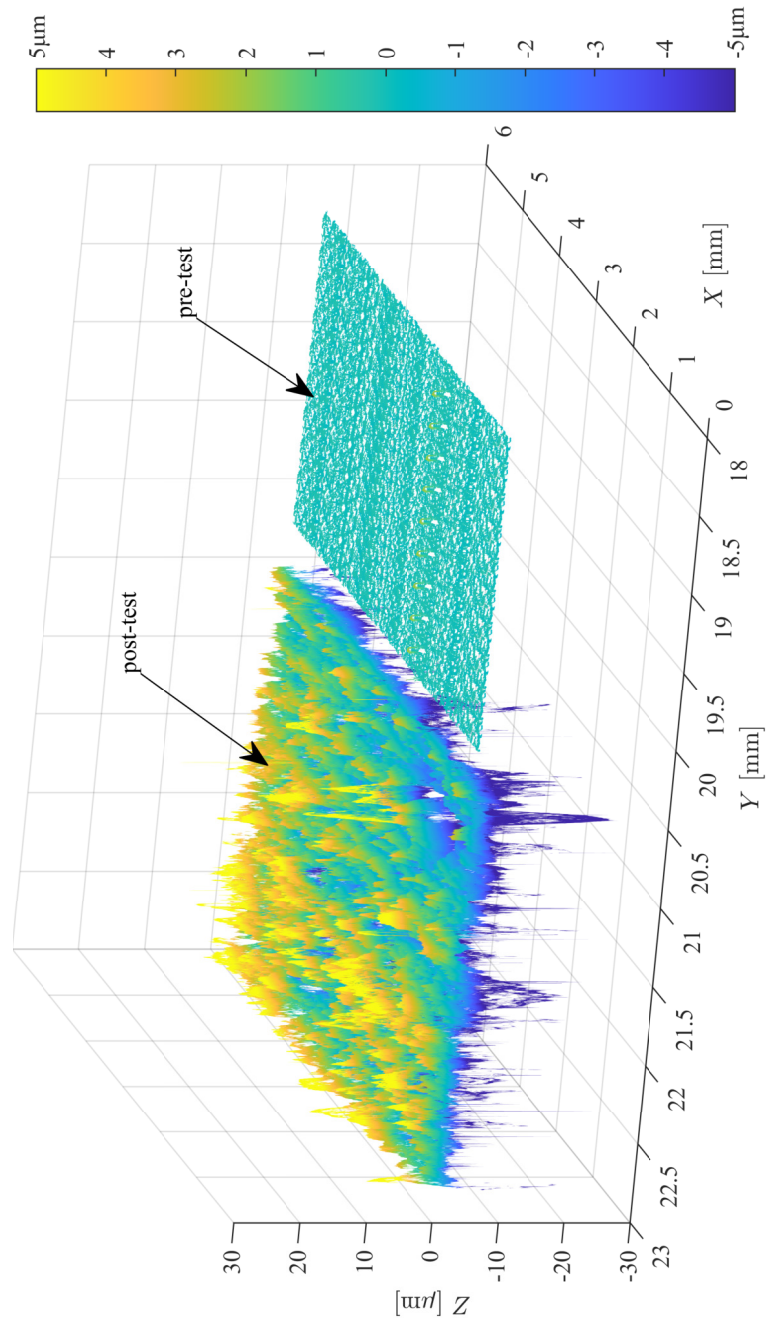


Figure 4.8: Excerpt of interferometry sampling of Fraction A — Stainless Steel macroscopic interface pre-test and post-test

shown by the volumetric response (Figures 4.6, 4.7) and condition of material at the interface after shearing (Figure 4.8), this parameter will change significantly over a large number of shears as R_{\max} and d_{50} change. Therefore, it is useful to take a more specific approach and consider only the influence of a change in R_{\max} which was the driving force behind the single-particle shear testing. The adoption of single-particle testing simplifies the interface analysis to remove the impact of global soil behaviour and changes in the particle size, thus isolating the role of abrasion on the interface stress response.

4.6.3 Single-particle Testing

Figure 4.5 displays the stress ratio response, as it varies with cumulative energy, of all single-particle tests conducted on a Fraction A - stainless steel interface. As shown, there is some level of variability in stress response caused by the inherent variability of shape in natural granular material. The influence of shape on single-particle shearing cannot be underestimated - traditional tribological analyses use diamond, pin-shaped styluses in similar testing to remove the influence of shape (Lindroos et al., 2015). In Figure 4.5, a stress ratio elevation occurs, where initial shearing stress ratio was on average 0.2 and the ultimate stress ratio was on average of 0.5, with variation between 0.6 and 0.4. The increase in the stress ratio occurred within a range of cumulative energy of 0 J to 30 J. Crucially, Figure 4.5 shows that confining masses has a comparatively insignificant impact on the stress ratio, indicating particle shape is the most significant factor impacting shear response. The glass bead data provides a crucial reference for the influence of shape effects. Given an equivalent amount of shear energy expenditure, the glass bead did not develop any increase in stress ratio over the duration of its test, an identical outcome to the macro scale shown in Figure 4.4. The *spherical* glass bead does not cause a stress ratio elevation, due to its minimal abrasive impact. The difference in particle shape is hypothesised to account for the different point (i.e. different energy level) of stress ratio elevation in single-particle tests. Further work will be carried out to investigate the impact of shape on interface shearing.

Interferometer sampling has been carried out on five mild steel single-particle test interfaces which can give more context to the stress response of single-particle shearing. An example interferometer surface plot can be seen in Figure 4.9. Notable from this plot is the trough ploughed into the planar interface by the particle and the ridges generated at either side of the particle contact area.

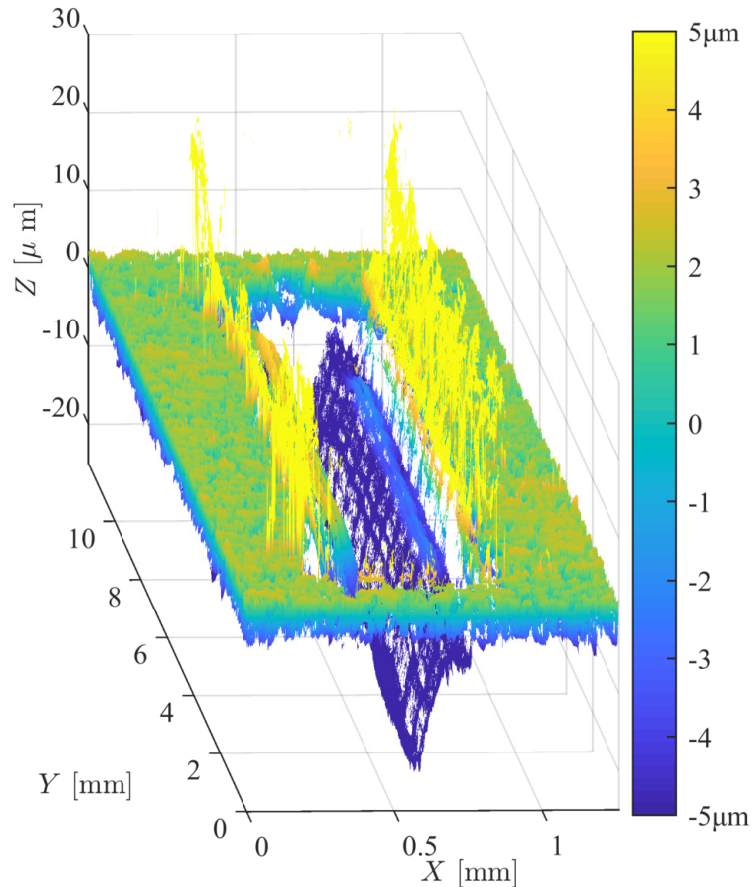


Figure 4.9: Single-particle interface shear interferometer surface plot

The two indicative interferometry samples (Figures 4.8, 4.9) appear very different. Evidently, the multitude of particles abrading the interface in the macroscopic tests will produce a different abrasive effect. There is also a fundamental difference between the shear modes at the interface as a result of the level of constraint on the granular media.

As mentioned in the introductory sections and shown in Figure 4.1, the single-particle experiencing shear is held in a fixed orientation, or, in tribology terms, a *two-body* abrasion system. Whilst the particles adjacent to the interface in the macroscopic sample exist in a *three-body* system (Hutchings and Shipway, 2017) as they are able to rotate in between the interface and far-field soil. Literature reports that two-body systems tend to have more damaging abrasive effects than three-body systems (Gates, 1998). This knowledge of two and particularly three-body systems, is insightful in the context of granular soils research. DeJong et al. (2003); Uesugi et al. (1989) reported that soil outside of the interface layer (5 to $10 \times d_{50}$), the far-field soil, has a negligible impact on interface behaviour. In

three-body shearing, the abrasion of the surface is not affected by the properties of the confining body (Gates, 1998). The similarity of findings of these two disparate areas of research gives further justification to the motivation of investigating interface behaviour in the context of material wear and abrasion.

4.7 Discussion

4.7.1 Stress Ratio Elevation

The results provided by both macroscopic direct shear and single-particle shear apparatuses prove the existence of a previously unobserved change in shearing behaviour for initially ‘smooth’ soil-structure interfaces. Verification of the elevation mechanism, first captured through experimentation at the macroscopic scale, was achieved by use of a completely separate apparatus, analysing the distinct interaction of a single grain and structural interface. It is evident that the interface, regardless of number of particles present, sees an increase in stress ratio after a given amount of shearing energy is expended. The steep incline in stress ratio μ occurs over a small region of energy expenditure, showing the change in mechanism occurs almost instantaneously.

Figure 4.10 shows the mean stress ratio and volumetric response for the already presented $\sigma_n = 100$ kPa tests, with a comparison to the mean response of two CNL $\sigma_n = 50$ kPa tests. Shown in the inset of Figure 4.10 is the stress response over the first 25 cycles for both tests. The stress response over the first 25 cycles is remarkably similar, before significant abrasion has set in. Some key differences across the entire 1500 cycles are clear; most notably, the peak stress ratio achieved in $\sigma_n = 50$ kPa tests is higher than that of the 100 kPa tests.

The initial shear mechanism at low stress ratios was that of sliding (i.e. minimal abrasion); this is supported by image data from macroscopic tests which show minimal deformation or rearrangement of particles within the interface layer. Further support is offered by macroscopic testing that was stopped before the elevation in stress ratio had occurred, and from other tests which were stopped mid-way through the elevation of stress ratio (Hashemi and Heron, 2017; Pettey and Heron, 2020) (see Appendix A). In these studies, interface plates from these prematurely stopped tests were removed and inspected, and it was found that signs of wear to the interface were not perceptible to the eye for the tests stopped prior to the elevation of stress ratio. Varying degrees of damage were

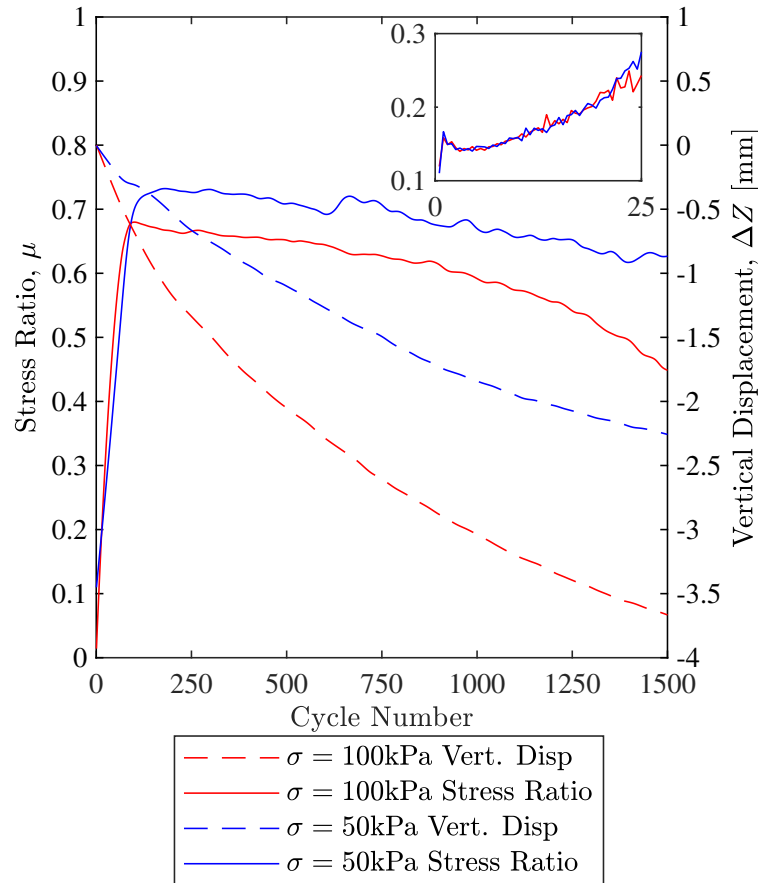


Figure 4.10: Comparison of average stress ratio and volumetric response in macroscopic direct shear test where $\sigma_n = 100$ kPa and 50 kPa

observed for tests stopped during the elevation. Upon completion of the stress ratio elevation, the entirety of the shearing area was visibly damaged, as supported by the interferometry data presented in Figure 4.8.

The shear stress response over individual cycles is different before and after the observed stress ratio elevation. Figure 4.11 shows the shear load vs shear displacement response for cycles 5, 500, and 1500 - representing the pre-elevation, post-elevation, and post-elevation degraded shear behaviour, respectively. Pre-elevation behaviour is elastic-perfectly plastic, indicative of a mainly sliding mechanism as shear load reaches its maximum immediately on shear direction reversal. However, the post-elevation behaviour is very different. When a shear reversal occurs in the post-elevation state, there is a sustained increase in shear load across a single shear (half-cycle), reaching an ultimate value by the end of each shear. This increase in shear load, with an associated increase in energy expenditure per shear, indicates the divergence from the pre-elevation mechanism;

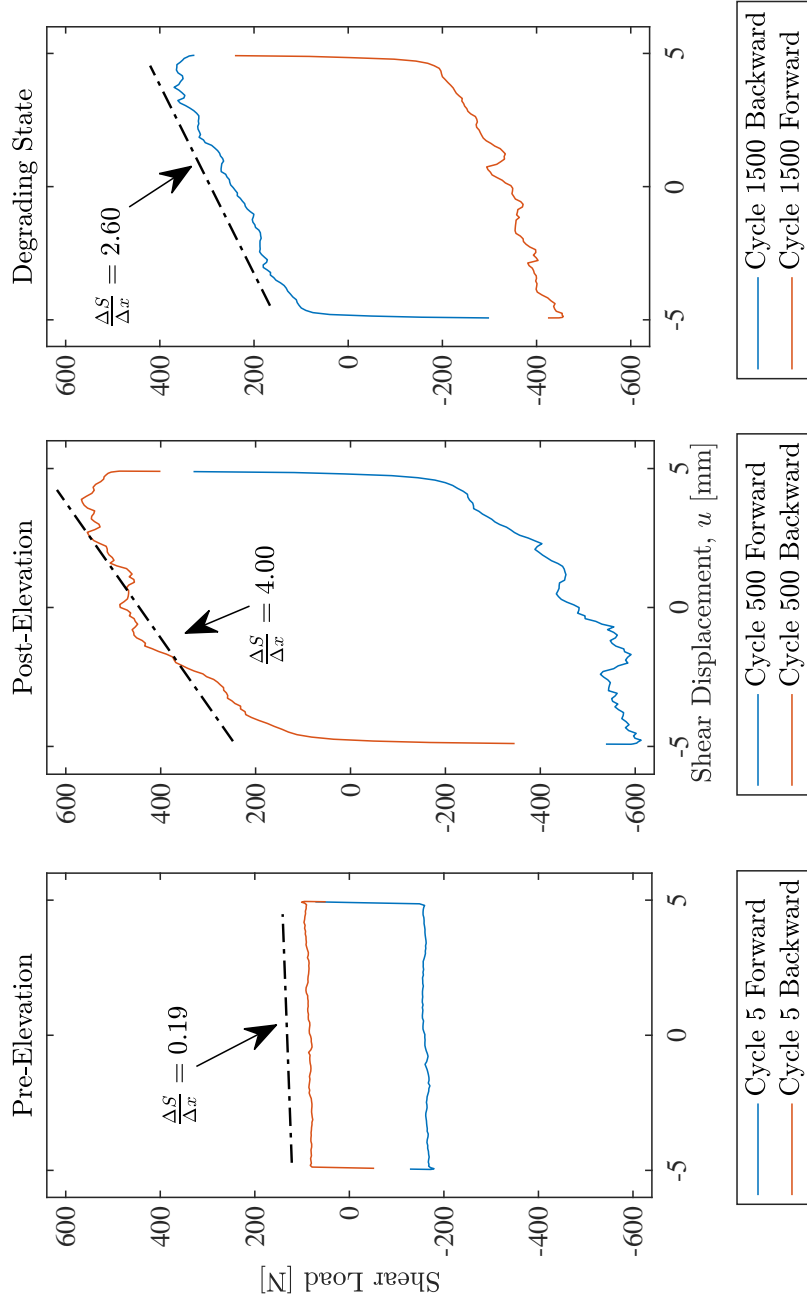


Figure 4.11: Plots of shear load against shear displacement showing pre-elevation, post-elevation elevated, and post-elevation degraded shear behaviour in a macroscopic direct shear test where $\sigma_n = 100$ kPa

there must exist, therefore, some other interaction between the granular body and structural interface. This will be explored further later where an explanation of the potential causes of the increase in shear load per shear associated with the elevation in stress ratio will be presented.

4.7.2 Influence of abrasion

The constituents of the interface and their material properties have an effect on the change in mechanism and elevation behaviour as a result of their role in abrasion. The structural interface is sheared by the *relatively harder* granular media, resulting in damaging abrasion. The wear rate of a surface is dependent on the difference in hardness between the surface H_s and the abrasive particle H_a (Hutchings and Shipway, 2017). Recalling the relative hardness, R_H , defined in the literature review (Equation 2.21). Figure 2.10 illustrates the conditions under which the particle or surface will plastically deform in abrasion. The wear rate of a material is significantly increased when the relative hardness is greater than ~ 1.2 , as the figure indicates. Invasive testing of the 304 grade stainless steel used as the structural interface used in this study judged the hardness value to be an average of 112 HV. The hardness value of LBS grains has been found to be approximately 500 HV (Sandeep and Senetakis, 2018). As such, the relative hardness of the interface is a minimum of $R_H = 4.46$, indicating that this interface will see extreme abrasive wear. Given the scale of difference in hardness, mild steel (which is softer than stainless steel) will also suffer extreme abrasive wear. Figures 4.8 and 4.9 prove this does indeed occur in both the macroscopic and single-particle samples. It is worth noting here, given the large relative hardness, that the standard “saw-blades model” (Bolton, 1984) relating strength and volumetric response does not hold for interface shear, as it relies upon both “saw-blades” being equivalently hard.

Figure 4.12 shows the shear load variation with displacement across one cycle in pre- and post- elevation states for single-particle shearing, similar to that presented in Figure 4.11 for a macroscopic sample. The most notable insight given by this data is that whilst the magnitude of shear load carried by a particle in the post elevation condition is greater, the nature of response (i.e. elastic-perfectly plastic) does not change.

Having established the cause of the stress ratio elevation observed in single-particle and macroscopic tests, it is worth considering the difference in per shear

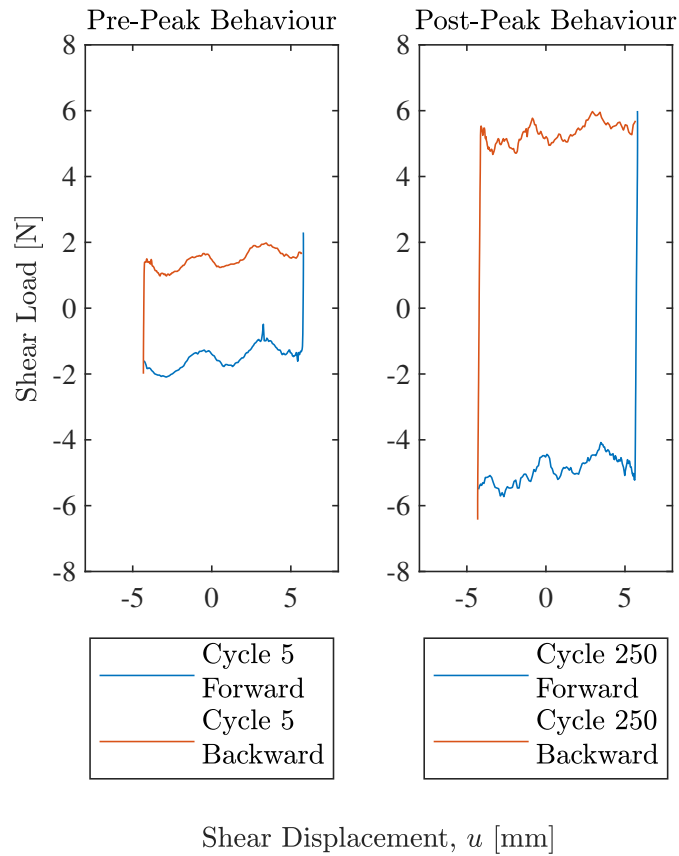


Figure 4.12: Plots of shear load against shear displacement showing pre-elevation and post-elevation shear mechanism in a single particle interface shear test

(half-cycle) response once the elevation has occurred. Key to this difference is the respective confinement condition of the particles at the interface. In single-particle tests, the particle is under a normal load and in a fixed orientation, as though it were under a stiff force chain perpendicular to the surface. The macroscopic case is different, where the orientation of the particles in the interface layer are only partially confined by the far field soil. Shear reversal causes a reorganisation of the particles at the interface and consequently the force chains in the sample.

There is a gradient of shear load across each half cycle, shown in Figure 4.11 ($\Delta F_x / \Delta F_z$), which is directly correlated with the magnitude of shear load (and therefore stress ratio). One explanation for this is the increased likelihood of reorientation of a given grain when subjected to a higher shear load. After reversal, the reorientation of the particles at the interface and the corresponding redistribution of force chains, will not occur instantaneously. Particles rearrange throughout each shear displacement (i.e. each half cycle). This rearrangement is

4. ABRASION IN CYCLICALLY SHEARED INTERFACES

a result of changes in the force chains. At the point of reversal the force chains will be vertical as no shear load is being transmitted. As shearing then starts, the force chains will transition from being vertical to being inclined. Hence the shear load will increase across each shear displacement.

Having established that interface abrasion of a smooth interface does indeed cause a stress ratio elevation, it is worthwhile to consider the underlying factors influencing abrasion of the structural interface. It was shown that the relative hardness R_H and confinement condition (two/three-body abrasion) define the mode of abrasion at the interface. Hutchings and Shipway (2017) provide a general equation, Equation 2.26, for the specific energy for material removal U , or the “frictional work expended per unit volume of material removed” from a single-particle abrading a surface. The total volume of material removed from the surface is dependent on the cutting-plasticity ratio, η , and the attack angle of the abrasive particle, for example β (shown in Figure 4.1). These parameters are greatly dependent on particle shape.

The surface profiles of the five Fraction A — mild steel tests at the end of shearing, exemplified by Figure 4.9, allow for calculation of the cutting-plasticity ratio, η (Equation 2.27). The ratio is defined as the ratio between volume of material removed from the surface through abrasive cutting and the volume of material displaced through plastic deformation, found from interferometry data of the surface. A schematic exemplifying the regions these volumes are calculated from is shown in Figure 4.13.

These volumes are calculated by placing a threshold planar surface at the mean Z -coordinate of the virgin area scanned, and integrating to find the volume above (Vol_{above}) and below (Vol_{below}) this threshold. A value of $\eta = 0$ indicates a mechanism of purely plastic flow, whereas a value of $\eta = 1$ indicates cutting of material from the surface. Analysis of this value for the various tests will show if

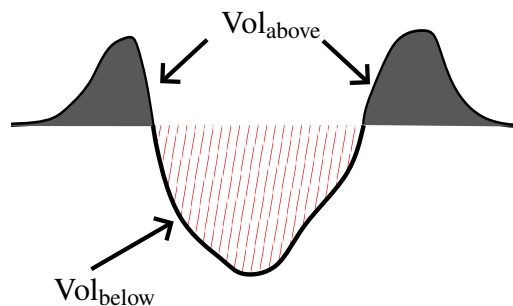


Figure 4.13: Schematic showing method for calculating cutting plasticity ratio

4.7. DISCUSSION

the type of abrasion influences the stress response. Figure 4.14 presents the stress response of five single-particle tests with the associated cutting-plasticity ratio, η , marked against their curve. A clear pattern is shown, wherein interfaces with lower values of η reach their peak stress ratio after fewer shear cycles. In the case of two tests with very similar η values of 0.513 and 0.514, the stress ratio response at high shear numbers is also remarkably similar. As such, it could be concluded that a higher resistance to shearing is mobilised where deformation to the interface surface is caused by plastic flow as opposed to cutting wear. The η value is a measure of deformation mode over the entirety of the test, in this respect it shows the average deformation mode. For example, Sample D in Figure 4.14 shows a further increase in stress ratio after the initial elevation event (at around 750 cycles). Although the interface surfaces were only analysed at the end of shearing, the damage experienced by the interface is cumulative over the duration of a test. The interferometry data clearly shows that in the elevated stress state, there are varied abrasive mechanisms damaging the structural interface that influence the magnitude of stress transfer. Evidently, plastic flow of the structural interface provides more resistance to shearing than cutting or chipping material away from the surface. In some single-particle tests, metallic fragments were clearly visible after shearing, supporting the assertion from calculation of η that some material is cut from the structural interface. Unfortunately, most tribological analyses are more concerned with the material response to indentation or abrasive wear by free granular material within the context of industrial processing. For example, Lindroos et al. (2015) began to consider the shear behaviour of a quartz particle on high strength steels before simplifying the process by using a uniform shape diamond stylus. Further investigation is needed to discover the role of granular shape effects on not only the cutting-plasticity ratio but also the stress response of interface shearing in general.

4.7.3 Stress Ratio Degradation

In addition to the novel stress ratio elevation mechanism change, as relatively harder samples move from sliding across the structural interface to causing plastic, abrasive wear, there is another mechanism that is identified within the macroscopic direct shear data available, one of stress ratio degradation. Degradation can be seen to occur at normal stresses of 100 kPa and 50 kPa, being characterised by a sustained and increasing rate of reduction in stress ratio (Figure 4.10), with an

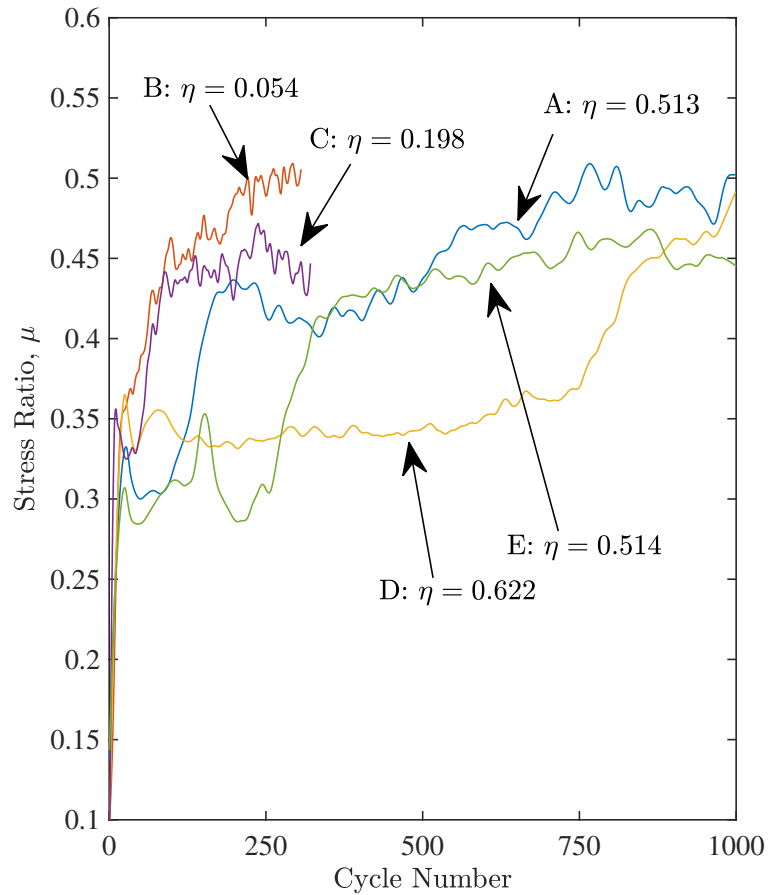


Figure 4.14: Single-particle interface shear stress response with comparison to the cutting-plasticity ratio η for mild steel interfaces with 500 g of applied load

associated contraction in volume caused by crushing of particles in the interface layer (Figures 4.10, 4.7). Furthermore, the shear response gradient across each shear reduces as observed in Figure 4.11. It is hypothesised that the degradation in stress ratio, which is of a much greater magnitude than the degradation referred to by DeJong et al. (2003); Mortara et al. (2007), is caused by a saturation of the interface layer by fine particles of $d_{50} \approx 63 \mu\text{m}$, identified by sieve analysis (although not presented due to the previously mentioned stratification of the interface layer), which was identified in Pettey and Heron (2020). A saturation of the interface layer refers to this layer becoming filled with fine material, which is generated by crushing of particles in the interface layer. Inverted tests, conducted in Pettey and Heron (2020) (see Appendix A), showed that the fine material is generated directly by crushing in the interface layer, as particles were witnessed to fall away from the interface layer. This behaviour was also witnessed in Ho et al. (2011).

4.7. DISCUSSION

Notably from Figure 4.10 when considering the post-elevation degradation, rate of contraction for $\sigma_n = 50$ kPa tests was much lower than for the greater 100 kPa tests, regardless of the greater stress ratio level reached by the lower normal load tests, proving the rate of crushing is not proportional to stress ratio but rather the magnitude of stress concentrations in the interface layer. It is however not possible to measure these stress concentrations experimentally.

There is a direct link between the rate of contraction and the rate of stress ratio degradation post-elevation for a given normal stress. It was shown how, in the elevated stress state, crushing is occurring solely in the interface layer (Ho et al., 2011; Pettey and Heron, 2020). By the end of testing, with a build up of fine material, the size of the interface layer will have substantially reduced, as its size is dependent on d_{50} . The reduction in rate of contraction can equally be attributed to one of two characteristics of the crushing of finer materials. Firstly, smaller particles have a greater associated crushing strength, meaning further crushing is less likely to occur. Secondly, in the event of crushing, smaller particles have a smaller associated contractile effect on global volume. What these two characteristics do suggest however, is that the interface layer may become saturated by fine material, leading to the reduction and eventual cessation in volumetric contraction. The reduction in rate of contraction shows that even with continued shearing, particles that exist outside the interface layer, seen in Figure 4.7, will not be subject to crushing, else the rate of contraction (Figure 4.10) would be constant as the entire sample is crushing. This is supported by early studies into interface behaviour that judged particles outside of the interface layer to be insignificant in shearing (DeJong et al., 2003; Hu and Pu, 2004).

It was shown that an increase in stress ratio is caused by abrasive wear to the structural interface, as plastic deformation provides a resistance to shear. Conversely, a reduction in stress ratio from the peak level must be caused by a cessation, or at the very least a reduction in the level of plastic deformation to the structural interface. This point is crucial in the difference between single-particle and macroscopic direct shear tests. In single-particle testing the particle is in a fixed orientation. Unless catastrophic failure of the particle occurs, the process of two-body abrasion continues unless some other medium prevents this abrasion from taking place. In macroscopic direct shear tests sieving analysis shows fine material, smaller than $63 \mu\text{m}$, is generated through crushing of particles, and builds up in the interface layer. This fine material is found to settle in the new abraded grooves of the structural interface, becoming fixed in place whereby

agitation of the surface with a brush does not dislodge all fine material. This was also observed by Ho et al. (2011). As these grooves become full of the fine material, less abrasion is taking place, reducing the amount of stress transfer at the interface. In this state the soil-structure interface has potentially become a soil-soil interface as the interface layer has saturated with fine material and a soil-soil shear band has formed. This is supported by the final recorded stress ratio of approximately 0.57 (average of the 50 kPa and 100 kPa tests) gives a friction angle of 30 degrees, which is a typical friction angle for LBS sands across the different fractions (particle sizes) commercially available.

In summary, the reason for the degradation in stress ratio is due to a transition from grain-stainless steel to grain-grain shearing. This is not an instant transition because of the need for on-going crushing and rearrangement of the crushed material to establish a shear band dominated by grain-grain interactions. More research, including further shearing beyond 1500 cycles, is needed to validate this hypothesis by investigation of the stress response after an accumulation of fine material in particle-interface shear.

4.8 Conclusions

When soil is sheared against a structural body, a traditional analysis involving a simple frictional model is not entirely sufficient to describe the behaviour. At a soil-soil interface, both bodies are equivalently hard, and wear to the soil medium may arise as a result of stress concentrations leading to particle breakage. At a soil-structure interface the difference in material properties, particularly hardness, of the constituent materials can lead to abrasive wear over the course of thousands of cyclical shears. In the case of a quartz sand - stainless steel interface where relative hardness, $R_H = 4.46$, the softer stainless steel interface will be subjected to abrasive wear by a mixture of plastic flow and cutting. The type of abrasive wear is influenced by the boundary condition on the particles in the interface layer. In this study, abrasive wear was proven to have occurred in the macroscopic samples tested by conducting a series of single-particle interface shear tests. This abrasive wear is clearly identified through surface profiling by white-light interferometry carried out on both the macroscopic and single-particle interfaces. A notable trough had been ploughed into the single-particle interface, as the particle abrades the surface in a two-body abrasion mode, where the particle is in a fixed orientation.

4.8. CONCLUSIONS

As a result of abrasive wear, a stress ratio elevation occurs in both macroscopic and single-particle tests. For macroscopic shearing this manifested as a steep and sharp rise in the interface stress ratio with an associated increase in the rate of vertical contraction of the sample, as crushing of the soil medium begins to occur within the interface layer. The elevation mechanism, shown to occur over the first 150 shears of testing, has been as yet unobserved in other interface studies. This absence is likely due to the use of testing parameters that do not generate the energy required to bring about this change in shear behaviour, most notably the common use of constant normal stiffness boundary conditions which results in lower applied vertical loads due to sample contraction. For the purposes of validation of the macroscopic interface shear apparatus, a constant stiffness boundary was tested and almost identical behaviour was seen to other studies. Single-particle testing has proven the existence of this elevation mechanism in interface shear is not a function of the apparatus or specific conditions tested but occurs generally where the soil is relatively harder than the interface. The exception is when using spherical glass beads which have a minimal attack angle and abrasive effect. It has also been found that the particle shape influences the magnitude of stress ratio elevation, as a function of the primary abrasive wear mode, plastic flow or cutting. Particles that had a bias towards plastic flow mobilised a greater shear resistance at an earlier cycle number than those with a cutting bias. Tribology theory suggests that the wear mode is dependent on attack angle of the abrasive particle on a planar surface, which can be related to particle shape characteristics and is to be examined in a subsequent study.

In addition to the novel stress ratio elevation, a sustained fall in stress ratio or degradation was also witnessed in macroscopic testing on continued shearing of the sample after it had reached peak stress ratio. The degradation witnessed in this study amounted to a 20 % fall in stress ratio over 1250 cycles. It is shown that this fall in stress ratio arises as a result of particle breakage only within the interface layer.

The rate of contraction of the sample is greatest when the maximum stress ratio is mobilised at the interface. The rate of contraction is shown to be proportional to the normal stress on the sample — whilst samples with a lower normal stress reached a greater peak and ultimate stress ratio, the rate of contraction was higher for samples under the greater normal load. The rate of contraction falls as the proportion of fines in the interface layer increases and it is hypothesised that as the interface layer, or more specifically, the abraded structural

interface, becomes saturated by fine material ($d_{50} < 63 \mu\text{m}$), a new sand-sand interface may be established.

In summary, this chapter has achieved Objectives 1 and 2 of this thesis, as stated in Chapter 3. By conducting a series of macro scale and particle scale interface shear tests, at far larger numbers of shear cycles than previously conducted, the mechanisms of stress ratio elevation and subsequent degradation have been identified. It can be concluded that there is a link between the macroscopic and single-particle interface behaviour, as the stress ratio elevation mechanism has been shown to occur in both cases, which satisfies Aim 1 of this thesis. Furthermore, the experimental analysis conducted in this chapter suggests that abrasion plays a key role in the long-term behaviour of the soil-structure interface, which begins to satisfy Aim 2 of this thesis. In the next chapter, a further development of this investigation of the role of abrasion in soil-structure interface behaviour will be presented.

Chapter 5

Quantifying Interface Abrasion with Particle Virtualization

5.1 Notes

This chapter is reproduced from the Geotechnical Testing Journal entry (Petty and Heron, 2023a). Where necessary, changes have been made to reflect the continuous narrative required for a thesis, mainly to the introduction which draws on elements of the established literature review.

5.2 Introduction

It is well established that single-grain (particle) form and roughness govern the global response of soils in soil-soil interaction (Fonseca et al., 2016; Nardelli and Coop, 2019; Sandeep and Senetakis, 2018; Senetakis et al., 2013; Todisco et al., 2017). In soil-structure interfaces, the local grain morphology at the contact point between the grain and interface is crucial in the interaction. An accurate representation of this irregular geometry is required to advance fundamental understanding of soil-structure interface behaviour, where it has been shown in Chapter 4 that abrasion affects the long term response. Also shown in Chapter 4 and concluded in the Literature Review (Chapter 2), the local grain morphology is crucial in the wear mode of the interface in single-particle shear, and hence will be a factor in the macroscopic response of the interface. In this chapter, Aim 2 of the thesis, the investigation into the role of abrasion at soil-structure interfaces, will be further addressed in this chapter. To achieve this, this Chapter will target

5. QUANTIFYING INTERFACE ABRASION

Objectives 3, 4 and 5 (as set out in Chapter 3) to establish a method for capturing the local grain morphology of sand grains, and to use this method to quantify the abrasive wear of the sand grains in single-particle shear — which at present has not been possible. This new methodology will then enable an investigation of the role of shape in single-particle—interface shear, which is the final Aim of this thesis.

Significant progress has been made towards capturing real geometries of grains to be used in numerical simulations for more informed results than the spherical ‘grains’ initially used in discrete modelling (Cundall and Strack, 1979). Non-invasive methods such as computed X-Ray tomography have been used to accurately capture particle form of ballast and large sand grains (Harmon et al., 2020; Medina and Jerves, 2018; Vlahinić et al., 2014; Zhao and Wang, 2016). The scale of such methods cannot be reduced further to examine smaller fractions of granular materials due to the noise generated at the particle boundaries. Whilst this method excels in accurately collecting the form of many grains in one scan, it does not capture the local angularity of grains, which is known to be crucial in single-particle — interface interaction. This is contrary to optical volume reconstruction used by Nadimi and Fonseca (2017) which, whilst only having the ability to capture one-grain at a time, can be scaled appropriately to capture the local angularity of smaller fractions of grain size.

Modelling the contact geometry is an issue that has previously been avoided when considering abrasive wear. Lindroos et al. (2015) attempted to model the abrasive characteristics of irregular rock tips before simplifying their analysis by using conical diamond styluses. The 1D attack angle formed when an abrasive contacts a planar surface is a factor in how damaging this process is (Hutchings and Shipway, 2017), making it an important consideration in the wear of structural materials by sand bodies. In Chapter 4 the apparatus and method for cyclically shearing a sand grain in a fixed orientation against structural surfaces was presented. In these experiments, a Leighton Buzzard Sand (LBS) Fraction A particle with mean particle diameter d_{50} of 1.5 mm was affixed to the end of a bolt head, which was monitored during testing through the use of a microscopic imaging apparatus. The resulting images provide an insight into the shearing mechanism but could not capture an accurate representation of the contact grain geometry due to the 2D nature of the images — a 3D model of the contact geometry is required prior to testing. It was observed in the 2D images that the sand grain displayed some change in shape at the contact point. This chapter has presented enhancements

made to the particle virtualization method first presented by Nadimi and Fonseca (2017), to capture the grain geometry prior to and post-test in single-particle shear. With this data, the wear of the sand grain can be accurately computed in terms of height and volume loss at the contact point and also allows for complex shape analysis. New insights regarding the interaction between sand grains and a structural interface can also be discovered as the position of the grain is tracked throughout shearing.

5.3 Methodology

For this study, 15 LBS grains were virtualized prior to and after testing in a single-particle interface shear device. The required level of resolution to quantify the abrasive affect of interface shearing on the grains exceeded that achieved by the Nadimi and Fonseca (2017) method, hence the process of particle virtualization outlined by Nadimi and Fonseca (2017) was enhanced. In doing so, a number of challenges were presented that required extra physical constraints and data processing that would not have been uncovered by the original study. Where appropriate, the differences between the method adopted in this study and the Nadimi and Fonseca (2017) will be highlighted, with a explanation of why this change was required.

5.3.1 Overview

An overview of the process of particle virtualization is displayed graphically in Figure 5.1. In summary, a series of images of the cross section of the grain are taken at 40 rotation points in 9° increments. At each rotation point several images are captured at various focus points through the depth of the grain to carry out focus stacking — allowing a singular focused image at high resolution to be obtained. Each focus stacked image is binarised using Otsu thresholding (Otsu, 1979). The binary images are projected into the third dimension — by repeating the array as many times as the width of the full image — to create a 3D binary array, which is rotated by the corresponding rotation angle from which the image was captured. Elementwise multiplication of each rotation point's 3D projected array will give the intersection of all of the cross sections, and hence the real 3D geometry of the grain (i.e. only where an element exists in all projections will it exist in the grain).

The apparatus used for particle virtualization is displayed in the schematic in Figure 5.2a.

5.3.2 Focus Stacking

In order to achieve the required resolution of the final reconstructed geometry of the grains, the initial imaging of the grains was conducted using a 10× Leica microscope objective and Teledyne DALSA Genie Nano camera unit with a stated resolution of 4112×3008 . This allowed images to be collected in which the grain fills a large proportion of the imaged area. As such, a better virtualisation resolution (pixels per micron) than that presented by Nadimi and Fonseca (2017) was obtained. The use of a microscope objective has one major drawback however, a very narrow depth of field, in this case $10 \mu\text{m}$. As a result, images of the LBS grains with $d_{50} = 1.5 \text{ mm}$ would appear to be out of focus for two reasons. First, the depth of the grain is simply too large compared to the depth of field, and information in front or behind the point of maximum focus would be lost. Secondly, the grains were fixed to the head of an M5 bolt using adhesive and the bolt was then rotated to allow the multiple images to be collected. Attaching the grain so that its XY centroid lies at the centreline of the bolt head is practically difficult and as such, the grain moves towards and away from the camera as it rotates and hence moves in and out of focus. Focus stacking is a method for creating detailed images that are absent of blur, by combining all of the focused regions in several images into a single image. The particle rotates around the fixed axes of the stepper motor, and at each stop angle (000 [0°], 001 [9°], 002 [18°]. . .) an image is captured. Once the particle has completed one rotation, the micrometer controlled positioning stage on which the camera unit is mounted is adjusted to a new focal point. A new series of images are taken at the same rotation points, and the process repeats, assembling the images fs00, fs01, fs02 etc. for each rotation angle, as shown in Figure 5.1. An average of 12 focus point images were collected for each rotation angle, with smaller grains requiring less focus points to recreate a clear image. Subsequently, the images at each rotation point are combined by a specialist focus stacking software (HeliconSoft, 2022) to create a fully focused image, with a sharp outline, that fills a large area of the image frame maximising the obtained resolution (pixels per micron), as shown in Figure 5.2b.

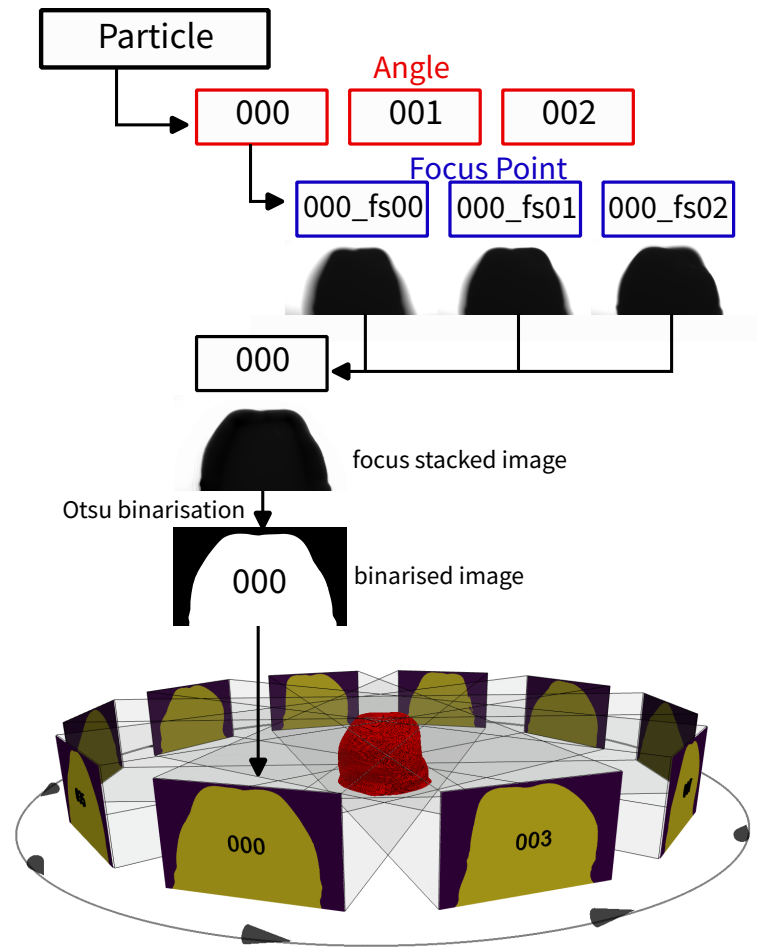


Figure 5.1: Overview of particle virtualization

5.3.3 Binarisation and volume realignment

To create a projection of the cross section of the grain at each rotation angle, each of the focus stacked images are binarised using the Otsu thresholding method included in the python module `skimage.filters` (*Scikit-Image: Image Processing in Python, 2022*). This is an automated process which maximises the inter-class intensity variance — separating regions of high intensity from low intensity. To help achieve this, the particles have been strongly backlit by a series of LEDs at a suitable distance away from the grain, creating a sharp silhouette. Following this, the binarised images must be realigned as a result of difficulties in having the grain positioned perfectly centrally on the fixing bolt. The grain moves ‘in to’ and ‘out of’ the frame as well as left and right in a sinusoidal pattern. To account for this, the images are rescaled and realigned in a two stage process by

making assumptions about grain geometry. Firstly, the images are rescaled. The maximum y -coordinate of the binary images must represent the tip of the grain, which can be assumed to be a fixed dimension. For example, should this point lie on the rotation axis, this coordinate would be unchanging between images. Each image is rescaled by a specific scale factor, such that the tips of the grain all lie at the same y -coordinate. Rescaling is used — as opposed to a raw translation — to account for parallax (the difference in projected size as the particle moves ‘into’ and ‘out of’ the frame). Secondly, the horizontal centroids of each binary area are realigned together. The centroid of any axis perpendicular to the rotation axis for a regular closed volume does not move with rotation. As such the volume can be reconstructed accurately as the projections will intersect each other on a constant path.

As shown in Figure 5.1, each binary image is projected into the third dimension and rotated by the angle at which the image was taken. The intersection of all the 3D arrays returns the real geometry of the grain. The 3D array is subsequently meshed using a fast Marching Cubes algorithm (Lewiner et al., 2003).

5.3.4 Angular realignment of pre and post-test volumes

To simplify the subsequent stages of analysis, it is useful to be able to measure the angle of the grain, relative to the initial pre-shear set of 39 focus stacked images, from any given image. This is beneficial when ‘re-virtualising’ the grains after single-particle shearing as it ensures that each rotation image is taken from an identical point in the pre and post image series.

Any given image of the grain can be compared against the pre-test reference images by selecting an in-focus region and ‘template matching’ against the reference images. Template matching (Lewis, 1994; *Scikit-Image: Image Processing in Python*, 2022) uses Fast Fourier Transformation (FFT) convolutions of a template and larger search array, to produce a correlation map across the possible positions of the template array inside the search array. The maximum correlation value across all 39 image comparisons gives most similar image and hence the most likely angle, at this stage with an accuracy of $\pm 4.5^\circ$. This uncertainty can be refined further, by manually rotating the grain across the 9° range in 1° increments and template matching again, to find the greatest correlation value. At this point, the angle of the particle is known relative to the pre-shear reference set and the

particle is rotated back to an angle of 0° before starting the post-test virtualisation process. As such, the 3D binary arrays and meshes pre and post-shearing are rotationally aligned to within $\pm 0.5^\circ$, this physical realignment that takes place before revirtualisation has the added benefit of allowing a ‘sense’ check to be carried out on the collected images during the post-test revirtualisation.

5.3.5 Vertical realignment of pre and post-test volumes

For comparison between the pre and post-test volumes, the grains must lie on equivalent axes with appropriate scaling. Slight changes in lighting or lens position can affect the output of the binarisation process, and as such the post-test 3D array must be realigned with the pre-test array. This is achieved through template matching a 2D region of the post-test array that is known to be unchanged, against the pre-test array. An example of this process is shown in Figure 5.2c, where the translucent particles are shown translating in the *XY*-direction over the true position of the particle. The maximum correlation identifies the location of the template array in the search array. It is known that the tip of the grain will change shape between single-particle tests. For this reason, a volume in the middle of the post-test scanned grain is selected for template matching as this will be similar between both 3D arrays.

First, the respective pre and post 3D arrays are flattened by summing perpendicular to the image plane, producing a flat image with the same dimensions as the binarised images. The reconstructed 3D arrays are a structured grid of ones (representing where there is particle material) and zeros (representing where there is not particle material), after this flattening process the resulting 2D array will consist of numbers representing how ‘thick’ or deep the particle is at that position. This process enhances the quality of the template matching process, whereby the depth of grain is also correlated in addition to the silhouette of the grain. In this sense, the process is correlating ‘2.5D’ arrays. This is shown in Figure 5.2c, where the true position of the grain has lower intensity towards the outer edges of the grain. Once the template region has been correctly matched, the post-test array can be translated onto an identically shaped array as the pre-test grain, from which comparison can then be made. In some cases, it is necessary to apply a scale factor to the post-test array, to maximise the correlation in template matching, minimising the error in geometry between the pre and post-test grains. To achieve this, a simple recursive binary search function was created to scale the

template array and conduct template matching in each recursion. An appropriate convergence limit of 0.01 % change in maximum correlation was used to end the recursive loop and select the best scale factor.

Another method was considered to realign the meshes, to allow for direct comparison of the pre and post-test meshes. Iterative Closest Point (ICP) is a method for aligning two point clouds, by iteratively finding the closest point in one cloud to each point in the other cloud, and then finding the transformation matrix that minimises the distance between the two clouds (Cignoni et al., 2008). This method relies on the point clouds being approximately realigned to begin with, which as a result of the physical angular realignment, is a reasonable assumption. However, the ICP method was found to be computationally expensive, and due to the density of points on the raw meshes, meant that the process was prone to errors that could be visibly detected. A known workaround is to downsample the point clouds, however this would reduce the resolution of the meshes and hence the accuracy of the comparison, and for this reason the ‘2.5D’ template matching method was used instead.

5.3.6 Vertical Displacement Tracking

In addition to the enhancements made to the particle virtualization methodology, a further enhancement has been made to the single-particle shear testing methodology first set out in Chapter 4. Shown in Figure 5.2d is a schematic of the process of vertical displacement tracking during single-particle shear testing. Over a period of 5000 shear cycles, 1000 individual 4112×3008 images are recorded using an identical imaging unit used in the virtualization process. Similarly to the realignment method, template matching is used to track the position of an in-focus and unobstructed feature on the edge of the grain. This method provides a good level of confidence in tracked position, with a mean confidence score of 0.986 across a given set of 1000 images. In a method similar to that used in traditional geotechnical Particle Image Velocimetry (PIV), a leapfrog value of 5 images is used to refresh the template region, that may have changed potentially due to lighting changes that rise from a strongly backlit image. To improve the accuracy of measurement, and avoid the ‘integer binning’ that arises from maintaining the same coordinate space as the raw images, a sub-pixel level method is implemented by fitting a quadratic curve to the FFT correlation map that is returned by the python Scikit-image template match function. A curve fitting function is used to fit

a curve to the surface (in the vertical direction) 10 values either side of the location of the maximum correlation. The resulting maximum of the quadratic function is taken to calculate the displacement between any image pair. One advantage of the displacement tracking method, is that the same process could be used to validate the horizontal compliance of the single-particle shear apparatus. It was found that, within the limits of the obtained resolutions, there was zero net horizontal movement of the particle, affixed to the end of a bolt head by fast-setting adhesive, throughout testing. As such, it is fair to assume that the adhesive connection is effectively perfectly rigid for the level of loads applied during shear (<2 N).

5.3.7 Resolution of Virtualized Grains

To quantify the resolution of the output mesh in terms of pixels per length unit, the particle virtualization apparatus was used to image a microscope calibration slide. It was found that a 0.1 mm scale has a width of 670 px. Hence, each pixel is 1.5 μm across, and each voxel (3D pixel) in the virtualized 3D array has a volume of 3.375 μm^3 . As stated earlier, the work presented in this chapter aimed to improve upon the previous resolution obtained by Nadimi and Fonseca (2017) in order to examine the impact of local particle shape on interface behaviour — for reference, the obtained resolution of 1.5 μm was a an improvement of three times over that previously achieved.

5.3.8 Grain Comparison

An example of both the pre- and post-test output meshes is shown in Figure 5.3. Subjectively, there is good comparison in the morphology of the grains. The realignment process has worked as expected, aligning the regions away from the tips of the grains, leaving a difference in tip coordinate (maximum Z coordinate) of the grains of 35 px, which equates to 52.5 μm . This methodology provides the capacity for unrivalled insight into single grain morphology and its resulting abrasive characteristics, in particular due to the enhancements made allowing for revirtualisation of the same grain post test and hence direct quantitative comparison.

5. QUANTIFYING INTERFACE ABRASION

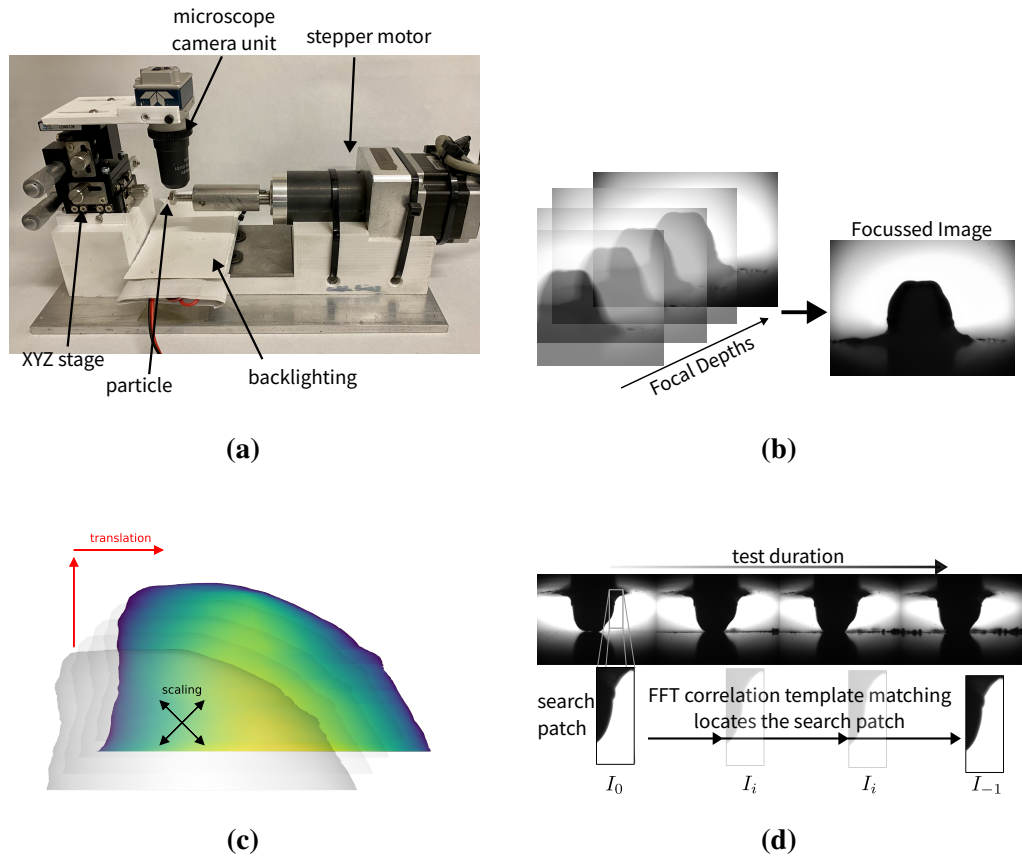


Figure 5.2: Particle Virtualization Framework: (a) Image of particle virtualization apparatus, (b) Focus stacking of images at different focal length, (c) Rescaling of post-test images based on image similarity, (d) Schematic of image-based particle depth detection

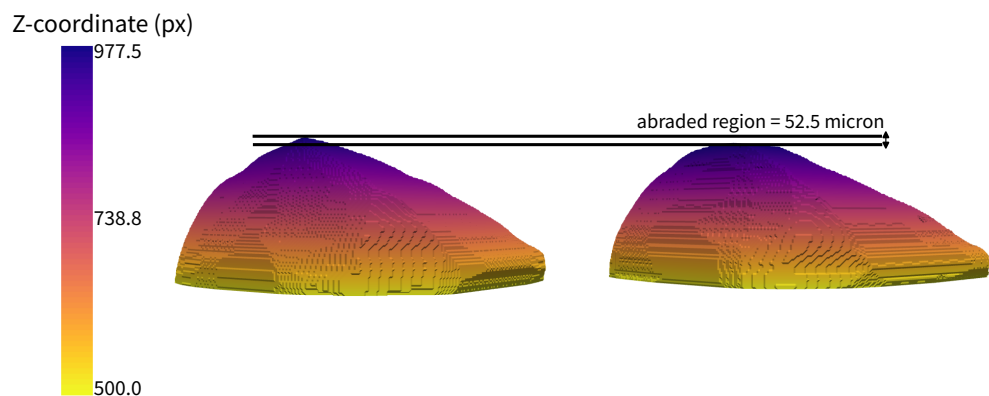


Figure 5.3: Comparison of pre and post-test grains meshes with maximum Z coordinate representing tip stated

5.4 Results and Discussion

The results from 15 single-particle interface shear tests are presented below with the insights obtained from particle virtualization and vertical displacement tracking being discussed.

5.4.1 Quantifying Abrasive Wear of Interface Bodies

Table 5.1: Comparison of volume of abrasive wear of particle and interface after shearing

Test	Volume Abrasion (μm^3)	
	Particle	Interface
441	0.0127	0.0180
202	0.0000	0.0079
225	0.0004	0.0018
528	0.0081	0.0095
623	0.0082	0.0217
948	0.1256	0.0255
834	0.0000	0.0159
627	0.0145	0.0090
939	0.0005	0.0135
521	0.0001	0.0106
727	0.0005	0.0106
040	0.0004	0.0038
915	0.0036	0.0183
552	0.0302	0.0406

Using the particle virtualization methodology it is now possible to directly compare the quantities of abrasive wear of both bodies involved in the soil-structure interface (i.e. the structural element and the soil grain). For analysis of the stainless steel interface, white-light interferometry is used following the same method set out in in Chapter 4.

Traditionally, abrasive wear is quantified in terms of the volume of material removed. Recalling from the literature, relative hardness, R_H , is the ratio of hardness of an abrasive particle, H_a , and surface, H_s , in an abrasive system

5. QUANTIFYING INTERFACE ABRASION

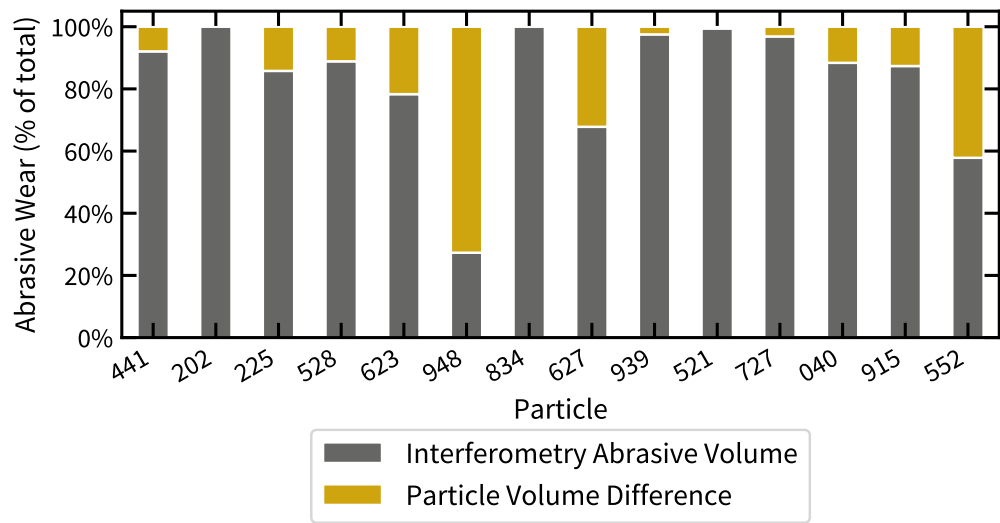


Figure 5.4: Stacked bar plot comparing the proportions of abrasive wear in terms of volume lost from the tip of grains, and volume abraded from interface surface

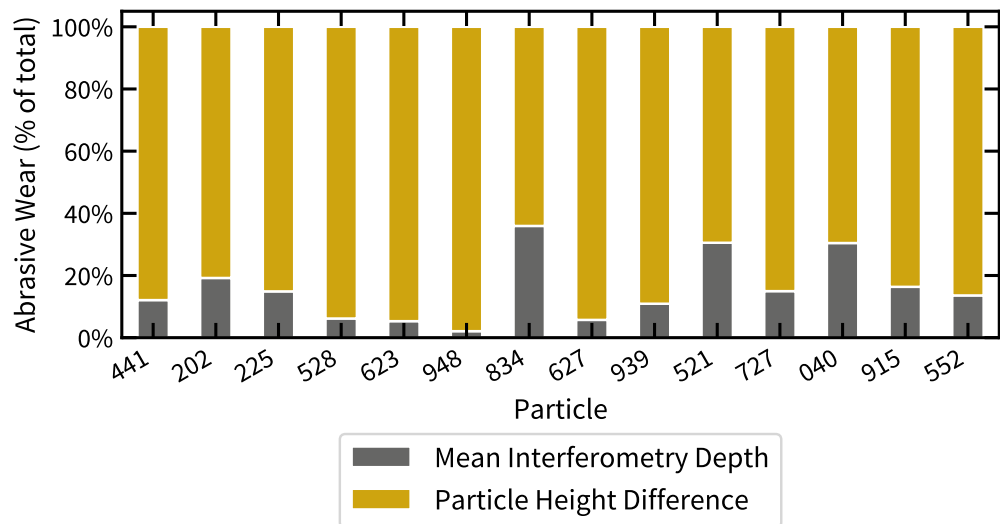


Figure 5.5: Stacked bar plot comparing the proportions of abrasive wear in terms of height lost from the tip of grains, and mean trough coordinate of interface surface

5.4. RESULTS AND DISCUSSION

Table 5.2: Comparison of change of height of particle and depth of interface after shearing, with vertical displacement at end of test

Test	Particle Height Difference (μm)	Depth of Interface Abrasion (μm)	Particle Interface Sum (μm)	Vertical Displacement (μm)
441	37.500	5.755	43.255	70.993
202	15.000	3.461	18.461	48.150
225	22.500	3.964	26.464	19.993
528	75.000	4.661	79.661	158.603
623	82.500	4.748	87.248	87.795
948	240.000	5.208	245.208	225.821
834	7.500	4.214	11.714	42.618
627	45.000	2.766	47.766	51.713
939	30.000	3.820	33.820	70.223
521	7.500	3.939	11.439	19.956
727	30.000	5.338	35.338	67.616
040	7.500	3.155	10.655	16.660
159	15.000	2.507	17.507	6.124
915	30.000	5.855	35.855	41.579
552	52.500	8.341	60.841	71.270

(Hutchings and Shipway, 2017) (see Equation 2.21). When this ratio exceeds a value of 1.2, the majority of abrasive wear is expected to occur to the softer of the two bodies if the normal load is greater than the indentation load for the softer surface. In the single-particle shear tests, a relative hardness value can be established. Invasive testing of the 304-grade stainless steel plates used in all of these tests showed an average hardness of 195 HV. Similar hardness testing of LBS grains gives a hardness of 500 HV (Sandeep and Senetakis, 2018). As such, the relative hardness in single-particle shear interface tests is 2.56, and the softer stainless steel is expected to see the majority of the abrasive wear.

Calculation of the volume loss between pre and post-test grain meshes was achieved using the python mesh processing package PyVista (Sullivan and Kaszynski, 2019). Each mesh object has a volume parameter, and by trimming the meshes to a common point the volume loss can be easily calculated. For the interface, the volume change is taken as the volume of the depression that

is created by the particle through continued shearing. In general, the theory of relative hardness holds and the majority of abrasive wear is attributed to the softer stainless steel interface. However, the proportions of volumetric abrasion are not dominated entirely by the interface. For convenience, the proportions of volumetric abrasive wear in the system are plotted in Figure 5.4. The underlying data is presented in Table 5.1. Some particles, notably particle 948, have an higher than usual proportion of abrasive wear to the particle. Visual inspection of these higher than expected particles validate the results, and it is seen that the particle tip fails more readily than the other grains. Whilst the observation that in the vast majority of cases more volumetric wear is experienced by the surface is somewhat trivial given the theory of relative hardness, the use of the modified particle virtualisation method allows for validation of this and allows for further investigation of the outliers, and investigation the how abrasive wear of sand particles governs interface shear response.

In the context of interface shearing, the total volume of abrasion to the interface is a misleading parameter to examine. Of course across a single shear cycle, the particle is interacting only with the surface material in the immediate contact area — the wear accumulated at other parts of the depression have no impact on the instantaneous stress ratio experienced between the grain and surface, at any specific point along the depression. It was shown in Chapter 4 that single-particle — stainless steel interfaces experience a steep increase, after a period of cycling, in the shear load transmitted across this contact area; an increase in stress ratio under constant normal load conditions. This increase in shear load must be governed by the particle and/or interface abrasion taking place. Another way to consider the quantity of abrasion (beyond simply volumetric wear) would be in terms of change in height or contact area. Figure 5.5 summarises the change in height and depth of both the LBS particles and stainless steel interface respectively, through comparison of the proportions of height change. The underlying data is presented in Table 5.2. Change in height of the grains is simply taken as the difference in pre-test maximum Z coordinate and post-test maximum Z coordinate. Change in depth of the interface is approximated as the mean minimum coordinate measured in the depression created by the particle during testing. As can be seen, the majority of vertical displacement (which can be estimated by summing particle height difference and interface depth) is comprised of particle height change at the tip of the grains. This, therefore, dominates the change in contact geometry of the system and hence the instantaneous stress ratio between the grain and the

surface. As such, although the concept of relative hardness remains true, it is not the key parameter that impacts the changing stress ratio response.

One difference between the tests presented in Figures 5.4 and 5.5, is the extent of shearing each test achieved, i.e. how long each test was allowed to run or the cumulative displacement of shear achieved in a test. Tests were deliberately run for different duration, as this permitted the particles and interfaces to be examined after different magnitudes of abrasive wear. Natural variation in the shear load during testing also impacts the magnitude of abrasive wear, as such, an appropriate parameter is needed to account for these differences.

5.4.2 Effect of Shearing Energy on Abrasion

Interface abrasion is a function of the total shear load transmitted at the interface, which was shown in Chapter 4 to change significantly during shear. Hence the number of cycles achieved is not a fair comparison between each test and the cumulative shearing energy, E , is used instead as previously defined in Chapter 4, Equation 4.2. Figure 5.6 presents the particle volume change data plotted against cumulative energy, where the point size is proportional to change in height of the grain. In general, volume change is proportional to cumulative shearing energy. With more shearing energy exerted, it is expected that there is more abrasion taking place as shown in Chapter 4. Some grains stand out against this trend, for example the point marked A in Figure 5.6 (particle 834, also identified earlier as an outlier in Figure 5.4), resulted in a much larger volume change in comparison to the other grains sheared to a similar energy. Another grain, marked B in Figure 5.6, also had a notably higher volume change than particles sheared to a similar energy, albeit at a lower magnitude than point A. This is due to variation in grain mineralogy, where brittle failure of the grain is able to occur at smaller stresses than average for this given fraction of sand.

Volume change is also correlated to height difference, although again, outliers are expected as different grain morphology's have different bias toward their volume. For example, an especially flat or flaky particle will lose more volume for a given height loss than a narrower or elongated one. This is shown by particles marked C and D in Figure 5.6, where particle D suffered less height change for an almost equal volume change, as a result of different tip shape.

The presented methodology paves the way for a range of shape related analysis, however some initial observations are made here. The abraded grains

— having a flattened edge in the post-test virtualization (Figure 5.3) — have an increased attack angle which is an influencing factor in interface behaviour. This finding shows that the shape of grains is transient even at relatively small numbers of shears. The theory of relative hardness does not consider the wear to the (harder) abrasive in the system and hence limits traditional application of 1D attack angle analysis of an abrasive. As the particle is subject to greater abrasive wear than relative hardness theories may suggest, the true 1D attack angle is a transient parameter during testing. In this case considering LBS grains, perhaps a more complex analysis considering the mineralogy of the grains is required.

5.4.3 Effect of particle surface area on abrasion

Using the displacement data collected by vertical tracking of the particle, in conjunction with the virtualised meshes, it is possible to analyse the abrasive system further with respect to the contact area between the grain and surface. A constant normal load is applied throughout the single-particle shear testing, therefore the contact area is the critical controlling parameter with regards to the stress condition in both the grain tip and structural interface. The contact area of particles has previously been established to have an effect on the internal stress and crushing behaviour of sands. After conducting tests of particle crushing with different coordination numbers Todisco et al. (2017) noted that the strength of LBS grains was influenced by local angularity. It was concluded that with low coordination numbers (small contact areas) fragments of the particles would break off, where as with high coordination numbers (where more of the grain surface is engaged) particles would fail catastrophically (i.e. global breakup of the particle) but at much higher stress levels. Image analysis shows breakage of the volume embedded in the interface, where contact area is highest.

Figure 5.7 displays the vertical displacement against cumulative shearing energy curves for a selection of grains in single particle shear. For reference to the proportions of abrasive wear (shown in Figure 5.5), the three digit test code is provided in the title of each plot. Through use of subpixel tracking, there is a clear trend of displacement throughout each test, with no sudden displacements. This accurate vertical tracking of the particle enables the calculation of particle surface area in contact with the interface.

The contact surface area also affects the abrasive wear of the interface. As previously stated abrasive wear is expected to occur to the softer of the two bodies

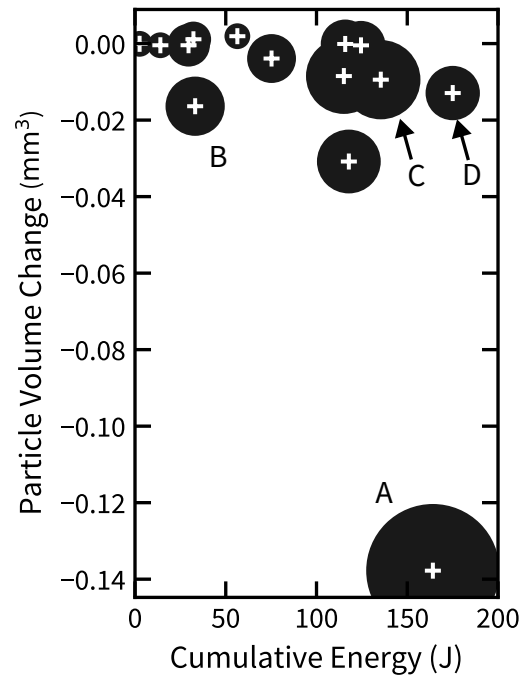


Figure 5.6: Plot of absolute volume change plotted against cumulative energy of shearing, point size represents change in height of grain

if the normal load is greater than the indentation load for the softer surface. To establish if this threshold has been met and to estimate the stress required, a series of normal embedment tests were carried out on two sand grains, normally loaded against a stainless steel surface. Vertical displacement tracking has been used to monitor the embedment of the particles as they were individually loaded from 1 N to 10 N. To validate the results, the same grain has been loaded twice on the same surface at a different point, and an alternate grain has also been examined. The curves of normal load against embedment depth are shown in Figure 5.8. At the maximum load of 10 N, there is still linearity. To estimate the minimum load at which embedment will commence, v_0 , linear best fit lines have been added to each series of data, and the x -intercept is found. The minimum embedment load v_0 values were found to be 1.75 N and 2.30 N for Particle A, and 0.97 N for Particle B. A qualitative analysis shows that particle B has a sharper/more narrow tip than that of particle A, and as such explains the lower load required, as contact stress is higher for any given load. Interestingly, there is a difference in the embedment load required for particle A when tested at a different point on the surface. This suggests that metallurgical differences in the surface can impact the behaviour of

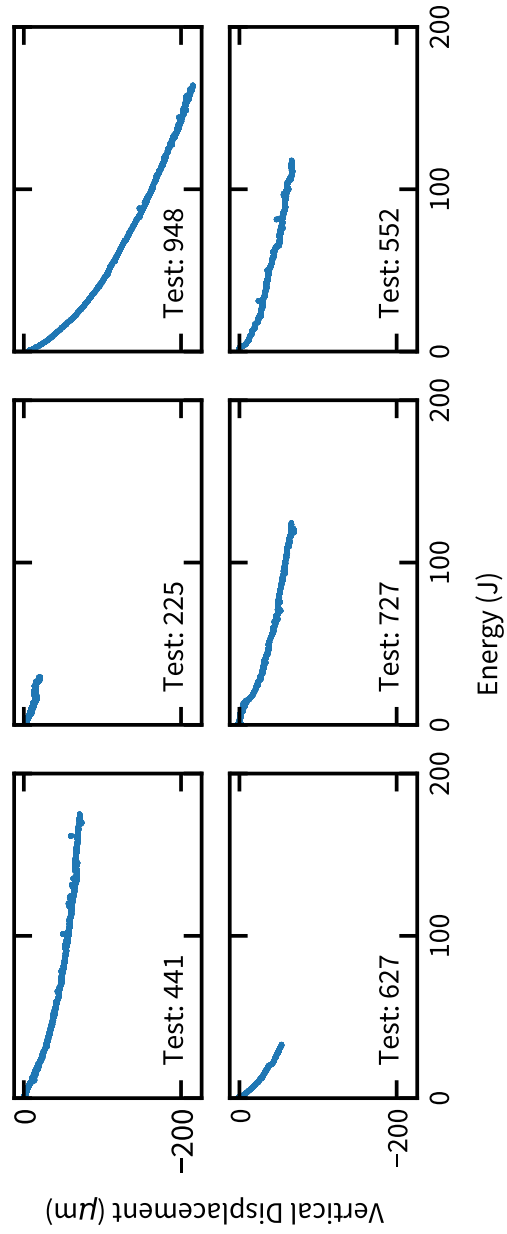


Figure 5.7: Comparison of cumulative shearing energy against vertical displacement

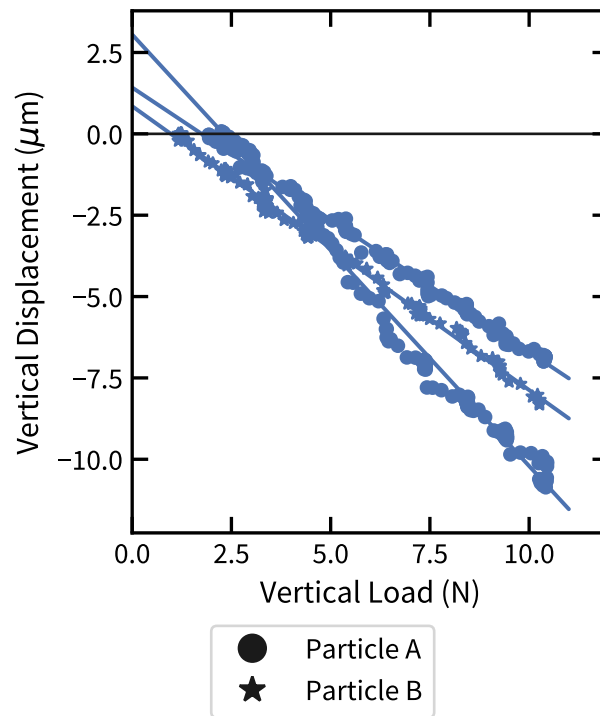


Figure 5.8: Normal embedment tests of sand grains

the grain-interface system.

With the transient shape of both the grains and the interface, the contact area is not constant across each 10 mm shear, or between successive cycles. Under normal loading, the particle contact area increases, as evidenced by Figure 5.8. The contact area under normal loading can be nominally estimated using the pre- and post-test meshes. Figures 5.9a and 5.9b display the pre- and post-test meshes respectively, with a highlighted area representing the nominal contact area under normal loading against a planar surface. This area is calculated from a sub-mesh centred at the tip of the grain (maximum Z coordinate). Any mesh face that is within a distance of 20 faces from the tip vertex point is included within the nominal contact area. The precise number of faces from the tip vertex to include is unknown and hence a nominal value of 20 has been chosen for this analysis. After shearing, the abraded grain, with a flatter top edge, has a larger contact area than the original mesh. During shearing, the contact area is expected to be larger due to the addition of faces in the X -direction (parallel to shear direction). In the middle of the shear stroke, faces on the particle outline when viewed perpendicular to the shear direction are in contact with the interface, in addition to those simply from normal (vertical) loading. Faces ‘in front’ or ‘behind’ this outline do have

5. QUANTIFYING INTERFACE ABRASION

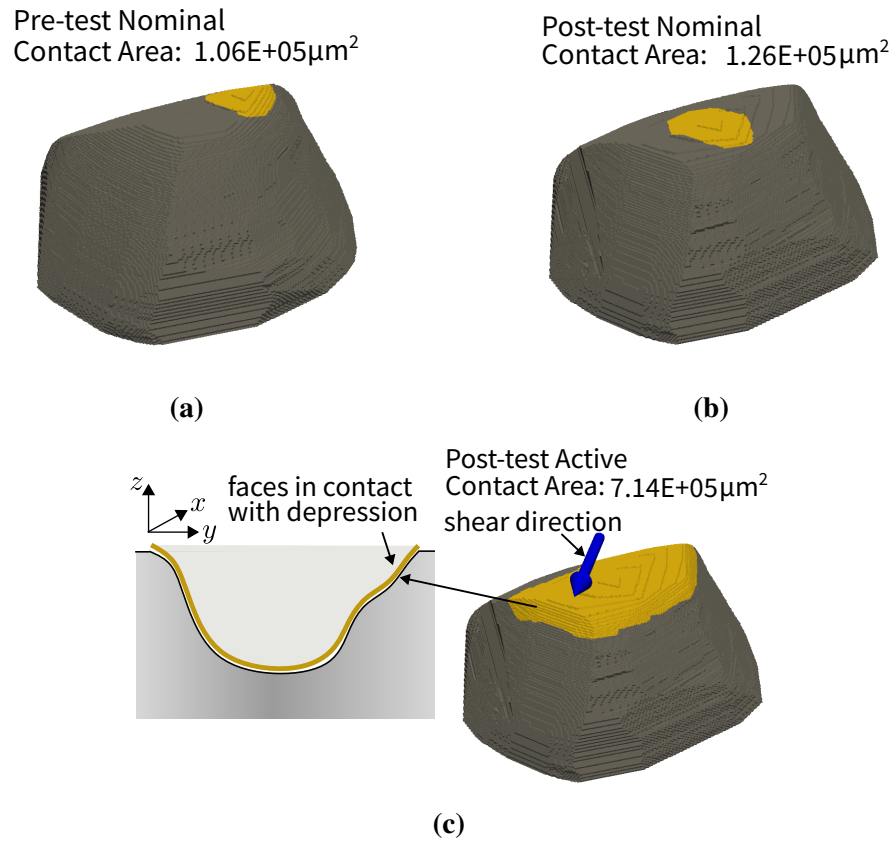


Figure 5.9: Change of nominal particle contact area pre- and post-test with increase in active area in contact during shear (3D meshes are shown viewing the tip of the grain): (a) Nominal contact area for a grain under normal load prior to shearing, (b) Nominal contact area for abraded grain under normal load after shearing, (c) Active contact area for abraded grain during shearing, schematic shows the particle outline and selection of outline faces

contact with the structural interface. This is demonstrated in a 2D schematic in Figure 5.9c. These active faces can be indexed on the surface of the 3D mesh produced by virtualisation and selected for subsequent analysis, shown in the 3D representation as highlighted faces adjacent to the structural surface. The contact outline on the surface of the particle, as shown, is a single line across the surface of the particle. This can exist in any orientation given the shear direction, and is calculated by using the angle detection process outlined in the above methodology. Figure 5.9c displays the faces on the post-test grain that are judged to be embedded in the interface *and* on the particle outline. Similarly to Figures 5.9a and 5.9b 20 rings around these faces are selected. This contact area can be referred to as the active area embedded in the interface. From the calculated contact areas

provided in Figure 5.9, the active contact area is more than double the pre-test nominal contact area. In addition, the depression within the structural interface increases the contact area of the post-test mesh by 70% (comparing post-test active to post-test nominal). Hence, the change in the particle is more significant in changing the contact area at the interface. Abrasive wear to the grains must therefore be considered when examining the variable shearing response in single particle shear.

With consistent and accurate tracking of particle vertical displacement, shown in Figure 5.7, this enhanced particle virtualisation methodology allows for calculation of the particle contact area at any point during shearing. It is therefore a powerful tool in developing further analysis on the behaviour of single-particle—interface shearing.

5.5 Conclusions

This study has set out a number of enhancements made to the particle virtualisation methodology presented by Nadimi and Fonseca (2017). As a result, is now possible to directly compare the meshes of grains prior to, and after shearing in single-particle interface shear. Furthermore, it is now possible to estimate the particle contact area at for single particle-interface shearing. An increase in resolution of the captured grains has also been achieved.

High resolution 3D meshes of 15 LBS grains have been captured before and after single-particle interface shear, and previously unattainable level of insight into the abrasive wear of (what are traditionally considered) ‘abrasive’ grains is now possible. This has permitted the quantification of volume loss from the abrasive grains, satisfying Objectives 3, 4 and 5 of this thesis. As would be predicted by relative hardness theory, larger volumes of abrasion occur to the softer structural interface than the harder grains. However, the contact area is a key controlling parameter on the shear response between the grain and the structural interface. It was found that the change in shape of the grain has a more significant impact on the contact area despite the lower volume change.

It is clear that aspects such as the variable contact area will play a role in the abrasive wear of the grains and structural interface, and hence the shear response. This chapter further develops the investigation into the role of abrasion in soil-surface interfaces, set out as Aim 2 of this thesis. Abrasive wear has been

shown to have more of an impact on the shear response than previously thought after Chapter 4. The investigation in this chapter has shown that the morphology of the grain tips changes by a ‘flattening’ the grain tips, and increase in the contact area of the grain with the interface. With the high resolution meshes captured by the enhanced particle virtualisation methodology, the complex geometry of the contact area between particle and structural interface can be examined further. This will be the focus of the next chapter, where the final Aim of this thesis will be addressed, an investigation into the role of particle shape in particle-interface shear.

5.6 Code Availability

The python code used to build the virtualised grains is freely available on the author’s github: github.com/guspettey.

Chapter 6

Characterising Frictional Response of Irregular Abrasive Grains with 3D Attack Angle

6.1 Notes

This chapter is a final draft of a paper submitted to *Géotechnique*, which is under review as of submission of this thesis. Where necessary, changes have been made to reflect the continuous narrative required for a thesis, mainly to the introduction which draws on the established literature review.

6.2 Introduction

As has been established in the Literature Review (Chapter 2), grain morphology is critical to the behaviour of granular bodies, however one all-encompassing parameter to characterise the shape of grains does not exist as physical interaction in different granular bodies is affected by three scales of particle shape (shown diagrammatically in Figure 2.1, derived from Barrett (1980)). The overall form of a particle will govern bulk volumetric response, angularity will be a factor in inter-particle friction, whilst roughness will impact the micro-mechanical interaction between grains. Attempts have been made to extend such analysis into three dimensions (Orosz et al., 2021; Zhao and Wang, 2016), with factors such as flatness, elongation, and compactness — all of which describe 3D form (shown in Figure 2.3). However, these parameters do not account for every facet

of 3D granular shape. Recent developments have been made, utilising detailed 3D meshes of objects, generated by methods such as X-Ray Tomography of granular triaxial samples (Fonseca et al., 2012; Medina and Jerves, 2018; Zhao and Wang, 2016) or photogrammetry (Angelidakis et al., 2021; Nadimi and Fonseca, 2017; Suhr et al., 2020), to analyse the shape of grains mathematically. It is clear that shape is an important factor not only in the behaviour of granular bodies but also in the shearing of soil-structure interfaces, where in Chapter 4 it was shown that abrasion caused a pronounced change in the stress ratio of the interface over thousands of cycles of shearing. Chapter 5 showed how the quantity of abrasion was variable between grains, in this chapter, a method to analyse the 3D contact geometry of these grains will be established (Objective 6). This will address the final Aim of the thesis, to analyse the role of particle shape in particle-interface shear (Aim 3).

Recalling from the Literature Review (Chapter 2), one parameter utilised in tribology to characterise shape in abrasive wear is the ‘attack angle’. The attack angle, α , is an established principle, and defines the angle from the particle centroid to the particle surface, where a smaller angle is more abrasive, as shown in the schematic in Figure 2.11. However, this traditional definition of the attack angle is based upon an idealised and simple conical abrasive, which, crucially, has a singular attack angle that does not vary as the abrasive penetrates the abraded surface. In fact, no suitable analysis exists for characterising the local roundness or angularity of an irregular particle, related to its abrasive effects. In addition, none of the shape parameters summarised in Figure 2.3 can be used as a substitute to quantify the abrasive characteristics. This is because, whilst the form parameters are applicable to irregular shapes, it is not specific enough to local angularity in 3D. This is a problem encountered by many studies, as Lindroos et al. (2015) noted, since modelling irregular abrasives used in experimental testing is challenging particularly due to the varying contact conditions. In that particular study, analysing cyclic direct shear behaviour of rock tips on high strength steels, a standard Rockwell-C diamond tip was substituted to simplify analysis.

Chapter 4 showed that cyclic shearing of sand against a metal interface, under constant normal load, resulted in a ‘stress-ratio elevation’, which is defined as a rapid increase in shear force over a set number of cycles, typically fifty. This was proven experimentally using both macroscopic (direct shear) and single-particle shear tests. Abrasive wear at the interface was found to be the cause of the elevation, although a specific parameter could not be identified as a trigger

for the rapid increase in shear force transmitted at the particle-interface contact. However, it was concluded in Chapter 4 that the shape of grains has a pronounced effect on the abrasive mechanisms and magnitude of abrasion that takes place between the relatively harder abrasive (particle) and the structural interface, simply demonstrated by the minimal abrasive effect of a spherical glass bead. Surface profiling showed that the interface was subject to plastic flow and cutting by the sand particles. In macroscopic samples the particles are free to rearrange and undergo crushing, and as such, there is no consistent set of particles interacting with the surface and hence no consistency to the abrasive wear experienced. It is therefore too complex to analyse the interactions occurring within the macroscopic samples at this time. Whereas, in single-particle tests, the particles were held in a fixed orientation, as such it is possible to capture detailed surface meshes of the particle contact region against the interface. This simplification enables an initial scoping investigation into shape effects on interfaces.

Chapter 5 presented a method to quantify the abrasive wear experienced by sand grains in single-particle shear, by capturing detailed 3D meshes of their morphology. Meshes are generated using particle virtualization, which is based on volume reconstruction of a number of 2D binary images, both before and after being subjected to shearing in a single-particle interface shear test, which subsequently allows for direct comparison and analysis of the shape of grains sheared. This methodology can be used to overcome the challenges encountered by studies such as Lindroos et al. (2015), enabling investigation of the shape of irregular grains. As such, a shape parameter which is responsible for the sudden elevation in stress ratio can be identified.

6.3 Methodology

6.3.1 Single-particle shear

Chapter 5 presented a quantitative analysis of the abrasion taking place in a series of 15 single-particle shear experiments, between a Fraction A Leighton Buzzard Sand (LBS) and a stainless steel interface, by considering only the 3D meshes created prior to and after shearing. Whereas in this study, load-displacement data collected during shearing of the 15 experiments will be analysed with respect to the shape of the irregular grains. These experiments are functionally identical to those presented by Chapter 4 — a schematic of the apparatus is shown in

Figure 4.1.

After establishing the utility of single-particle testing in developing a micromechanical understanding of soil-structure interfaces in Chapter 4, further development of the apparatus has taken place. Previously, normal load was applied through the use of masses placed above a linear bearing. To achieve finer control of the normal load application this has been modified, and a pneumatic actuator, controlled by a Proportional Integral Derivative (PID) programmed regulator, is used to hold a constant load through a 10 N capacity load cell. Shear load is measured by another 10 N capacity load cell.

Another adjustment made compared to the experiments in Chapter 4, a fixed normal load of 2 N was applied to all the grains across a shear cycle displacement of 20 mm during each of the tests. This was done in an effort to isolate the grain geometry and test duration as variable parameters, which are known from earlier testing to influence the abrasive wear of the interface. Other testing parameters such as grain type and interface material were considered as potential variables, but it was judged that the added complexity of the analysis would severely limit any conclusions that could be drawn. The particular normal load of 2 N was selected to approximate the upper bound load conditions experienced by grains in a macro-scale sample, which can be estimated by utilising other studies in literature. Hashemi and Heron (2019) provides a method for estimating the number of particle contacts on a sapphire glass surface, and hence estimation of the average force applied on 1D loaded grains. It was shown that Fraction A LBS has $0.80 \text{ contacts}/d_{50}^2$. The macroscopic samples tested, shown in Chapter 4, had a cross-sectional area of $80 \text{ mm} \times 80 \text{ mm}$. As such the number of contacts can be estimated as (with a $d_{50} = 1.5 \text{ mm}$) $0.8 \times 6400/d_{50}^2 = 2275$, with each grain having three points of contact (according to Hashemi and Heron (2019)). If a sample has a constant normal stress of 100 kPa, this results in 0.28 N per contact or approximately 0.9 N or 90 g for each grain. During cyclic soil-structure interface shearing, the force chains were disturbed upon shear reversal, identified with image analysis. Zhang and Evans (2018) presents a Discrete Element Method derived estimation of the probability of any given force chain carrying more load than the expected mean (load/contact number) in macroscopic interface shear. It is estimated that some force chains may be carrying up to $10\times$ more load than the expected mean. Hence the 0.9 N normal force calculated would be an underestimate of the true force applied to certain grains. Furthermore, as shown in Chapter 5, to overcome the minimum embedment load for a Fraction A LBS

grain on stainless steel, a load in excess of 1.5 N is required. Hence, considering the upper and lower bounds on the likely normal force carried by a typical grain, for this study a normal force, F_z , of 2 N was judged to be an appropriate load condition.

Another improvement over the previous body of single-particle experiments is the ability to accurately measure the vertical displacement of the particle, Δz , during shearing. This method was presented in Chapter 5, where high resolution images of the grain are taken during each individual shear displacement (two per cycle). A sub-pixel image tracking method is then implemented to return the net displacement of the grain since the beginning of the test. This enhancement also allowed for validation of the horizontal compliance of the system, which showed that the particle experienced negligible net movement in the horizontal (X) direction over the duration of the test. The connection between the grain, adhesive, bolt head, and load cell can as such be assumed as perfectly rigid for the magnitude of forces experienced during the test.

6.3.2 Particle Virtualisation and Mesh Processing

The particle virtualisation methodology presented in Chapter 5 has been used in this study to produce meshes — of resolution $1.5 \mu\text{m px}^{-1}$ — of each particle both prior-to and after shearing. The returned meshes are created using a Marching Cubes (MC) algorithm (Lewiner et al., 2003) on a voxelated structured grid of binary values (where the particle exists or not). Zhao and Wang (2016) notes for meshes created from volumetric data sets using the MC method — “the surface generated from MC have artificial stair-steps which makes a highly rough surface.” — as such, the meshes require a level of post-processing. Suhr et al. (2020) also faced a similar challenge with volumetric data of ballast particles collected using photogrammetry. As a result of the high resolution of their scans, surface roughness was present in the ballast meshes. The ‘collapse_short_edges’ (CSE) method in the python package PyMesh was used by Suhr et al. (2020) to smooth the meshes prior to analysis of their curvature and angularity. This eponymously named method will remove any face edge on the mesh shorter than a given threshold. The CSE method was used on the virtualised Fraction A LBS meshes with a threshold of $3\times$ the mean average edge length, which was judged to be appropriate to remove the artificial stair-steps from the surface. A sample of the processed meshes is shown in Figure 6.1. The intensity of the mesh denotes

the z -coordinate of the vertices. Higher values are closer to the tip of the grain, which was in contact with the stainless steel interface during shear.

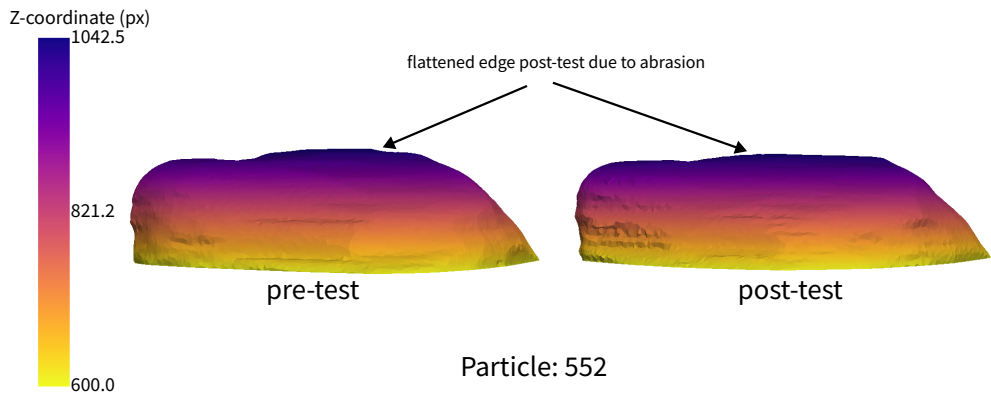


Figure 6.1: Virtualised meshes of sample particle pre- and post-test in single-particle interface shear. Meshes have been processed with ‘collapse_short_edges’ using a threshold of $3\times$ the mean average edge length

6.4 Shape Tensor Analysis

As mentioned in the introduction, some established methods exist for characterising the shape of irregular particles, namely the form parameters shown in Figure 2.3, established by Orosz et al. (2021). Due to the versatility of the methods presented for virtualising grains prior to and after shearing — presented in Chapter 5 — it is possible to calculate the form parameters for the volume of each grain that would be embedded in the interface at the end of each test, using the surface orientation tensor. To achieve this an assumption is made that no abrasive wear is suffered by the grains. As such, the embedded volume is found by taking the volume of mesh that lies within the maximum vertical displacement value from the tip of the pre-test mesh. For example if a grain had a maximum vertical displacement of $50\ \mu\text{m}$, the volume of mesh within $50\ \mu\text{m}$ of the tip of the pre-test mesh would be taken as the embedded volume. Figure 6.2 shows a Ternary plot of the three form parameters: compactness, flakiness, and elongation (sometimes referred to as rodness). These form parameters struggle to capture the angularity of the grains, and are clearly biased towards flakiness, due to the ‘flat’ nature of the embedded region. This demonstrates the limitation of the surface orientation tensor method to be used for comparing local angularity. It is only this embedded volume that is ever in contact with the interface, yet the form parameters are heavily biased

towards flakiness. Therefore, another method is required to quantify the angularity of the grains.

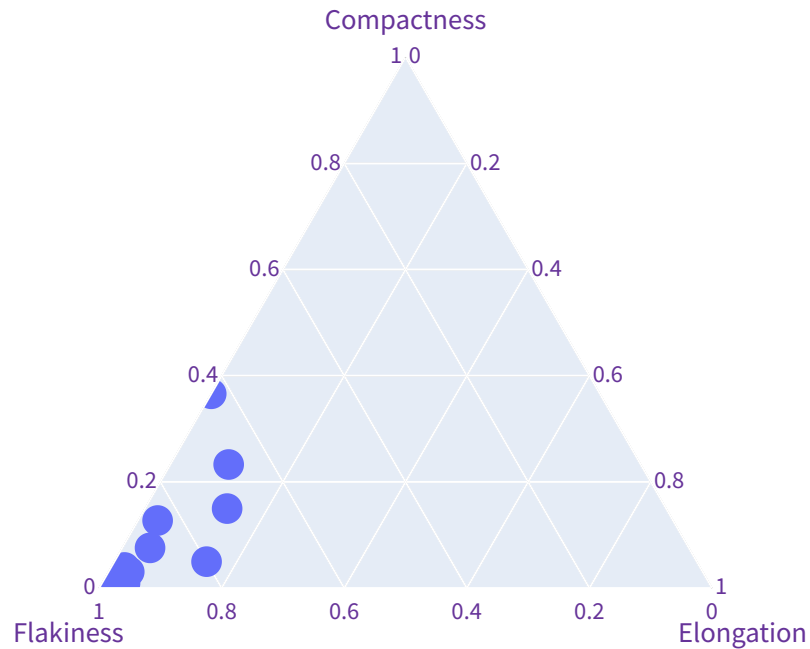


Figure 6.2: Ternary plot of the form parameters for the volume of particle embedded in the surface, for all tests

6.5 Attack Angle Analysis

6.5.1 Characterising Abrasive Wear to Irregular Grains

Before examining the frictional response of the irregular grains during single-particle interface shearing, it is useful to first consider the nature of damage experienced by the particles during shearing. This will subsequently inform assumptions which are necessary to establish the relationship between the damage to the particles and the frictional response. The abrasive wear suffered by the grain can be seen in Figure 6.1, with the tip of the post-test grain having been flattened. A subjective analysis of all of the post-test meshes shows this flattening of the tip, however a quantitative analysis can be carried out. Each mesh is comprised of a number of triangular faces. The meshes have a number of attributes accessible,

including, but not limited to, the face area and face normal attributes. The face normal attribute is a (n_faces, 3) shaped array of $x\hat{i}, y\hat{j}, z\hat{k}$ vector components, denoting the 3D direction each face is pointing. The face normal array can be used to analyse local changes in shape or for comparison against any given vector. Specific regions of the grains can be selected for deeper analysis.

To investigate the ‘flatness’ of the grain tips, the face normal vectors at the grain tips can be compared to a unit vector in the z -direction (0, 0, 1) (these face normals would point directly up in Figure 6.1). To compare any two vectors, ‘cosine similarity’ is used. The cosine similarity returns a score from -1 to 1 for how similar two vectors are, where 1 is identical and -1 is opposing (Virtanen et al., 2020). Cosine similarity, K , between two vectors, A and B , is calculated as:

$$K = 1 - \frac{A \cdot B}{\|A\| \times \|B\|} \quad (6.1)$$

Figure 6.3 shows violin plots of the cosine similarity, of all faces within 3 pixels of the particle tip, between the face normal and z normal vector. The violin plot displays the distribution and density of a series of data, and is marked with the mean of its distribution. Each violin plot is labelled by a unique numeric key that is used as reference for the different tests. In the violin plot, the mean similarity of faces is marked, and in excess of 0.9 for all grains, with a majority in excess of 0.98. Grain 521 stands out as an outlier, which is a result of the length of shearing experienced. The duration of shearing was not consistent across all tests, in order to analyse the abrasive wear at different amounts of shearing energy. Grain 521 was sheared through 350 cycles, the smallest amount of cycles of all tests. As such, the ‘flattening’ effect was minimal, compared to other tests which had up to 5000 cycles. Therefore, a fixed range of 3 pixels in the z -direction selects faces that have not been abraded (flattened), and which therefore have less similarity to the z normal vector.

Chapter 5 showed in single-particle shearing of a Fraction A LBS on a stainless steel interface, that whilst the total volume of abrasive wear in the system was dominated by volume loss of the stainless steel interface, in terms of height loss, the particle abrasion was dominant (since volume is calculated across the entire 10 mm abrasion). Hence it follows, that the vertical displacement measured during shearing is dominated by height loss at the tip of the particle. For example, in test 552, the post-test particle was estimated as $35 \mu\text{m}$ shorter than the pre-test particle. Surface profiling through white-light interferometry showed the depth of the abraded region to be $8.2 \mu\text{m}$. Independent from these methods, vertical

6.5. ATTACK ANGLE ANALYSIS

displacement tracking displayed a maximum depth of $47.5\ \mu\text{m}$. The sum of particle height difference and surface depth should, in theory, equal the maximum vertical displacement value, however some error is expected in both the height loss calculation and surface depth, which is an average across the entire length of abrasion. Since the surface depth is much smaller than the height change of the particle, it is assumed, for the subsequent analysis presented in this chapter, that the vertical displacement measurement can approximate the level of particle height loss at any point during the test.

In summary, it is reasonable to assume that the abrasive wear of grains increases the surface area at the grain tip that is ‘flat’ or similar to the z normal vector, as shown by Figure 6.3. Due to the change in vertical displacement being dominated by particle height loss, an estimate of the abraded particle shape can be established by taking an xy plane across the grain at the vertical displacement value for a given cycle. The faces of the mesh adjacent to and above this plane, are therefore taken to be the faces in contact with the surface and involved in abrasive wear.

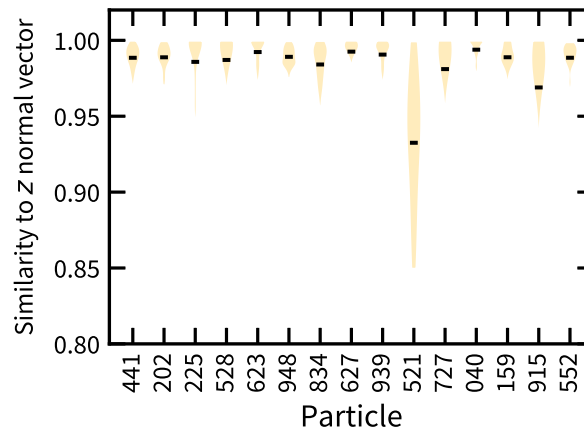


Figure 6.3: Violin plot showing the similarity distribution of face normals to z -normal vector at the tip of post-test grains

Throughout testing, the vertical displacement, Δz , of the particle was measured using the image tracking method described in Chapter 5. The relationship of vertical displacement, Δz , and stress ratio, μ , is shown in Figure 6.4, where both parameters are plotted against cumulative shearing energy, E . As previously used in Chapter 4, the stress ratio is simply calculated as the average shear load per cycle divided by the average normal load per cycle. An appropriate rolling mean of 75 cycles across all of the datasets is taken for better clarity

when comparing the trends between tests. Each of the grains was sheared to a different level of cumulative shearing energy. As established in Chapter 4 the cumulative shearing energy is used to offer better comparison between tests where abrasive wear considerably changes the stress transfer at the interface and is defined in Equation 4.2. Similarly to the single-particle tests in Chapter 4, a stress ratio elevation occurs for LBS grains sheared against an equivalently harder stainless steel interface. This is manifested in a rapid increase in the stress ratio from an initially sliding mechanism with minimal frictional response ($\mu \approx 0.2$) to a mechanism of plastic deformation with a much greater frictional response ($\mu \approx 0.7$). The high level of friction after elevation is dominated by cutting wear. This is confirmed on calculation of the cutting-plasticity ratio, η , which was found to be a mean of 0.87 ($\eta = 1$ would be purely cutting wear) across all tests. A high level of cutting wear is expected in two-body abrasion (where the particle contact has no degree of freedom), and also is known to have a high frictional effect (Gates (1998); Hutchings and Shipway (2017)). The grains do not have a consistent energy at which a stress ratio elevation occurs, grain 627 is almost immediate, after 1.1 J of shearing energy, whereas grain 915 required up to 25 J (approximately 2750 shear cycles) before the elevation. The rate of vertical displacement increase is, as expected, variable, and is dependent on the grain morphology. The full dataset of vertical displacement and stress ratio is shown in Figure B.2.

6.5.2 3D Attack Angle

Traditional analysis of abrasive systems has used a 2D attack angle, as shown in Figure 2.11. Clearly, due to the irregular geometry of the LBS grain, drawing an appropriate 2D attack angle is challenging since the particle is not a constant shape with depth into the y or z -axes. A 3D attack angle is more appropriate, and is able to be created by leveraging the benefits of the particle virtualisation methodology, but requires some assumptions to be made.

To build an understanding, first consider Figure 6.6a, which demonstrates the principal of how an attack angle could be generated for an irregular particle at two different levels of abrasion. To create the attack angle, a tangent is drawn from the contact point, through the faces of the particle that are within a depth d from the contact point. In practical terms, this creates an average attack angle of the faces inside the depth d , that are assumed to be contributing to the frictional

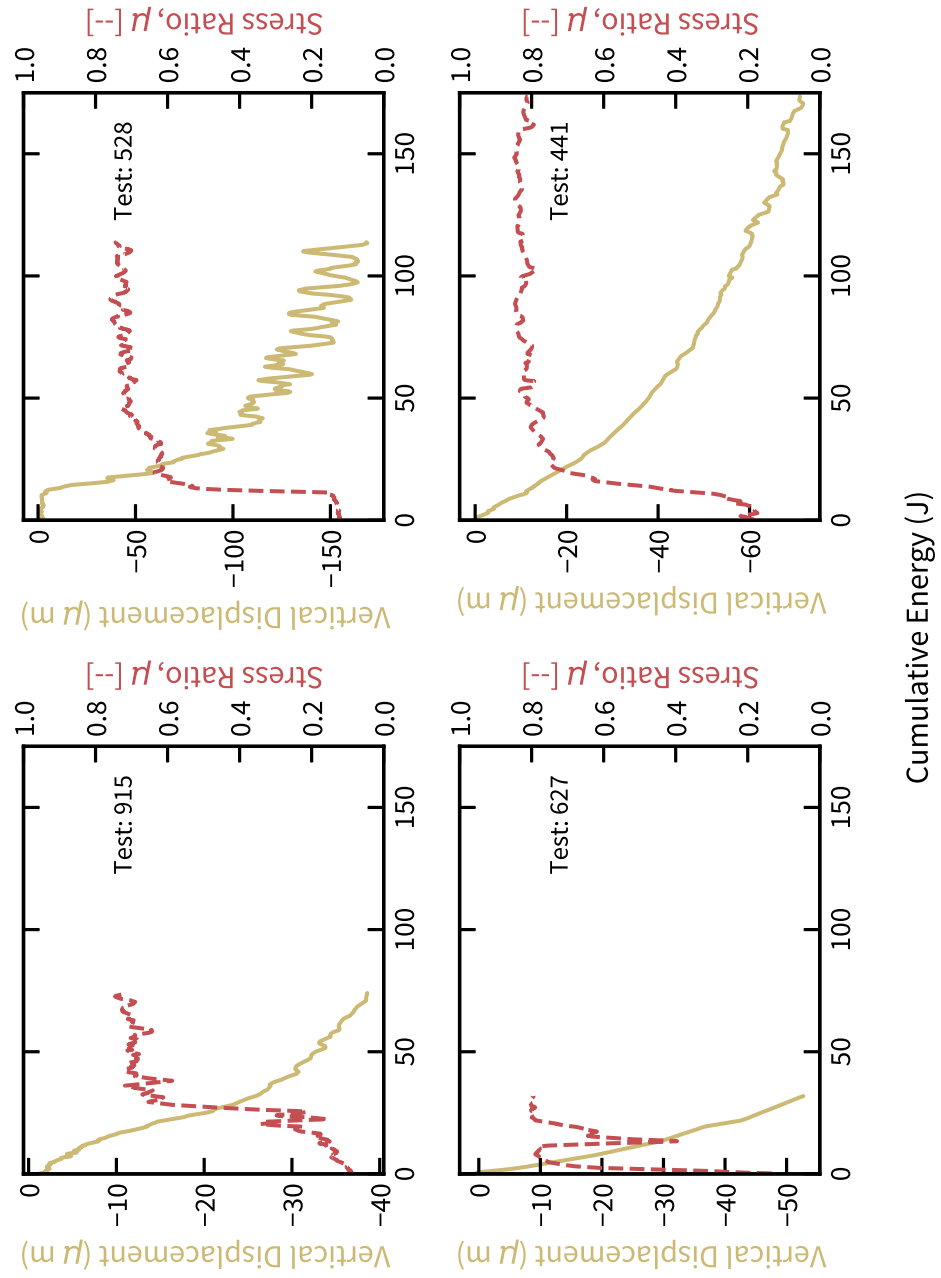


Figure 6.4: Plots of vertical displacement, Δz , and stress ratio, μ , against cumulative shearing energy

contact during shearing. The choice of the depth, d , is subjective, and will change the resulting attack angle, α , where a larger range is less susceptible to error, but has less relevancy to the contact mechanics of the particle and surface. It should, however, be a consistent value to enable direct comparison between test points. As such, the depth, d , is identical in the initial and mid-test schematics. A value of d that is too small will be too noisy and subject to bias from individual faces. Equally, a value of d that is too high will include a region of the particle that is not relevant the shear behaviour. Therefore, the specific value of the depth, d , is decided to optimise the analysis.

Figure 6.6b shows how the above analysis is extended into 3D, using a sphere as an example. The attack angle of each face, α_{face} , can be established relative to the flat plane drawn across the sphere, which represents the depth from the grain tip to the contact point. In this analysis, as concluded in the previous section, this depth will be taken as the measured vertical displacement. As such, the translucent area represents the volume of particle which is assumed to have been removed by abrasive wear. Face attack angles are calculated on every face in the highlighted region, where the depth of this region is analogous to the depth, d , in Figure 6.6a. For the analysis on the grains in this study, a depth of 4 px is taken, equivalent to 6 μm . The angle, α_{face} , can be directly calculated using the face normal vector, N , against the z -normal vector, P , Therefore, α_{face} is calculated as:

$$\alpha_{\text{face}} = \sin^{-1} \left(\frac{|N \cdot P|}{\|N\|} \right) \quad (6.2)$$

The 3D attack angle, α_{3D} , is taken as the mean of all individual face attack angles inside of the region of interest (the highlighted region). However, a simple mean would be identical regardless of the experienced shear direction. Therefore, a weighting, γ , must be introduced to account for the specific direction of shearing in each test, relative to the particle. Chapter 5, a method for calculating the orientation of grains during shearing allows for the shear direction to be represented as a vector. Therefore, the cosine similarity (Equation 6.1) can be used to weight each face attack angle by its contribution to shear resistance. The basis for this is that faces perpendicular to the shear direction vector provide a minimal contribution to the shear resistance, and as such have less relevance to the frictional response. Whereas, faces parallel to the shear direction vector will have a significant contribution to the shear resistance. To demonstrate this, the intensity value of the faces in Figure 6.6b represents the cosine similarity to the displayed shear vector. In practice, the shear vector is not uni-directional, as shearing is

cyclic in single-particle interface shear. As such, the absolute value of cosine similarity is taken when weighting faces, giving a range of 0 to 1, to create an average attack angle that is representative of the bi-directional shearing vector. Furthermore, an area weighting must be applied to the face attack angle, as the meshes do not have a uniform face size. This is simply taken as the face area divided by sum of face areas in the region of interest. The particle face contact area has been directly calculated from the mesh properties, and is displayed in Figure 6.5 compared to the stress ratio, μ , against cumulative shearing energy. As expected, the contact area increases as shearing continues, as the particle tip is flattened and more faces are in contact with the surface. The full dataset of contact area and stress ratio is shown in Figure B.3.

Given the above, the 3D attack angle, α_{3D} , relative to a shear direction vector, V , is calculated as:

$$\alpha_{3D} = \langle \gamma \alpha_{\text{face}} \rangle \quad (6.3)$$

where,

$$\gamma = \frac{A_{\text{face}}}{\sum A_{\text{face}}} K_V N_{\text{face}}$$

Applying the above to the example of a sphere with radius 50 px, such as in Figure 6.6b, the mean face attack angles can be directly calculated and are shown in Figure 6.7. As shown, the mean face attack angle at the particle tip (depth = 0) is 90° , and at the centreline (depth = 50) are 0° , these are expected values for a sphere, validating the method of calculation for face attack angle.

The 3D attack angle, α_{3D} can be calculated on any irregular meshed object with face area and face normal attributes. This analysis can therefore support further investigation of the abrasive wear caused by irregular grains.

6.5.3 Frictional Response of 3D Attack Angle

Having established the calculation method of 3D attack angle, and the assumptions required to compute it — namely that a flat surface can be taken across the particle at a depth equal to the vertical displacement, to estimate the level of abrasion of the particle in any given cycle — the analysis can be carried out on all 15 virtualised particles and shear datasets. The virtualised particles and shear datasets have been established independently of each other (i.e. one via imagery and one via traditional instrumentation).

Figure 6.8 displays four plots of 3D attack angle, α_{3D} , and stress ratio, μ , against cumulative shearing energy for four representative separate grains (tests

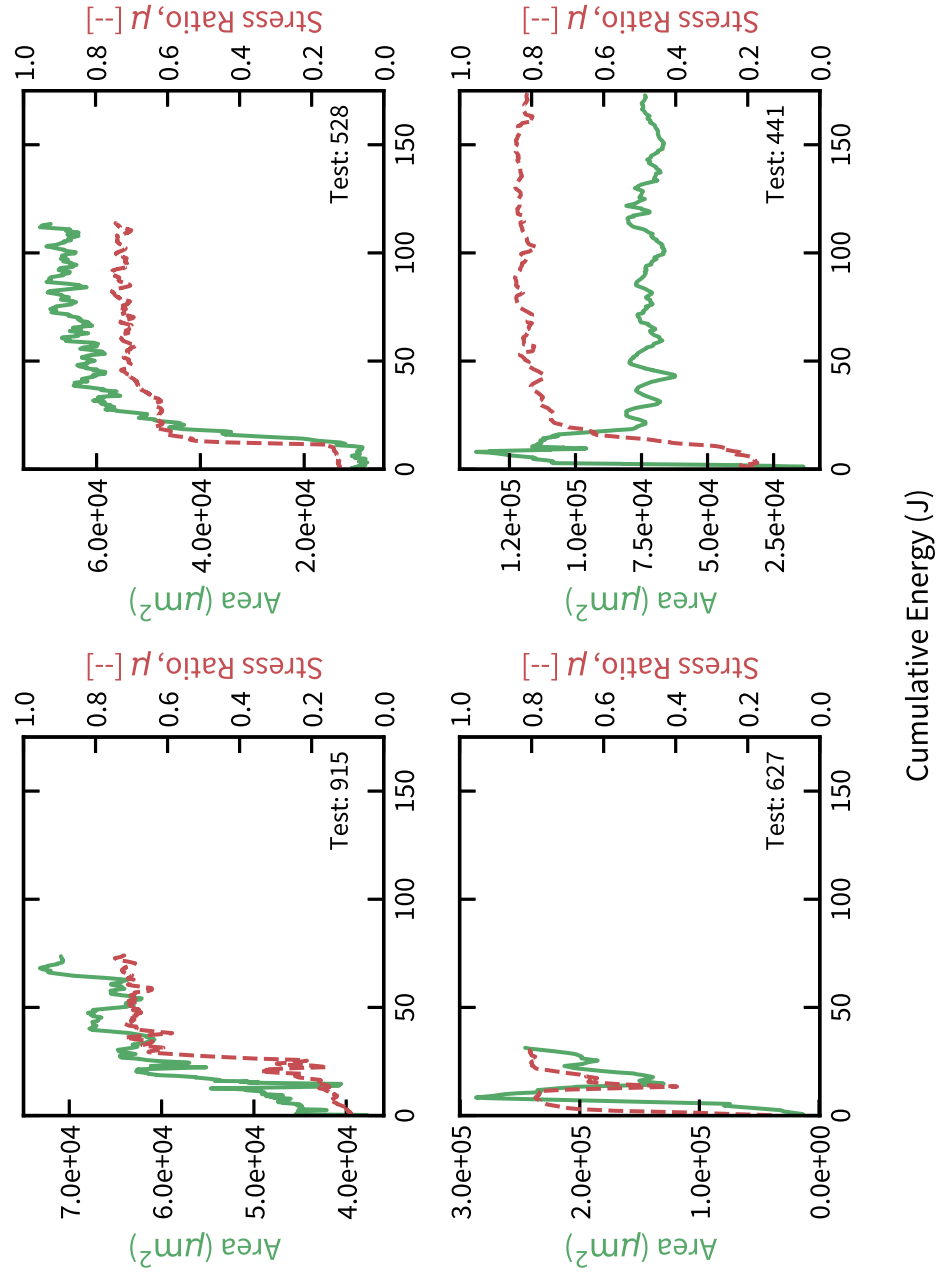


Figure 6.5: Plots of contact area, ΣA , and stress ratio, μ , against cumulative shearing energy

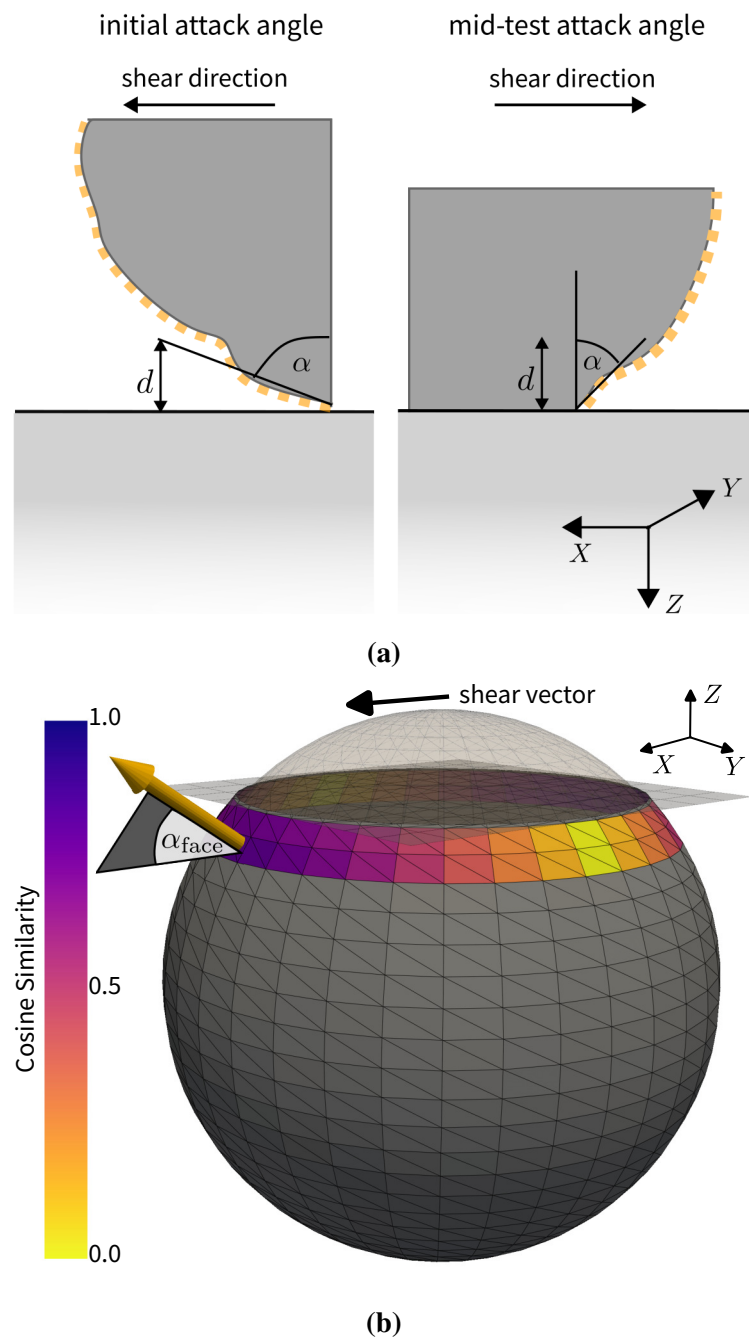


Figure 6.6: Development of 3D attack angle: (a) Example of 2D attack angle α estimation for an irregular geometry at increasing levels of embedment z , (b) Example of weighted face attack angle calculation on a sphere

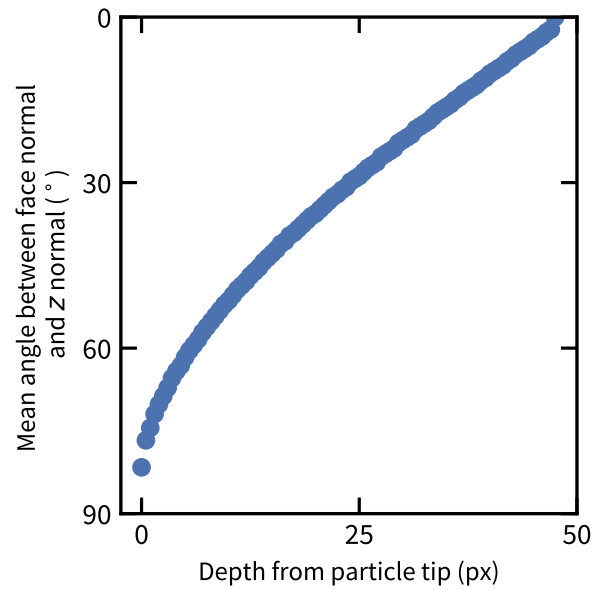


Figure 6.7: Mean angle of face attack angles to xy plane for a sphere with radius 50 px

915, 528, 627 and 441). The 3D attack angle has been calculated on the pre-test particle meshes.

The frictional response of the tests shows that there must be some variable trigger which causes the rapid increase in shear force transmitted at the interface. Until now, the specific trigger for this rapid increase in horizontal stress has been unclear. The experimental method used in this study was created to minimise the variability between tests, leaving only the grain shape and mineralogy (inherent variability between grains) as variables. The plots produced reveal a clear link between the grain-specific 3D attack angle, α_{3D} , and the stress ratio response. It is evident that a steep decrease in attack angle occurs alongside the stress ratio elevation. Indeed, even a momentary drop in stress ratio in test 627 is also accompanied by a drop in attack angle, before increasing again with stress ratio, showing a clear correlation. An decrease in attack angle — caused predominately by the abrasive wear of sand grains, in addition to embedment and cutting wear of the surface — causes the increase in friction between a single LBS grain and stainless steel interface. Strong attack angles are associated with high levels of shear resistance, caused by cutting wear (Hutchings and Shipway, 2017). Note these two parameters are computed from two entirely independent datasets — one from imagery and one from traditional instrumentation. As such the clear correlation between them is not a trivial link resulting from an error in experimental

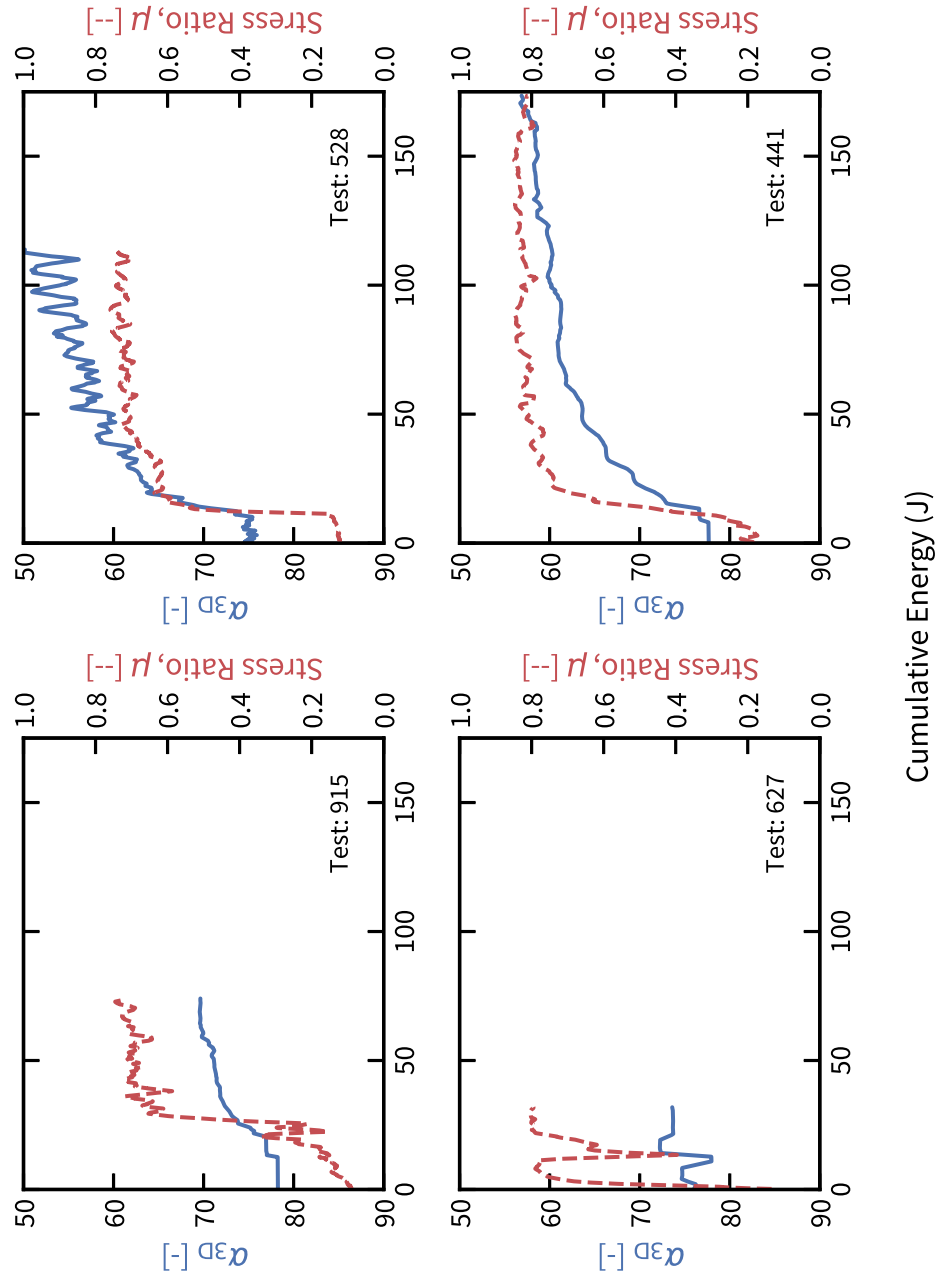


Figure 6.8: Plots of 3D attack angle, α_{3D} , and stress ratio, μ , against cumulative shearing energy

processing.

Each of the tests had a similar starting 3D attack angle of 75° to 80°. It is expected that grains which are of the same fraction, and characterised as ‘rounded’, would have a similar starting value of attack angle at the grain tip, although there does not seem to be a critical angle at which stress ratio elevation begins. Naturally, the peak attack angles are not similar between tests, due to the inherent variability of grain geometry with depth into the particle. The contact area between the particle and surface has been shown to vary greatly between the start and end of shearing, see Figure 5.9c. Direct comparison of the frictional response and attack angle between particles is challenging as a result. Abrasive wear, which provides the majority of shear resistance at the single-particle—steel interface, is a function of contact stress and as such the area of contact. For example, as demonstrated in Chapter 5, the normal load required to embed two LBS grains into a stainless steel surface is different because of the varying contact area, this is why hardness is measured with a regular pyramidal indenter. Therefore, the stress level needed to trigger the stress ratio elevation, caused by abrasive wear, will also be dependent on contact area and as such the specific angles of the particles cannot be directly compared.

6.6 Conclusions

The local angularity or roundness of irregular grains is a crucial component of the frictional response during interface shearing. The grains form an ‘attack angle’ relative to the surface, which is a standard method of characterising abrasive wear in the discipline of tribology. However previously this analysis has only been conducted in 2D on regular shapes such as conical tips. This study presents a method to calculate the attack angle of irregular geometries by taking into account their 3D shape. This attack angle, α_{3D} , can be calculated on any meshed object. The 3D attack angle is shown to have a strong correlation with the stress ratio mobilised when shearing Leighton Buzzard Sand particles against a stainless steel interface. A stress ratio elevation occurs in all tests, from an initially low stress ratio of 0.2, to approximately 0.7 — this elevation tallies with when the attack angle of the particle begins to reduce. Reduced attack angles cause the abrasive wear mode to be dominated by cutting abrasion, which is known to have a high frictional effect. Indeed, the experiments presented in this study had a high level of cutting abrasion as measured by the cutting-plasticity ratio. Therefore

6.6. CONCLUSIONS

it is concluded that the decrease in attack angle, caused by a flattening of the particle tips by abrasive wear, causes an increase in the level of cutting abrasion on the surface, which is responsible for the stress ratio elevation. This study neatly concludes the experimental work of this thesis, by applying fundamental mathematical analysis to the experimental data, to provide a new insight into the frictional response of granular materials. As such, this study has satisfied the last of the aims of this thesis, to analyse the role of particle shape in particle-interface shear.

Part III

Conclusions and Recommendations

Chapter 7

Conclusions and Recommendations

7.1 Review of Findings

This section will review the findings of each chapter of investigation conducted in this thesis, with reference to the aims and objectives of this thesis, as defined in Chapter 3.

7.1.1 Chapter 4: The role of abrasion in cyclically sheared soil-structure interfaces

The first investigation of this thesis set out to satisfy Aim 1 and Aim 2 (defined initially in the Aims and Objectives in Chapter 3), to investigate the link between macroscopic interface behaviour and particle scale interface behaviour and investigate the role of abrasion at soil-structure interfaces. Using a novel experimental apparatus to conduct single-particle interface shear tests, the link between macroscopic interface behaviour and particle scale interface behaviour was established. This link was established over much larger numbers of cycles than previously conducted, the existing level of ‘long-term’ investigation has been limited to less than 100 cycles of shearing, which is insufficient to capture the full range of behaviour that can be expected from a soil-structure interface. It was identified that after continued shearing under a constant normal load boundary condition, a sudden increase in stress transfer at the interface occurs, referred to as a stress ratio elevation, in both macroscopic and single-particle tests. This stress ratio elevation was not previously formalised in literature, as the majority of research into cyclical interface shear behaviour was established under a constant stiffness boundary condition (Section 2.3.2). Therefore it is

concluded that the investigation into the link between macroscopic and particle scale interface behaviour has been successful

It is evident, on the basis of the similarity between single-particle and macroscopic stress ratio response — presented in Section 4.7 — that the abrasive wear caused by individual particles is the primary mechanism for the stress ratio elevation in macroscopic interface shear. This is because the abrasive wear caused by individual particles is the only mechanism that is present in both single-particle and macroscopic interface shear. However, the complexity of the abrasive response, and the lack of specificity in load condition in single-particle testing, means the investigation into the role of abrasion in interface behaviour required further development.

7.1.2 Chapter 5: Quantifying Interface Abrasion with Particle Virtualization

This Chapter sought to continue the investigation into the role of abrasion at soil-structure interfaces, satisfying Aim 2 of this thesis. To achieve this, a particle virtualisation method was developed to capture high resolution 3D meshes of the grains tested in single-particle shearing. As such, any abrasive wear suffered by the grains could be quantified, and compared to the abrasive wear suffered by the structural interface, which is quantified using the method established in Chapter 4 of white light interferometry. In a significant development over the initial study that presented the particle virtualisation methodology, the new method presented in Chapter 5 enables the direct comparison of the particle geometry before and after shearing in single-particle interface shear, on an identical coordinate system. This has, initially, enabled the quantification of the abrasive wear of the grain in terms of both volume and height. The long established principal of relative hardness in abrasion has been verified in terms of volume of wear, but the finding of a more significant change in contact area due to the change in shape of the grain is a novel finding and prompts a conclusion that it is perhaps this variable contact area that causes the stress ratio elevation. Abrasive wear theory is not well suited to irregular grain geometry, and this study has demonstrated the importance of considering the change in shape of the grain — at the angularity scale from Figure 2.1 — when considering the abrasive wear of a grain. The established principal of relative hardness does not account for any wear to the harder abrasive particle. In reality this is physically impossible, some wear will of course occur —

even diamond tip abrasives eventually need replacing — however the extent of this wear is significant enough to fundamentally influence the wear mode of the surface by the particles. This is a significant finding, and one that has not been previously reported in the literature, which has mainly considered a change in roughness through the breakage of asperities.

7.1.3 Chapter 6: Characterising Frictional Response of Irregular Abrasive Grains with 3D Attack Angle

The final investigation of this thesis sought to satisfy Aim 3, to analyse the role of particle shape in particle-interface shear. The method developed in Chapter 5 to capture high resolution 3D meshes of the grains tested in single-particle shearing was further developed to enable the analysis of the 3D contact geometry of a particle against a surface in particle-interface shear. By quantitatively examining the nature of wear suffered by the grains, it was shown that the grains tips become flatter, with a larger contact area that points towards the interface. Using this information, an assumption can be made about the wear mode of the grain, throughout the shearing process. It was assumed that the vertical displacement value at any point in the shearing process, would be dominated by height loss at the tip of the grain, and the contact geometry could be found by taking this vertical displacement as a depth into the grain. As such, a new parameter, the 3D attack angle, α_{3D} , was defined, which is the angle between the edge of the particle contact and the surface, which crucially, is relative to the direction of shear. This accounts for irregular grain geometry, and is more applicable to the analysis of the particle-surface interface than the established methods of shape analysis, which either take a simple 2D cross section, or consider the particle as a whole. The 3D attack angle is shown to be a key factor in the frictional response of the particle-surface interface, and a sudden fall in attack angle occurs at the same point as the stress ratio elevation, initially identified in Chapter 4. It is therefore concluded that the decrease in attack angle during shearing, as the particle is driven into the surface, causes an increase in the level of cutting abrasion on the surface, which is responsible for the stress ratio elevation. Crucially, these findings have been made by curating two entirely independent datasets, one from traditional instrumentation and one from image analysis, which have been shown to be in agreement with each other.

7.2 Application of Findings

This thesis has sought to investigate the micromechanics of soil-structure interface behaviour, and whilst this is a fundamental investigation, not using experimental conditions directly linked to real world applications, the findings of this thesis can be broadly applied to the design considerations of soil-structure interfaces. One significant finding is that of the extent to which abrasive wear affects the long-term behaviour of soil-structure interfaces. At present, the abrasive wear of interfaces is not something that has been considered in design, and the resulting stress ratio elevation will significantly impact the load conditions of interfaces throughout their lifespan. Two examples of this are presented below, to demonstrate the application of the findings of this thesis to real world applications.

Firstly, take, for example, the case of a steel monopiled foundation embedded in sand. Cyclical lateral loading ($\pm 1^\circ$) experienced by a 6 m monopile could cause over 100 mm of displacement at the sand-steel interface, repeated throughout its lifespan, which can cause abrasive wear, increasing roughness and interface friction. At present the decommissioning of these monopiles is achieved by simply cutting the monopile at the seabed, and leaving the foundation in place. However, with the insights gained regarding the stress ratio elevation, a model to estimate the stress ratio on a monopile after large amounts of continued cycling can be developed, potentially enabling the calculation of the pull out force required which could enable recycling of the foundation. Again, with an appreciation for the design challenges of soil-structure interfaces, the length of experimentation presented in this thesis is more appropriate for the design lifespans of interfaces in reality.

Secondly, consider a shallow pipeline, buried in sand. The pipeline is subject to cyclical loading, due to thermal expansion and contraction, which causes the pipeline shear against the sand. With repeated shearing, the pipeline will be subject to abrasive wear, which will increase the roughness of the pipeline, and increase the frictional resistance of the pipeline. With greater shear loads applied to the pipeline, without adequate expansion joints, the pipeline may be subject to buckling. The findings of this thesis can be applied to the design of the pipeline, to estimate the increase in frictional resistance due to abrasive wear. A refined design could account for this, potentially with a sacrificial layer of material or harder coating, to reduce the abrasive wear of the pipeline.

7.3 Future Work

Whilst this work has uncovered new insights into the micromechanical processes at the particle-surface interface, there is still much to be done to fully understand the macroscopic behaviour of soil-structure interfaces. One of the key limitations of the single-particle testing in this study is the absence of crushed particles in the particle-surface interface, that are otherwise generated in the macroscopic interface. It was concluded in Chapter 4 that the crushed particles, generated by stress concentrations at the macroscopic interface, are responsible for a degradation of stress ratio with continued shearing. This degradation behaviour could not be observed in the single-particle testing due to the absence of crushed particles. Therefore, the future work stemming from this thesis will be to link back single-particle testing to the macroscopic interface, by the introduction of crushed particles in single-particle testing.

One other limitation of the single-particle testing relied on in this thesis relates to the cyclical nature of the testing. As detailed in Section 6.5.2, because of the bi-directional nature of shearing, the 3D attack angle generated is an average of the two directions. This is a limitation of the experimental apparatus, and is not a limitation of the analysis method. One way to overcome this limitation would be to conduct the testing in a single direction, similar to the principal of ring shear. A single attack angle could be considered by shearing in a constant direction, where strain can be limitless, and the 3D attack angle can be isolated further. This would be a significant development in the understanding of the micromechanics of the particle-surface interface, and would allow for a more considered analysis of the role of angularity in the wear mode of the particle-surface interface.

Lastly, using the fundamental insights gleaned from this thesis, experimentation directly linked to real world applications can be conducted, with specific design cases in mind. This will enable the development of models to predict the long-term behaviour of real soil-structure interfaces, which will enable the design of interfaces to be refined, and the lifespan of interfaces to be extended with a greater focus on performance based design.

Appendix A

Effect of Crushed Particles on Soil-Structure Interface Behaviour

Appended here is a conference paper that was presented at the European Conference on Physical Modelling in Geotechnics. The paper investigates how fines generated within the interface layer can influence the interface behaviour, by conducting experimental testing on a Leighton Buzzard Sand — stainless steel interface. For this study macroscopic direct interface shear experiments were carried out in an inverted condition, where the effect of gravity would draw fine material away from the interface. It was not included in the main body of this thesis as it was not directly related to the micromechanics of the particle-surface interface, and the experimental work was carried out prior to PhD study. However, the findings of this study are of interest to the geotechnical community and have been referenced in the main thesis, and so are included here for completeness.

Abstract

When shear is induced at a soil-structure interface fines will be generated either by particle crushing or the breakage of asperities. In a standard monotonic interface test these fines will have a negligible impact upon the interface behaviour. However, during cyclic loading the volume of fines generated can become significant and hence the long-term effect on the interface behaviour needs to be investigated. Traditionally interface tests are designed such that the soil sits above the interface (an ‘upright’ test) and hence gravity and segregation would lead to the fines migrating towards the interface thus amplifying their impact on the observed

behaviour. However not all prototype interfaces are orientated in this upright direction; for example a pipeline will have an ‘upright’ interface at the crown of the pipe, an ‘inverted’ orientated interface at the invert of the pipe (where fines will migrate away from the interface) and an interface orientated at ninety degrees at the spring-line (side) of the pipe (where fines will migrate along the interface). As such, it is important to consider every potential prototype case when developing, for example, constitutive models. The development of such models to predict interface behaviour is becoming more commonplace, though consideration of the issues from the perspective of real engineering problems will enhance the utility of any models developed. A bespoke cyclic interface shearing device has been adapted to facilitate testing of interfaces in a variety of orientations. This equipment is also capable of providing visual observation of the movement and crushing of the soil particles during shearing using transparent model containers and high-resolution imaging. A series of interface tests conducted using this apparatus will be presented in this paper and the impact of fines, and fines migration, on the interface behaviour will be discussed.

A.1 Introduction

The physical changes in soil-structure interfaces, occur in the interface layer. This is a distinct band of soil that is in contact with the structural interface and far-field soil. The layer has been defined by various studies as five to ten times the mean particle diameter (DeJong and Westgate, 2009; Dejong et al., 2006). The confinement condition of a soil-structure interface has been widely studied. Three distinct conditions are found to affect the response of the interface: Constant Normal Load (CNL), $K = 0$; Constant Normal Stiffness (CNS), $K = \text{constant}$; Constant Volume (CV), $K = \infty$ (DeJong and Westgate, 2009; Evgin and Fakharian, 1996). The condition that occurs at the interface can vary for different applications. For example, a piled foundation, will experience an approximately constant stiffness boundary condition in the radial direction. One major shortcoming in the published literature regarding interface behaviour, is that cyclic behaviour of the interface has only been considered up to 45 cycles by Dejong et al. (2006). Other studies have considered cyclical behaviour, albeit at lower cycle number. In ‘live’ engineering problems such as the thermal cycling of pipelines or pile driving, interfaces may be sheared hundreds or thousands of times. The mechanism underlying this shearing is yet to be fully understood at cumulative displacements

in the order of tens of millimetres, let alone thousands. It has been shown by experimentation on soil-soil interfaces, that cyclical shearing gives rise to crushing of granular matter. For this study, Leighton Buzzard Sand (LBS) Fraction B is used as the testing medium due to the wealth of published research into its particle characteristics. Cavarretta et al. (2010, 2016); Senetakis et al. (2013), detail the particle crushing characteristics of LBS Fraction B in particle-particle contact. Such research provides a good reference point for developing the more complex model of soil deformation at the interface. Another shortcoming of interface research thus far, is that there has only been consideration of the upright condition of the interface, that is, where fine material migrates towards the interface layer due to gravity. An alternate case to model would be the inverted interface, where fine material developed falls away from the interface. This case is of importance when considering the boundary conditions of the interface, a buried pipeline for example, will have both an upright and inverted interface at the top and bottom of its circumference. A third case also exists, where an interface is orientated at ninety degrees at the spring-line of the pipe, where fines propagate parallel to the interface. A diagram of the three principal orientations is shown in Figure 2.12. For the purposes of this study, only the upright and inverted cases will be considered.

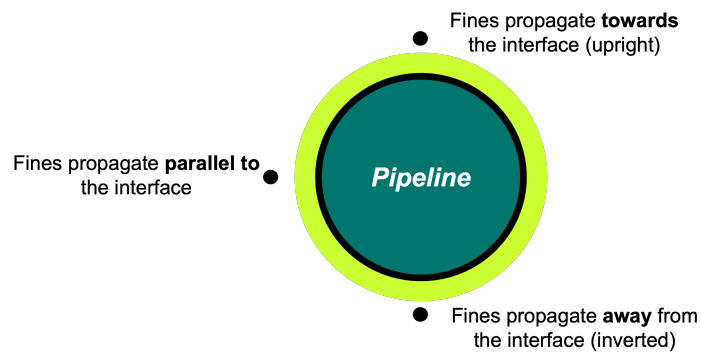


Figure A.1: Diagram of the three principal interface orientation conditions

A.2 Methodology

A.2.1 Experimental Apparatus

To identify the impacts of large cumulative displacements on interfaces, testing is carried out using a bespoke interface shear testing device, developed within the

Nottingham Centre for Geomechanics (Hashemi and Heron, 2017). Since the first

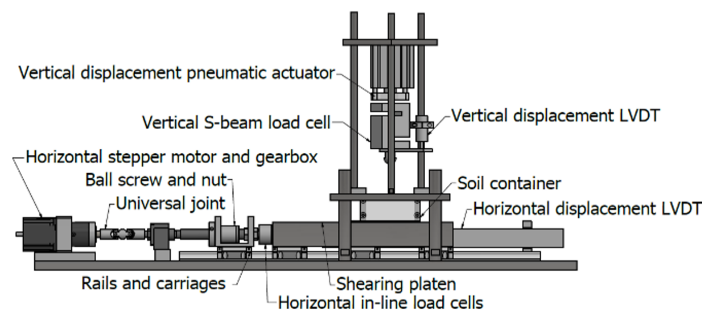


Figure A.2: Schematic of updated Toton Shear apparatus

uses of this apparatus, several improvements have been made. Firstly, imaging of the soil sample during testing is now possible, using a transparent sample container. Imaging of the soil sample allows for mechanical changes, identified in the interface layer, to be matched to recorded changes in sample stress and volumetric behaviour. Such an approach gives more context to trends identified in results data. Secondly, the entire assembly can be rotated through 180° for the testing of the inverted condition. Thirdly, the vertical load motor has been replaced by a pneumatic actuator and pressure controller. The controller has a much faster response time than the previously used motor and encoder control loop. Proportional-Integral-Derivative control is used to set a target pressure in the actuator, to apply a constant normal load on the sample. This improvement allows for a greater stiffness in the far-field soil, giving a closer approximation of the CNL condition than previously published. A schematic of the Toton Shear apparatus, in its upright configuration, with the described improvements is displayed in Figure A.2.

A.2.2 Test Plan

A basic test plan was used to simulate the interface condition at large cumulative shear displacements. The test plan is shown in Table A.1. Each test consists of 4000 shear reversals of 10 mm displacements, peak to peak (2000 full cycles). Although numerous previously published studies have used the cycle number to denote the length of a test, this can disguise the true amount of shearing a sample has experienced. For example, a shallow pipeline experiencing thermal cycling will not undergo repeated cycling at a constant displacement for its entire lifespan. It would be more accurate to consider the cumulative displacement and number

Table A.1: Test plan for upright and inverted direct shear tests

Test Code	σ_n kPa	$ u_x $ mm	θ
100-10-000-1	100	10	0
100-10-000-2	100	10	0
100-10-180-1	100	10	180
100-10-180-2	100	10	180

of shearing reversals. The normal stress, σ_n , and shear displacement magnitude, $|u_x|$, are constants throughout testing, to isolate the effect of a change in interface orientation angle, θ . The shear rate, v , is also constant throughout testing at 1 mm s^{-1} . Each test is repeated, for validation of results, and the identification of trends. Note that subsequent use of ‘upright’ and ‘inverted’ will refer to an interface orientation angle of 0° and 180° respectively, relative to the horizontal.

A.3 Testing Medium

A.3.1 Soil

Prior to testing, the Fraction B LBS was washed and dried, with a particle size distribution analysis carried out in accordance with BS 1377-1:2016 (British Standards Institution 2016). It is found that 90% of material passes between 2 mm and 1.18 mm. Samples are poured from the same height, through a sieve of size 3 mm, to limit the rate of each pour and ensure samples have equivalent relative density prior to testing. Each test sample is of mass 300 g, with a cross-sectional area of 80 mm×80 mm. At the end of testing, the sample is collected by spatula. The same particle size distribution analysis is then carried out, to assess the change in sample constitution. Hutchings and Shipway (2017), show that silica sand, such as the LBS used in this study, has a Vickers hardness value of 700 HV to 1200 HV. This is of key importance when considering the tribological implications of the shearing of the interface.

A.3.2 Structural Interface Plate

A 3 mm stainless steel plate is used to simulate the structural interface for the tests presented in this study. Vickers hardness tests have been conducted upon the

A.3. TESTING MEDIUM

material used, and an average hardness value of 188 HV has been found across three separate plates. Each plate of dimension 300 mm×108 mm has two tests conducted upon it, in virgin areas.

A.3.3 Data Collection and Processing

The Toton Shear apparatus utilises two parallel 1 kN capacity load cells, to transfer rotational force from the ball screw and nut, applied by a stepper motor, to linear force upon the shear platen. The shear platen is mounted upon rails that incur a rolling resistance. Prior to testing the samples, this rolling resistance is quantified by a series of 20 calibration shear displacements of 12 mm. A 0.001 inch feeler gauge is passed below the soil container before calibration, to ensure that the soil container does not impart any resistance upon the shear platen and has a consistent offset from the platen, outside of the cross section of the sample. When processing the raw data, acquired by a National Instruments Data Acquisition (DAQ) unit, the horizontal loads for forward - load cells in compression - and backward - load cells in tension - movement are treated separately, with calibration loads calculated for each. Across all four tests, the average forward and backwards rolling resistances were found to be 42.74 N, and -42.58 N respectively. The corresponding resistance is subtracted, as appropriate, from all load data in subsequent calculations and plots.

A.3.4 Image Data

Image data is captured by a Teledyne DALSA Genie Nano camera unit and 16 mm lens, mounted adjacent to the sample container. Due to the long focal length, an exposure time of 0.08 s is used to capture each frame. Images of resolution 4112 px×3008 px pixels are recorded every 2.5 mm of travel during shearing, giving an equivalent frequency of 0.4 Hz. Whilst during initial loading of the sample, images are recorded with a 1 Hz frequency. A high refresh rate is used as it is hoped in future studies to utilise the recorded image data in the use of advanced Particle Image Velocimetry. Each frame of image data can be matched to controller data by the indexing of each frame in the recorded data. As such, the micromechanisms that take place at the interface, can be identified with added context of the volumetric and stress response of the sample. One drawback of this analysis is that the image data only represents a 2D plane of the sample. An assumption must be made that the mechanism witnessed in this plane, must

also exist throughout the depth of the sample. During post-processing, the raw Portable Network Graphics (.png) files are cropped to the size of the sample in the frame, and the frame number is added to the image. An example of the recorded image data is shown in Figure A.3. The individual frames are stitched together as a video file, that can be used to examine the evolution of the micromechanisms present at the interface.

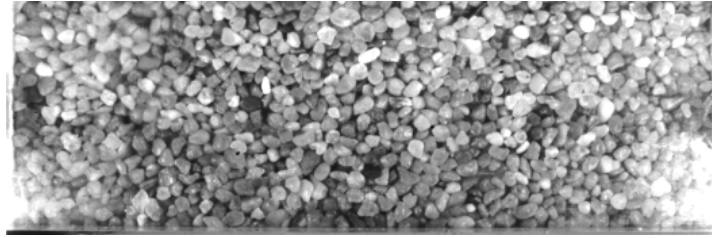


Figure A.3: Sample image after post-processing

A.3.5 Data Smoothing

The data gathered by the DAQ unit has an acquisition loop length of 0.1 s. As such, load data, particularly the horizontal data, is required to be smoothed by an appropriate method to remove the noise in the recorded data. Firstly, the average load, across the two parallel load cells, for each shear displacement (half cycle) is calculated. Hence, for the tests conducted in this study, 4000 average loads are presented. The same method has been carried out for the vertical load data, to allow the calculation of stress ratio, μ , for each cycle:

$$\mu = \frac{F_s}{F_n} \quad (\text{A.1})$$

where F_s is the average shear force and F_n is the average normal force across a given displacement. The unprocessed data is retained to allow for closer analysis of response in each displacement. Secondly, a local regression smoothing method (loess) (MATLAB 2019) is used to remove noise in the data. Smoothing is carried out upon load data in addition to vertical displacement data, recorded by the vertical Linear Variable Differential Transformer (LVDT), as to increase the clarity of general trends across test data.

A.4 Results and Discussion

A.4.1 Stress Response

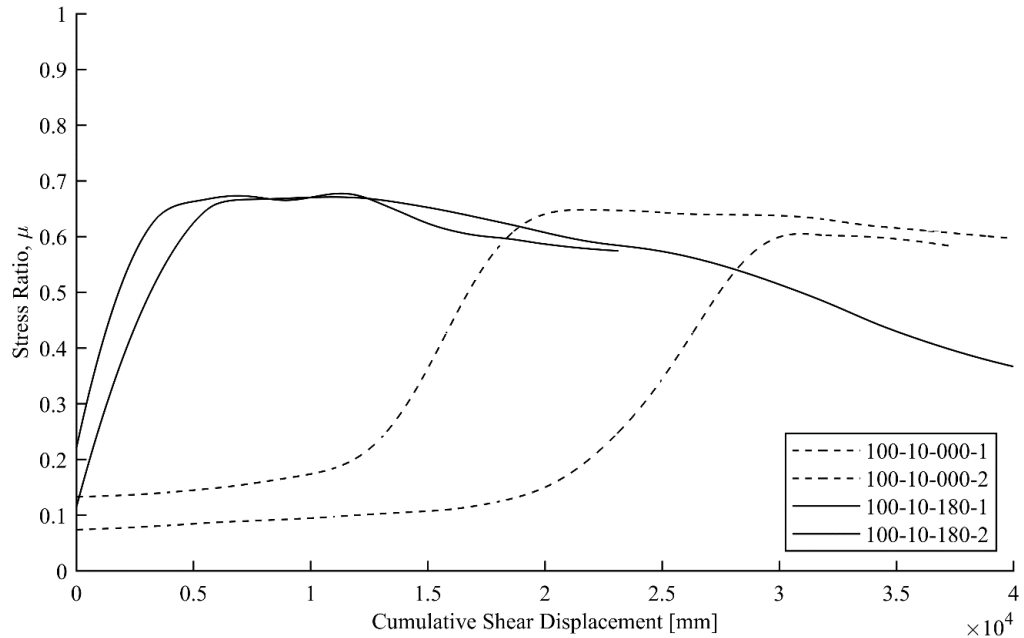


Figure A.4: Plot of the stress ratio, μ , vs cumulative shear displacement

Figure A.4 displays a plot of the evolution of the stress ratio throughout each of the four tests, up to a maximum cumulative shear displacement of 40 000 mm. It should be noted that due to a safety limit within the controller software, tests 100-10-000-2 and 100-10-180-2 did not complete the full 4000 shear displacements. The safety limit exists as to prevent damage to the apparatus. Tests that fail in this manner are unable to be restarted as the sample will have travelled outside of the tested area of the interface plate. Hence, unexpected rotations of particles at the interface may occur. Furthermore, when the test is stopped for a prolonged period, shear stress degradation occurs as the linear driving force on the shear platen is released by the stepper motor. As such, data for these tests has been cut at their relevant end points of 37 410 mm and 23 150 mm of displacement respectively. Fortunately, the data from these tests shows good similarity to the repeated tests. An immediate observation that can be made is that at large displacements, there is a steep increase in the stress ratio of each specimen, which has previously been unrecorded in published work. For the test pressure of 100 kPa and cyclic displacement of 10 mm, an upper limit exists at a stress ratio of 0.7. This value seems independent of the orientation of the interface, with inverted tests reaching

no higher value than upright tests. However, the inverted tests seem to show a more pronounced peak in stress ratio before steadily falling. It is evident that there is a similar trend in the rate of change in stress ratio during the rapid increase. The similarity in the rate of change in stress can be better shown by plotting the derivative of stress ratio against itself- shown in Figure A.5. It is shown that the earlier the onset of an increase in stress ratio, the greater the peak rate of increase. Interestingly, once the peak stress ratio has been reached, regardless of the stress path taken, the residual stress ratio is very similar for a test of the same type. This could suggest the existence of a critical state style condition. Note also, the inverted tests display a clear negative gradient after the peak stress ratio has been reached.

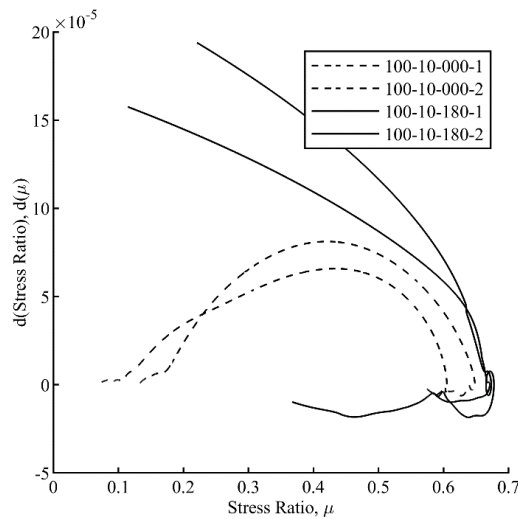


Figure A.5: Plot of first derivative of stress ratio, $d(\mu)$, vs stress ratio, μ

A.4.2 Volumetric Response

The eventual increase in stress ratio may be explained by the volumetric response of the sample over large shear displacements. The samples all contract over the duration of the test in a similar way to that presented in DeJong et al. (2003). On each reversal of shear displacement, the sample experiences a small dilation before steadily contracting for the rest of the displacement, as the soil skeleton rearranges to its lowest energy state. The volumetric data recorded by the vertical LVDT is shown in Figure 6. Similar to the stress response, there seems to exist a steady state where the rate of contraction of the sample remains constant after a point. During testing, the samples all experienced a plastic contraction due to

crushing of the grains in the interface layer, confirmed by an audible crushing sound.

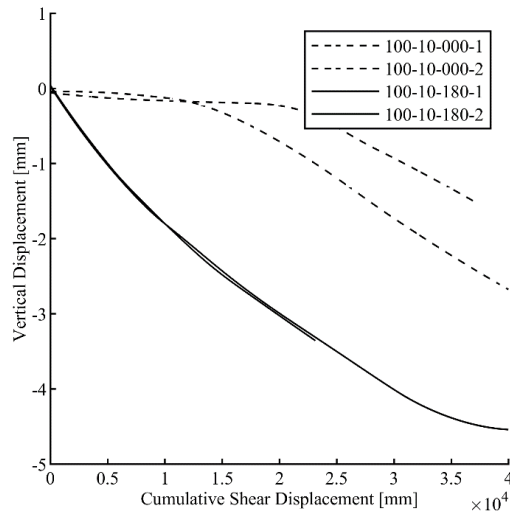


Figure A.6: Plot of vertical displacement against cumulative shear displacement

The crushing experienced can be witnessed in the image data. For example, in test 100-10-000-1 where the gradient becomes almost constant, at a cumulative shear displacement of 15 000 mm and 1500 reversals, the stress ratio begins to increase rapidly at the same point, and crushing is also seen to begin to occur. The crushing of the sample can also be confirmed by grain size distribution analysis. Figure A.7 shows a plot of grain size analysis on each of the four tested samples and a baseline of the clean, untested Fraction B. With consideration of the vertical displacement data in Figure A.6, samples with a greater total contraction, have a greater proportion of fine particles at the end of the test. Test 100-10-180-1 experienced the greatest total contraction. The gradient of its vertical displacement seems to fall close to zero as a cumulative displacement of 40 000 mm is reached. Figure A.8 shows a frame of image data taken at the end of the 100-10-180-1 test, with a cumulative displacement of 40 000 mm. When compared with the sample image in Figure A.3, it can be seen that the interface layer, shown at the bottom of the images, is saturated with fine material. It could be hypothesised that when the interface layer is fully saturated with fine material, an ultimate contraction is reached, where a sliding mechanism occurs again, and unbroken particles in the far-field soil do not contact the interface. The stress state at this point may reflect a standard direct shear test, comprised of the fine material. Further investigation into the stress state in the interface layer when saturated with fines, will need to take place.

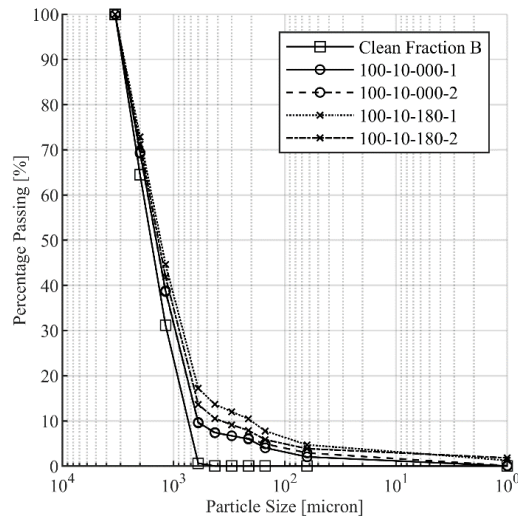


Figure A.7: Grain size distribution analysis for each test and a clean, untested sample

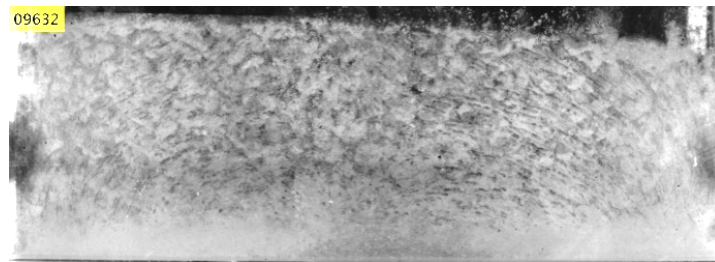


Figure A.8: Frame taken from test 100-10-180-1 at 40,000 mm displacement

It was observed during the upright tests that a period of sliding occurred, prior to the crushing. It is believed that any sample will experience crushing after an amount of interface shearing. Although the increase in stress ratio and plastic contraction occurred at smaller cumulative displacements for the inverted tests, it should not be assumed that all inverted tests will act in a similar manner. Future testing will seek to clarify if this immediate response is a function of orientation angle.

A.4.3 Damage to the Interface

After each test is conducted, surface fine material is cleaned from the plates. An image showing the plates of the one upright and one inverted test area is shown in Figure A.9. The tested area is clearly identified, with micro abrasions and ploughing wear on the interface plate. Plastic flow occurs via third-body abrasion when a normal load is applied to an abrasive particle with hardness $1.2\times$ greater

than the first (damaged) body (Hutchings and Shipway, 2017). As demonstrated in Section A.3.1, the hardness of silica sand far exceeds the value given for the structural interface plate. When the silica particles are forced into the relatively soft steel interface repeatedly, ploughing of troughs and abrasion occurs. Further study should be given to the relative hardness of the interface, and what effect that has on shear behaviour. One could hypothesise that the increase in stress ratio occurs due to fine particles falling into the abrasions on the interface plate. As the fine material, some of which has a diameter $<63\ \mu\text{m}$, is worked into the abrasions, the fine soil skeleton transfers more normal stress into shear stress. The damage upon the interface plate is worse in the middle of the sample area, note the darker band of wear in the middle of the sample area, caused by deeper grooves that reflect less light. This observation is key in validating that the experimental response is not caused by boundary effects. As the sample cycles through a stroke of 10 mm, the leftmost and rightmost 10 mm of interface plate boundaries of the interface plate are only worn for half of the amount of travel, as soil particles travel over this area. Hence, it would be expected for the boundaries to experience a smaller amount of wear than central areas.

A.5 Micromechanical Response

Using the image data, the micromechanisms that occur during interface shearing at high cumulative displacements, can be identified. For the first time, a distinct micromechanism has been identified for interface shearing. After many shear reversals, a random translation of a single particle within the interface layer occurs, causing a cascading rearrangement of particles in the remainder of the interface layer, and in the far field soil. This mechanism has not been previously described, and is likened to popcorn cooking, as the translation of one particle causes the translation of many more. This popcorning can be easily identified within the image data when viewed as a video, though is more difficult to identify in discrete frames, and therefore is omitted from this paper. The effect of inversion upon the fine material generated at the interface, can more easily be shown by comparison of the upright and inverted tests after crushing has begun. Figure 10 displays a comparison of the samples from the 100-000-10-4000 and 100-180-10-4000 tests, after the crushing mechanisms have begun, and near to the end of the tests. The fine material in the upright test, Figure A.10a, has formed a clear band of packed fine material, with a peak quantity of fines in the centre of the sample. This is

A. EFFECT OF CRUSHED PARTICLES ON SOIL-STRUCTURE INTERFACE BEHAVIOUR

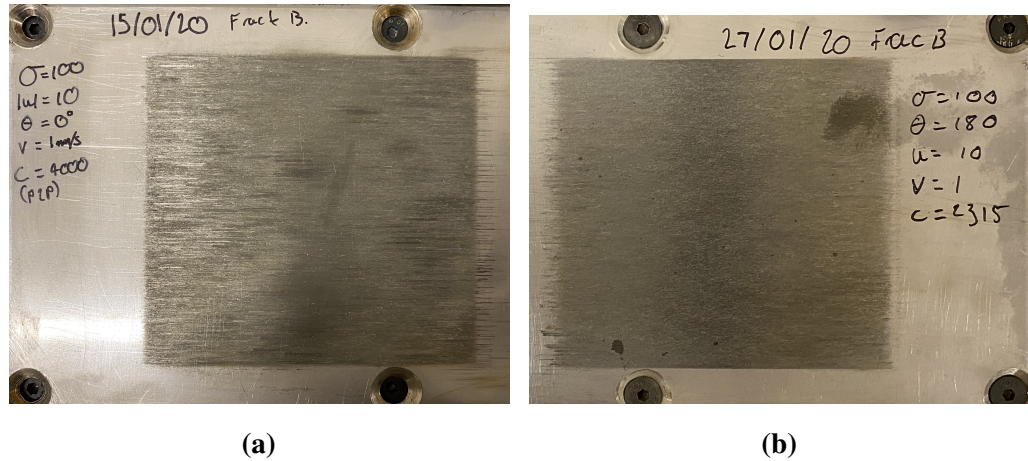
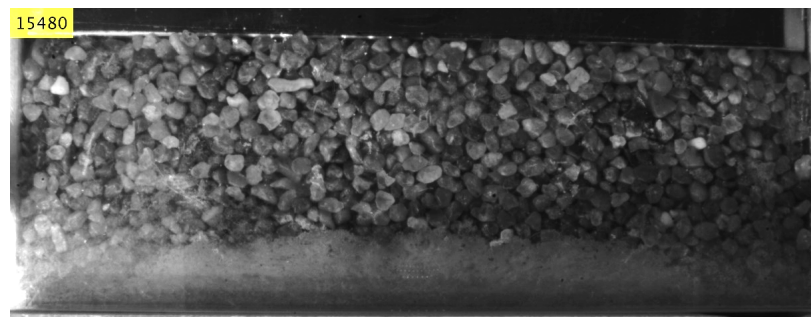


Figure A.9: Image of damaged interface plate after tests (a) 100-10-000-1, (b) 100-180-10-2

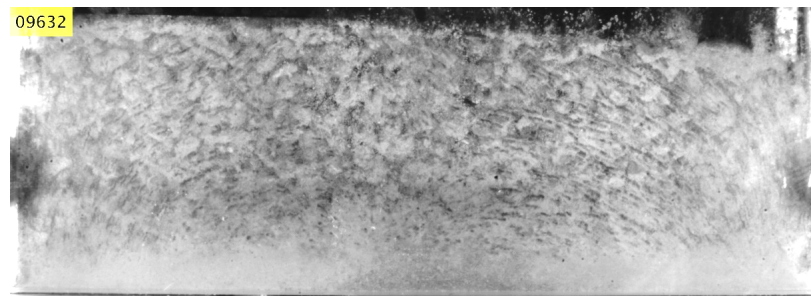
to be expected as fines tend towards the interface under the effect of gravity. In contrast, in the inverted sample Figure A.10b, fines have fallen throughout the sample, coating particles in the far-field soil. However, a concentration does exist in the interface layer. The absence of fine material in the far-field soil of the upright sample, and the concentration of fines in the interface layer of the inverted test, suggests that crushing only occurs in the interface layer. If crushing was to occur in the far-field soil, fines would be seen to coat the particles throughout the upright sample, with a greater concentration in the interface layer; this does not occur. Further work will be conducted to determine the origins of the fine/crushed material.

A.6 Conclusions

The experimental work presented in this study represents the first insight into interface shear behaviour at large cumulative displacements in the order of thousands of millimetres of travel and shear reversals. The existence of non-linear shear behaviour at large displacements is described and analysed with respect to the volumetric and stress responses of the test samples. Future work conducted will seek to specifically identify the cause of the steep rise in stress ratio, as well as the crushing of grains in the interface layer.



(a)



(b)

Figure A.10: Comparison of crushing mechanisms for (a) upright and (b) inverted test

Appendix B

3D Attack Angle Full Results

In this appendix, the full results of the 3D attack angle analysis are presented. Three plots, corresponding to the three different plots in Chapter 6, that show how particle vertical displacement, contact area, and 3D attack angle vary with stress ratio at the interface are presented. Where required, the x -axis range has been modified to suit the tests with very small amounts of cumulative energy (tests 521, 040).

B.1 3D Attack Angle

The general trend stated in the main discussion can be identified in Figure B.1. An elevation in stress ratio is caused by an increase in attack angle of the particle. However, some tests do not clearly support this trend (test 040, 225), which is likely as a result of grain mineralogy as well as errors in virtualising and processing the grain meshes. Although the mineralogy is similar between different Leighton Buzzard Sand grains, being a granular material, different grains will have slightly different mineral content and imperfections. As a consequence, not all particles will have identical strength characteristics. Therefore, the abrasive wear suffered by the grains will be variable which has an effect on the estimated contact point of the grain, the depth into the grain at which is actually in contact with the surface, as opposed to its assumed depth from vertical displacement tracking.

With regards errors arising from the virtualisation and mesh processing method — when smoothing ‘stair-steps’ blocking using ‘collapse_short_edges’. This process may smooth a key area of angularity which in fact triggers the increase in stress ratio.

B.1. 3D ATTACK ANGLE

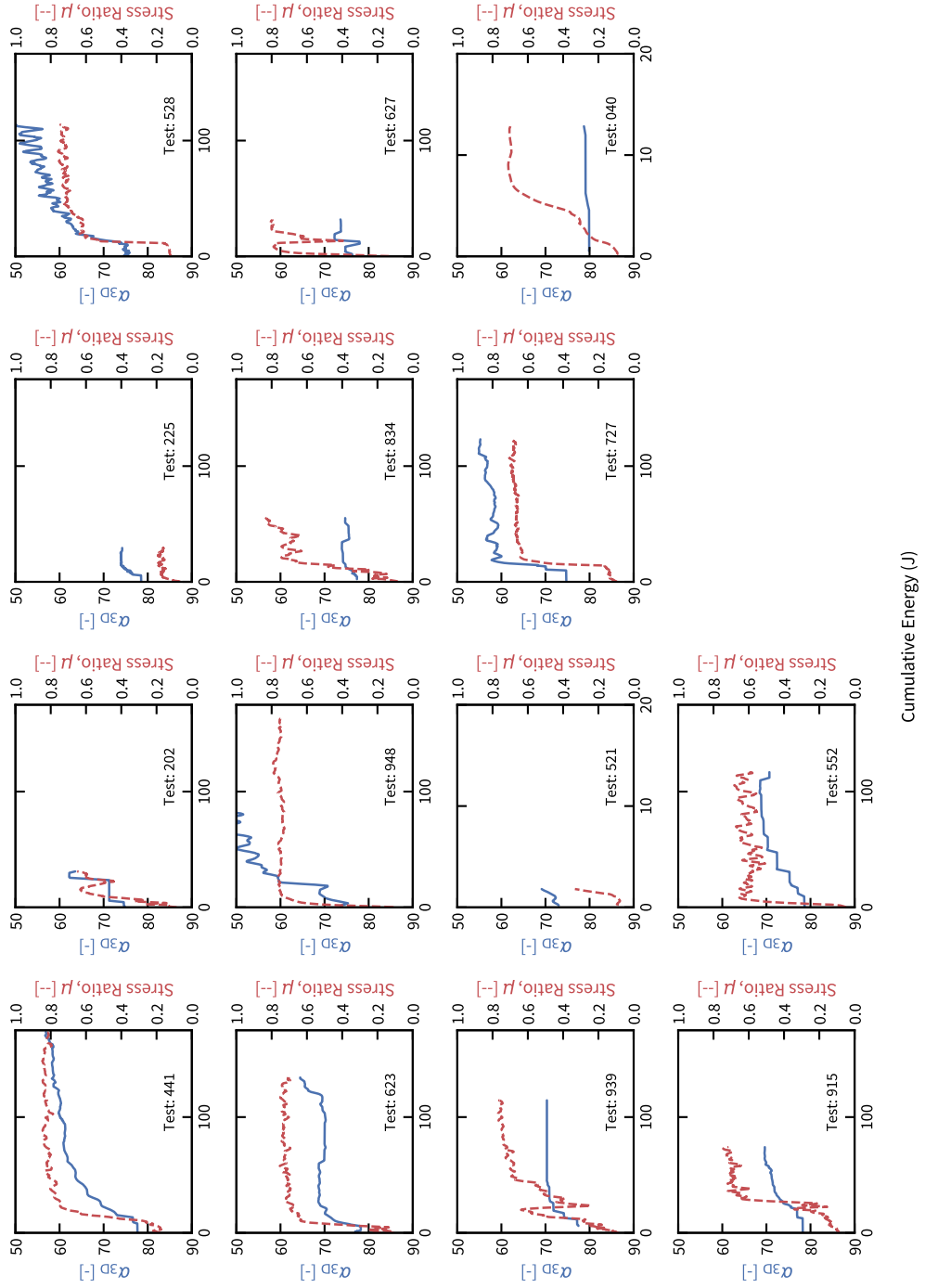


Figure B.1: Plots of 3D attack angle, α_{3D} , and stress ratio, μ , against cumulative shearing energy for the entire dataset

B.2 Particle Vertical Displacement

The supporting plots of particle vertical displacement against cumulative shearing energy, alongside stress ratio, are presented in Figure B.2.

B.3 Particle Contact Area

The supporting plots of particle contact area against cumulative shearing energy, alongside stress ratio, are presented in Figure B.3.

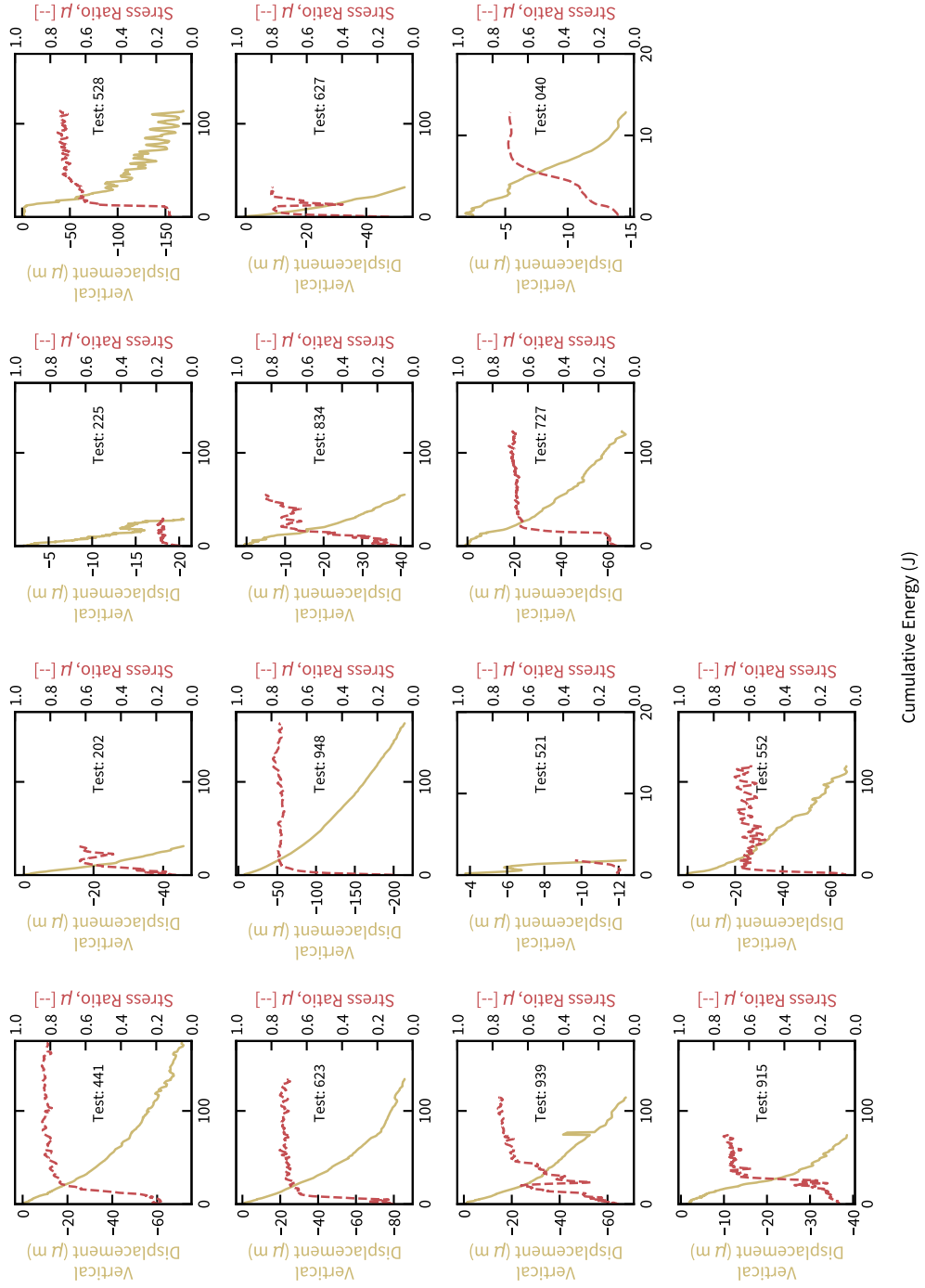


Figure B.2: Plots of particle vertical displacement, z , and stress ratio, μ , against cumulative shearing energy for the entire dataset

B. 3D ATTACK ANGLE FULL RESULTS

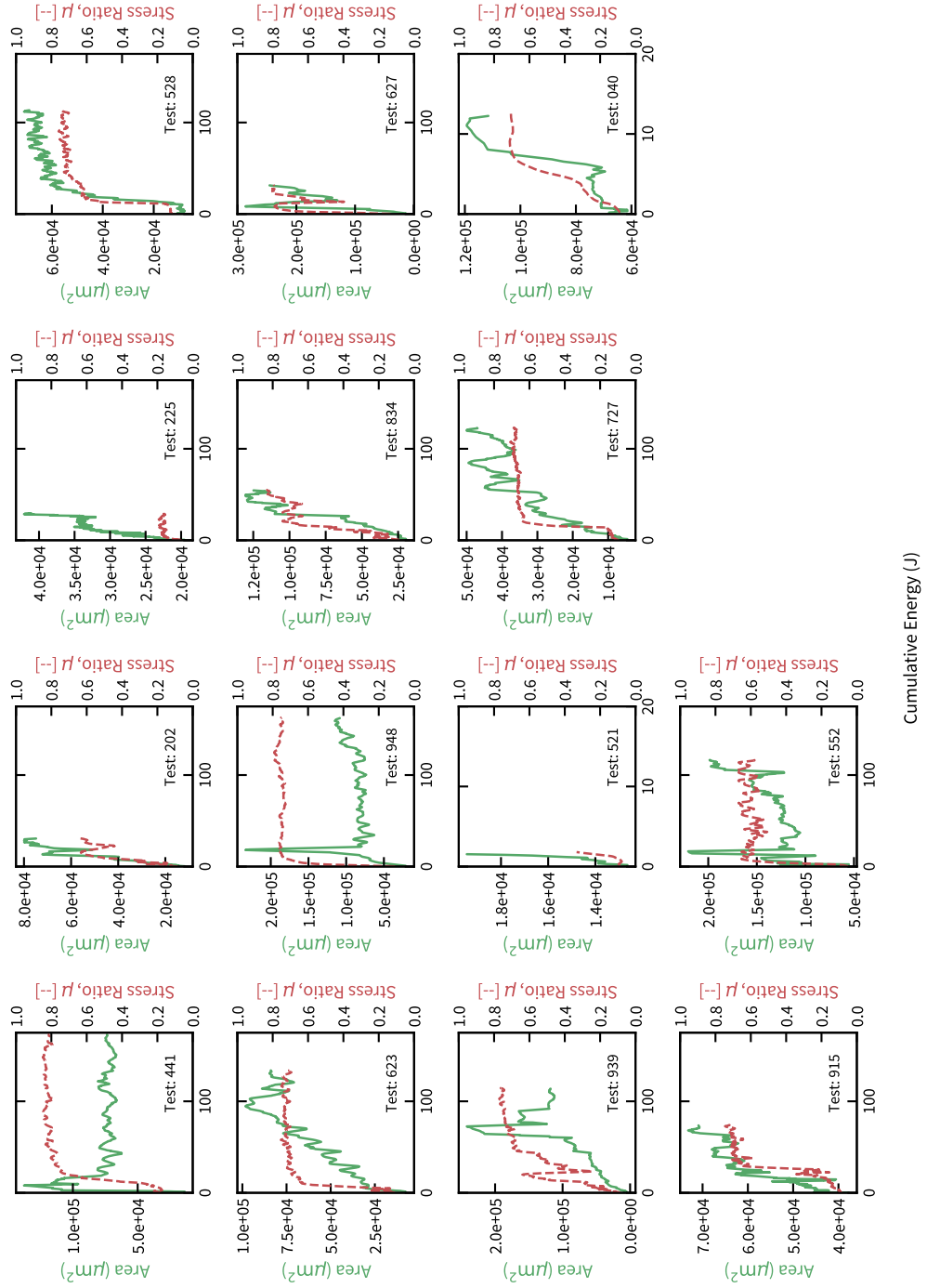


Figure B.3: Plots of particle contact area, A , and stress ratio, μ , against cumulative shearing energy for the entire dataset

References

- Angelidakis, V., Nadimi, S. and Utili, S. (2021), ‘SHape Analyser for Particle Engineering (SHAPE): Seamless characterisation and simplification of particle morphology from imaging data’, *Computer Physics Communications* **265**, 107983.
- Antonyuk, S., Tomas, J., Heinrich, S. and Mörl, L. (2005), ‘Breakage behaviour of spherical granulates by compression’, *Chemical Engineering Science* **60**(14), 4031–4044.
- Bagi, K. and Orosz, A. (2020), A New Variable For Characterising Irregular Element Geometries In Experiments And DEM Simulations, in ‘ECMS 2020 Proceedings Edited by Mike Steglich, Christian Mueller, Gaby Neumann, Mathias Walther’, ECMS, pp. 256–260.
- Bandini, V. and Coop, M. R. (2011), ‘The Influence of Particle Breakage on the Location of the Critical State Line of Sands’, *Soils and Foundations* **51**(4), 591–600.
- Barreto, D. and O’Sullivan, C. (2012), ‘The influence of inter-particle friction and the intermediate stress ratio on soil response under generalised stress conditions’, *Granular Matter* **14**(4), 505–521.
- Barrett, P. J. (1980), ‘The shape of rock particles, a critical review’, *Sedimentology* **27**(3), 291–303.
- Bažant, Z. P., Le, J.-L. and Bazant, M. Z. (2009), ‘Scaling of strength and lifetime probability distributions of quasibrittle structures based on atomistic fracture mechanics’, *Proceedings of the National Academy of Sciences* **106**(28), 11484–11489.
- Bernard, X. D., Eichhubl, P. and Aydin, A. (2002), ‘Dilation bands: A new

REFERENCES

- form of localized failure in granular media', *Geophysical Research Letters* **29**(24), 29–1–29–4.
- Bolton, M. (1984), *A Guide to Soil Mechanics*, Macmillan, Hong Kong.
- Cavarretta, I., Coop, M. and O'Sullivan, C. (2010), 'The influence of particle characteristics on the behaviour of coarse grained soils', *Géotechnique* **60**(6), 413–423.
- Cavarretta, I., O'Sullivan, C. and Coop, M. (2016), 'The relevance of roundness to the crushing strength of granular materials', *Géotechnique* **67**(4), 301–312.
- Cheng, Y. P., Nakata, Y. and Bolton, M. D. (2003), 'Discrete element simulation of crushable soil', *Géotechnique* **53**(7), 633–641.
- Cho, G.-C., Dodds, J. and Santamarina, J. C. (2006), 'Particle Shape Effects on Packing Density, Stiffness, and Strength: Natural and Crushed Sands', *Journal of Geotechnical and Geoenvironmental Engineering* **132**(5), 591–602.
- Cignoni, P., Callieri, M., Corsini, M., Dellepiane, M., Ganovelli, F., Ranzuglia, G. et al. (2008), Meshlab: An open-source mesh processing tool., in 'Eurographics Italian Chapter Conference', Vol. 2008, Salerno, Italy, pp. 129–136.
- Coop, M., Sorensen, K. K., Bodas Freitas, T. and Georgoutsos, G. (2004), 'Particle breakage during shearing of a carbonate sand', *Géotechnique* **54**(3), 157–163.
- Cundall, P. A. and Strack, O. D. L. (1979), 'A discrete numerical model for granular assemblies', *Géotechnique* **29**(1), 47–65.
- DeJong, J. T., Randolph, M. F. and White, D. J. (2003), 'Interface load transfer degradation during cyclic loading: A microscale investigation', *SOILS AND FOUNDATIONS* **43**(4), 81–93.
- DeJong, J. T. and Westgate, Z. J. (2009), 'Role of Initial State, Material Properties, and Confinement Condition on Local and Global Soil-Structure Interface Behavior', *Journal of Geotechnical and Geoenvironmental Engineering* **135**(11), 1646–1660.
- Dejong, J., White, D. and Randolph, M. (2006), 'Microscale observation and modeling of soil-structure interface behavior using particle image velocimetry', *Soils and Foundations* **46**, 15–28.

REFERENCES

- Evgin, E. and Fakharian, K. (1996), 'Effect of stress paths on the behavior of sand–steel interfaces', *Canadian Geotechnical Journal* **33**, 191–199.
- Fairhurst, C. (1964), 'On the validity of the 'Brazilian' test for brittle materials', *International Journal of Rock Mechanics and Mining Sciences & Geomechanics Abstracts* **1**(4), 535–546.
- Fakharian, K. (1996), Three-Dimensional Monotonic and Cyclic Behaviour of Sand-Steel Interfaces: Testing and Modelling., Thesis, University of Ottawa (Canada).
- Fakharian, K. and Evgin, E. (1997), 'Cyclic Simple-Shear Behavior of Sand-Steel Interfaces under Constant Normal Stiffness Condition', *Journal of Geotechnical and Geoenvironmental Engineering* **123**(12), 1096–1105.
- Fioravante, V. (2002), 'On the Shaft Friction Modelling of Non-Displacement Piles in Sand', *Soils and Foundations* **42**(2), 23–33.
- Fonseca, J., Nadimi, S., Reyes-Aldasoro, C. C., O'Sullivan, C. and Coop, M. R. (2016), 'Image-based investigation into the primary fabric of stress-transmitting particles in sand', *Soils and Foundations* **56**(5), 818–834.
- Fonseca, J., O'Sullivan, C., Coop, M. R. and Lee, P. D. (2012), 'Non-invasive characterization of particle morphology of natural sands', *Soils and Foundations* **52**(4), 712–722.
- Foray, P., Balachowski, L. and Rault, G. (1998), Scale effect in shaft friction due to the localisation of deformations, in 'Centrifuge 98', pp. 211–216.
- Frost, J. D., DeJong, J. T. and Recalde, M. (2002), 'Shear failure behavior of granular–continuum interfaces', *Engineering Fracture Mechanics* **69**(17), 2029–2048.
- Gates, J. (1998), 'Two-body and three-body abrasion: A critical discussion', *Wear* **214**(1), 139–146.
- Ghafghazi, M., Shuttle, D. and DeJong, J. (2014), 'Particle breakage and the critical state of sand', *Soils and Foundations* **54**(3), 451–461.
- Gudehus, G. and Nübel, K. (2004), 'Evolution of shear bands in sand', *Géotechnique* **54**(3), 187–201.

REFERENCES

- Guo, B., Song, S., Ghalambor, A. and Lin, T. R. (2014), *Offshore Pipelines: Design, Installation, and Maintenance*, second edition edn, Elsevier, GPP, Amsterdam.
- Hardin, B. (1985), 'Crushing of Soil Particles', *Journal of Geotechnical Engineering* **111**.
- Harmon, J. M., Arthur, D. and Andrade, J. E. (2020), 'Level set splitting in DEM for modeling breakage mechanics', *Computer Methods in Applied Mechanics and Engineering* **365**, 112961.
- Hashemi, M. A. and Heron, C. (2019), 'Analysis of particle contact using frustrated total internal reflection', *Meccanica* .
- Hashemi, M. A. and Heron, C. M. (2017), Development of a soil-interface device for cyclic and large deformation shearing, Proc. 19th ICSMGE.
- He, H., Senetakis, K. and Coop, M. (2019), 'An investigation of the effect of shearing velocity on the inter-particle behavior of granular and composite materials with a new micromechanical dynamic testing apparatus', *Tribology International* **134**, 252–263.
- HeliconSoft (2022), 'Helicon Focus'.
- Hertz, H. (1882), 'Ueber die Berührung fester elastischer Körper.', *Journal für die reine und angewandte Mathematik* **92**, 156–171.
- Ho, T., Jardine, R. and Nguyen, M. (2011), 'Large-displacement interface shear between steel and granular media', *Géotechnique* **61**, 221–234.
- Hou, WJ. (2008), Research on Monotonic and Cyclic Behavior and Constitutive Model of Three-Dimensional Soil–Structure Interface, PhD thesis, PhD thesis, Tsinghua University, Beijing.
- Hu, L. and Pu, J. (2004), 'Testing and Modeling of Soil-Structure Interface', *Journal of Geotechnical and Geoenvironmental Engineering* **130**(8), 851–860.
- Hu, L. and Pu, J. L. (2003), 'Application of damage model for soil–structure interface', *Computers and Geotechnics* **30**(2), 165–183.
- Huang, M., Chen, Y. and Gu, X. (2019), 'Discrete element modeling of soil-structure interface behavior under cyclic loading', *Computers and Geotechnics* **107**, 14–24.

REFERENCES

- Hutchings, I. M. and Shipway, P. (2017), *Tribology: Friction and Wear of Engineering Materials*.
- Kawamoto, R., Andò, E., Viggiani, G. and Andrade, J. E. (2018), ‘All you need is shape: Predicting shear banding in sand with LS-DEM’, *Journal of the Mechanics and Physics of Solids* **111**, 375–392.
- Kawamoto, R., Andrade, J. and Matsushima, T. (2018), ‘A 3-D mechanics-based particle shape index for granular materials’, *Mechanics Research Communications* **92**.
- Khrushchov, M. M. (1957), Resistance of metals to wear by abrasion, as related to hardness, in ‘Conference on Lubrication and Wear’, Institution of Mechanical Engineers, pp. 655–659.
- LeBlanc, C., Houlsby, G. and Byrne, B. (2010), ‘Response of stiff piles in sand to long-term cyclic lateral loading’, *Geotechnique* **60**(2), 79–90.
- Lee, D.-M. (1992), Angles of Friction of Granular Fills., Thesis, University of Cambridge.
- Lewiner, T., Lopes, H., Vieira, A. W. and Tavares, G. (2003), ‘Efficient Implementation of Marching Cubes’ Cases with Topological Guarantees’, *Journal of Graphics Tools* **8**(2), 1–15.
- Lewis, J. (1994), ‘Fast Template Matching’, *Vis. Interface* **95**.
- Lim, K.-W., Kawamoto, R., Andò, E., Viggiani, G. and Andrade, J. E. (2016), ‘Multiscale characterization and modeling of granular materials through a computational mechanics avatar: A case study with experiment’, *Acta Geotechnica* **11**(2), 243–253.
- Lindroos, M., Valtonen, K., Kemppainen, A., Laukkanen, A., Holmberg, K. and Kuokkala, V.-T. (2015), ‘Wear behavior and work hardening of high strength steels in high stress abrasion’, *Wear* **322–323**, 32–40.
- Liu, H., Song, E. and Ling, H. I. (2006), ‘Constitutive modeling of soil-structure interface through the concept of critical state soil mechanics’, *Mechanics Research Communications* **33**(4), 515–531.

REFERENCES

- Liu, J., Zou, D. and Kong, X. (2014), 'A three-dimensional state-dependent model of soil–structure interface for monotonic and cyclic loadings', *Computers and Geotechnics* **61**, 166–177.
- McDowell, G. R. (2005), 'A physical justification for $\log e$ – $\log \sigma$ based on fractal crushing and particle kinematics', *Géotechnique* **55**(9), 697–698.
- McDowell, G. R. and Bolton, M. D. (1998), 'On the micromechanics of crushable aggregates', *Géotechnique* **48**(5), 667–679.
- McDowell, G. R., Bolton, M. D. and Robertson, D. (1996), 'The fractal crushing of granular materials', *Journal of the Mechanics and Physics of Solids* **44**(12), 2079–2101.
- McDowell, G. R. and Daniell, C. M. (2001), 'Fractal compression of soil', *Géotechnique* **51**(2), 173–176.
- McDowell, G. R. and de Bono, J. (2013), 'On the micro mechanics of one-dimensional normal compression', *Géotechnique* **63**(11), 895–908.
- Medina, D. A. and Jerves, A. X. (2018), 'A geometry-based algorithm for cloning real grains 2.0', *Granular Matter* **21**(1), 2.
- Michael, M., Vogel, F. and Peters, B. (2015), 'DEM–FEM coupling simulations of the interactions between a tire tread and granular terrain', *Computer Methods in Applied Mechanics and Engineering* **289**, 227–248.
- Misra, A. and Finnie, I. (1981a), 'Correlations between two-body and three-body abrasion and erosion of metals', *Wear* **68**(1), 33–39.
- Misra, A. and Finnie, I. (1981b), 'On the size effect in abrasive and erosive wear', *Wear* **65**(3), 359–373.
- Moore, G. (1965), 'Cramming More Components Onto Integrated Circuits', *Electronics* **38**(8).
- Moore, M. A. (1974), 'The relationship between the abrasive wear resistance, hardness and microstructure of ferritic materials', *Wear* **28**(1), 59–68.
- Moore, M. A. and Douthwaite, R. M. (1976), 'Plastic deformation below worn surfaces', *Metallurgical Transactions A* **7**(12), 1833–1839.

REFERENCES

- Mortara, G., Ferrara, D. and Fotia, G. (2010), 'Simple Model for the Cyclic Behavior of Smooth Sand-Steel Interfaces', *Journal of Geotechnical and Geoenvironmental Engineering* **136**(7), 1004–1009.
- Mortara, G., Mangiola, A. and Ghionna, V. N. (2007), 'Cyclic shear stress degradation and post-cyclic behaviour from sand–steel interface direct shear tests', *Canadian Geotechnical Journal* **44**(7), 739–752.
- Mueth, D. M., Jaeger, H. M. and Nagel, S. R. (1998), 'Force distribution in a granular medium', *Physical Review E* **57**(3), 3164–3169.
- Nadimi, S. and Fonseca, J. (2017), 'Single-Grain Virtualization for Contact Behavior Analysis on Sand', *Journal of Geotechnical and Geoenvironmental Engineering* **143**(9), 06017010.
- Nardelli, V. and Coop, M. (2019), 'The experimental contact behaviour of natural sands: Normal and tangential loading', *Géotechnique* **69**(8), 672–686.
- Nardelli, V., Coop, M., Andrade, J. and Paccagnella, F. (2017), 'An experimental investigation of the micromechanics of Eglin sand', *Powder Technology* **312**, 166–174.
- Orosz, Á., Angelidakis, V. and Bagi, K. (2021), 'Surface orientation tensor to predict preferred contact orientation and characterise the form of individual particles', *Powder Technology* **394**, 312–325.
- Otsu, N. (1979), 'A Threshold Selection Method from Gray-Level Histograms', *IEEE Transactions on Systems, Man, and Cybernetics* **9**(1), 62–66.
- Oumarou, T. A. and Evgin, E. (2005), 'Cyclic behaviour of a sand - steel plate interface', *Canadian Geotechnical Journal* **42**(6), 1695–1704.
- Petty, A. and Heron, C. (2020), Effect of Crushed Particles on Soil-Structure Interface Behaviour, in 'European Conference on Physical Modelling in Geotechnics'.
- Petty, A. and Heron, C. (2023a), 'Quantifying Interface Abrasion with Particle Virtualization', *Geotechnical Testing Journal* .
- Petty, A. and Heron, C. M. (2023b), 'The role of abrasion in cyclically sheared soil-structure interfaces', *Géotechnique* **Pre-print**, 15.

REFERENCES

- Rabinowicz, E., Dunn, L. A. and Russell, P. G. (1961), 'A study of abrasive wear under three-body conditions', *Wear* **4**(5), 345–355.
- Russell, A. R., Muir Wood, D. and Kikumoto, M. (2009), 'Crushing of particles in idealised granular assemblies', *Journal of the Mechanics and Physics of Solids* **57**(8), 1293–1313.
- Saberi, M., Annan, C.-D. and Konrad, J.-M. (2018), 'On the mechanics and modeling of interfaces between granular soils and structural materials', *Archives of Civil and Mechanical Engineering* **18**(4), 1562–1579.
- Saberi, M., Annan, C.-D. and Konrad, J.-M. (2019), 'Implementation of a soil-structure interface constitutive model for application in geo-structures', *Soil Dynamics and Earthquake Engineering* **116**, 714–731.
- Sandeep, C. S. and Senetakis, K. (2018), 'Grain-scale mechanics of quartz sand under normal and tangential loading', *Tribology International* **117**, 261–271.
- Scikit-Image: Image Processing in Python* (2022), Image Processing Toolbox for SciPy.
- Senetakis, K., Coop, M. and Todisco, M. C. (2013), 'The inter-particle coefficient of friction at the contacts of Leighton Buzzard sand quartz minerals', *Soils and Foundations* **53**(5), 746–755.
- Seyedi Hosseininia, E. (2012), 'Investigating the micromechanical evolutions within inherently anisotropic granular materials using discrete element method', *Granular Matter* **14**(4), 483–503.
- Stringer, M. E., Cerna-Alvarez, E. and Kutter, B. L. (2020), 'Effects of the ratio between body forces and inter-particle forces on maximum void ratio', *Soils and Foundations* **60**(1), 1–12.
- Suhr, B., Skipper, W. A., Lewis, R. and Six, K. (2020), 'Shape analysis of railway ballast stones: Curvature-based calculation of particle angularity', *Scientific Reports* **10**, 6045.
- Sullivan, C. and Kaszynski, A. (2019), 'PyVista: 3D plotting and mesh analysis through a streamlined interface for the Visualization Toolkit (VTK)', *Journal of Open Source Software* **4**(37), 1450.

REFERENCES

- Todisco, M., Wang, W., Coop, M. and Senetakis, K. (2017), 'Multiple contact compression tests on sand particles', *Soils and Foundations* **57**(1), 126–140.
- Uesugi, M., Kishida, H. and Tsubakihara, Y. (1988), 'Behavior of Sand Particles in Sand-Steel Friction', *Soils and Foundations* **28**(1), 107–118.
- Uesugi, M., Kishida, H. and Tsubakihara, Y. (1989), 'Friction Between Sand and Steel Under Repeated Loading', *Soils and Foundations* **29**(3), 127–137.
- Virtanen, P., Gommers, R., Oliphant, T. E., Haberland, M., Reddy, T., Cournapeau, D., Burovski, E., Peterson, P., Weckesser, W., Bright, J., van der Walt, S. J., Brett, M., Wilson, J., Millman, K. J., Mayorov, N., Nelson, A. R. J., Jones, E., Kern, R., Larson, E., Carey, C. J., Polat, İ., Feng, Y., Moore, E. W., VanderPlas, J., Laxalde, D., Perktold, J., Cimrman, R., Henriksen, I., Quintero, E. A., Harris, C. R., Archibald, A. M., Ribeiro, A. H., Pedregosa, F., van Mulbregt, P. and SciPy 1.0 Contributors (2020), 'SciPy 1.0: Fundamental algorithms for scientific computing in python', *Nature Methods* **17**, 261–272.
- Vlahinić, I., Andò, E., Viggiani, G. and Andrade, J. E. (2014), 'Towards a more accurate characterization of granular media: Extracting quantitative descriptors from tomographic images', *Granular Matter* **16**(1), 9–21.
- Weibull, W. (1951), 'Wide applicability', *Journal of applied mechanics* **103**(730), 293–297.
- White, D., Campbell, M., Boylan, N. and Bransby, M. (2012), A new framework for axial pipe-soil interaction, illustrated by shear box tests on carbonate soils, *in* 'Offshore Site Investigation and Geotechnics 2012: Integrated Technologies - Present and Future, OSIG 2012', pp. 379–387.
- White, D. J., Take, W. A. and Bolton, M. D. (2003), 'Soil deformation measurement using particle image velocimetry (PIV) and photogrammetry', *Géotechnique* **53**(7), 619–631.
- Wood, D. M. (1991), *Soil Behaviour and Critical State Soil Mechanics*, 1 edn, Cambridge University Press.
- Xu, R. and Liu, E. L. (2019), 'Analysis on Evolution of Force Chain and Contact Network of Non-Cohesive Soil', *Key Engineering Materials* **803**, 253–261.

REFERENCES

- Zhang, G. and Zhang, J.-M. (2009), 'Constitutive rules of cyclic behavior of interface between structure and gravelly soil', *Mechanics of Materials* **41**(1), 48–59.
- Zhang, N. and Evans, T. M. (2018), 'Three dimensional discrete element method simulations of interface shear', *Soils and Foundations* **58**(4), 941–956.
- Zhao, B. and Wang, J. (2016), '3D quantitative shape analysis on form, roundness, and compactness with μ CT', *Powder Technology* **291**, 262–275.